POLITECNICO
MILANO 1863

SCUOLA DI INGEGNERIA INDUSTRIALE
E DELL'INFORMAZIONE

Satellite manoeuvre detection and estimation with radar observations

Tesi di Laurea Magistrale in
Space Engineering - Ingegneria Spaziale

Author: **Lorenzo Porcelli**

Student ID: 945295
Advisor: Prof. Pierluigi Di Lizia
Co-advisor: Dr. Diego Escobar Antón
Academic Year: 2020-21

Abstract

The increasing number of Resident Space Objects (RSOs) and congestion of the orbital debris environment cause activities for cataloguing of space objects to become more challenging year after year. The main source of potential new object detection corresponds to manoeuvres of operational satellites, creating trajectories unexpected by cataloguing systems. Detecting manoeuvres is crucial for maintaining catalogues of RSOs, since otherwise duplicated objects would populate the entire catalogue. Manoeuvre detection with survey observations can be understood as an association problem between the orbit of a RSO, estimated before the manoeuvre, and a set of Uncorrelated Tracks (UCTs), received afterwards, not necessarily all of them belonging to the manoeuvring satellite. In this thesis, a novel approach is proposed for detection and estimation of manoeuvres based on tracking observations, suitable to be used with survey data thanks to its run-time efficiency. The detection is realised in the measurements space, while a first guess for the manoeuvre is obtained via parameter estimation, employing an optimal control approach with a cost function depending on the velocity increment. The time for detection is considerably reduced, since, as opposed to orbit-to-orbit association, a full new object detection and initiation is not required. However, a single track after a manoeuvre is not enough information to estimate the manoeuvre and post-manoeuvre orbit with enough accuracy to correlate future tracks. Thus, this track-to-orbit correlation needs to be combined with a track-to-track method in order to associate post-manoeuvre tracks corresponding to the manoeuvring RSO until obtaining similar accuracy for the post-manoeuvre orbit (and the manoeuvre itself) as in the no-manoeuvre scenario. The proposed methodology is able to provide reliable first manoeuvre estimates which are then refined with high-fidelity orbit determination. Results are presented for simulated radar data, highlighting the qualities of the detection and estimation strategy.

Keywords: *manoeuvre detection and estimation*, *cataloguing*, *uncorrelated tracks resolution.*

Abstract in lingua italiana

Il crescente numero di Resident Space Objects (RSOs) e la congestione dello spazio intorno alla Terra rendono le attività di catalogazione degli oggetti spaziali sempre più impegnative. La fonte principale di rilevamento di oggetti potenzialmente nuovi sono le manovre dei satelliti, che causano lo spostamento di quest'ultimi su traiettorie non previste dai cataloghi orbitali. Rilevare queste manovre è cruciale per il corretto mantenimento dei cataloghi di RSO e per evitare la generazione di duplicati. Il rilevamento e la stima di manovre tramite osservazioni di sorveglianza può essere inteso come un problema di associazione fra un'orbita, stimata prima della manovra, e un insieme di tracce non correlate, ricevute successivamente e non necessariamente appartenenti allo stesso oggetto. Questa tesi presenta un nuovo approccio per rilevamento e stima di manovre a partire da osservazioni di tracking, applicabile anche in scenari di sorveglianza grazie al suo basso costo computazionale. Il rilevamento è effettuato a partire dalle misurazioni ed è seguito da un algoritmo basato su un approccio ottimo che permette di ottenere una prima stima della manovra. Il tempo necessario per il rilevamento è sensibilmente ridotto perché, a differenza di metodologie che sfruttano associazioni orbita-orbita, l'inizializzazione di un nuovo oggetto non è richiesta. Ciononostante, i dati contenuti in una singola traccia post-manovra non sono sufficienti per stimare l'orbita post-manovra e la manovra stessa con sufficiente accuratezza. Per questo motivo, la correlazione traccia-orbita per la stima della manovra deve essere preceduta dall'applicazione di una metodologia per associazioni traccia-traccia, in modo da correlare sufficienti osservazioni post-manovra dello stesso RSO, fino ad ottenere un'accuratezza per la manovra e l'orbita post-manovra simile a casistiche senza alcun impulso. La metodologia proposta permette di ottenere una stima iniziale della manovra successivamente rifinita tramite orbit determination ad alta fedeltà. I risultati sono ottenuti a partire da dati radar simulati, mostrando le qualità dell'algoritmo sviluppato per il rilevamento e la stima.

Parole chiave: *rilevamento e stima di manovre*, *catalogazione*, *risoluzione di tracce non correlate*.

Contents

Abstract **i**

Abstract in lingua italiana **iii**

Contents **v**

1 Background and introduction to the problem **1**
1.1 The space environment and Resident Space Objects (RSOs) 1
1.2 The space debris problem 6
1.3 Space Surveillance and Tracking (SST) 9
1.4 Space Traffic Management (STM) 12
1.5 Cataloguing activities 13
1.6 The impact of manoeuvring objects on SST activities 17
1.7 Scope of the thesis 19
1.8 Structure of the thesis 21

2 State of the art **23**
2.1 Introduction 23
2.2 Detection and estimation with surveillance data 24
2.3 Detection and estimation with tracking data 27

3 Methodology for manoeuvre detection and estimation **35**
3.1 Manoeuvre detection 35
3.2 Manoeuvre estimation 38
3.2.1 Batch-least squares parameter estimation for first manoeuvre estimates 38
3.2.2 Selection of first manoeuvre estimate for subsequent re- estimation . 41
3.2.3 Development of dynamical model for manoeuvre estimation 42

4 Results **49**

4.1 Results of the accuracy tests for the dynamical models 49
4.2 Setup of simulation scenario 56
4.3 Results for manoeuvre detection 61
4.4 Results for manoeuvre estimation 62
4.4.1 General results 63
4.4.2 Test case: impulsive manoeuvre 69
4.4.3 Test case: long manoeuvre 74
4.4.4 Impact of track separation and time elapsed since manoeuvre on estimation 77

5 Conclusions and future work **81**

Bibliography **85**

A Appendix A **95**
A.1 Coordinate systems 95
A.2 Analytical model for measurements simulation and prediction 99

B Appendix B **103**

List of Figures **105**

List of Tables **107**

List of Symbols **109**

Acknowledgements **111**

Ringraziamenti **113**

1 | Background and introduction to the problem

1.1. The space environment and Resident Space Objects (RSOs)

Geospace, defined as the region of outer space near Earth including the upper atmosphere and magnetosphere [1], is a vast and dynamic environment influenced by the activity of the Sun and of other far-away bodies. The majority of man-made space objects, except the ones devoted to interplanetary or deep space missions, currently resides in the lower part of this region [2], extending from the Von Kármán line, which has an altitude of 100 km as defined by the FAI (Fédédération Aéronautique Internationale)[1], up to the outer Van Allen radiation belt (altitude comprised between $\approx$ 19,134 km and $\approx$ 44,646 km [4]).

According to the Database and Information System Characterising Objects in Space (DISCOS) [5], which is a catalogue maintained by the European Space Operation Centre (ESOC) of the European Space Agency (ESA), the number of tracked artificial Resident Space Objects (RSOs) orbiting the Earth has reached a record of 29,498 by mid October 2021. The growth of the number of RSOs has been non-stopping since the beginning of the space age in 1957 with the launch of Sputnik 1 [6]. The catalogue reports RSOs with dimensions down to 1 mm, but with the vast majority of them (99.6%) being larger than 10 cm due to the complications of observing small objects from ground. The data gathered in DISCOS is subsequently analysed, commented and presented to the public in an Annual Space Environment Report, whose last version was published in May 2021 [2]. As of mid October 2021, around 58% of the total number of objects (precisely 17,115) is bounded in Low Earth Orbits (LEOs), having an altitude comprised in the interval between 0 and 2,000 km. The popularity of this region can be attributed to its combination of altitude-orbital period, which makes it suitable for a large variety of space applications,

[1] There are currently different proposals for the standard altitude of the line; for example, other authors claim it should be placed at 80 km [3].

such as remote sensing [7] and satellite internet provision via constellations [8]. If one considers other typologies of orbits which cross the LEO region, such as Geostationary Transfer Orbits (GTOs) and LEO-MEO Crossing Orbits (LMOs), the number grows to 20,874, about 70% of the total. Another popular region for RSOs (891 objects, around 3% of the total) is the Geostationary Earth Orbit (GEO) belt, with altitudes between 35,586 km and 35,986 km. As the GEO revolution period is equal or very close to a sidereal day, the observed scene on the Earth for a spacecraft orbiting in this region is almost fixed. This property is exploited to provide services such as telecommunications, weather forecasting and TV broadcasting [7]. Figure 1.1 shows the distribution of RSOs objects according to their orbital regimes. Along with the already mentioned orbits, the bar plot shows the number of objects in Extended Geostationary Orbits (EGOs), Navigation Satellites Orbits (NSOs), MEO-GEO Crossing Orbits (MGOs) and Highly Eccentric Earth Orbit (HEOs) [2].

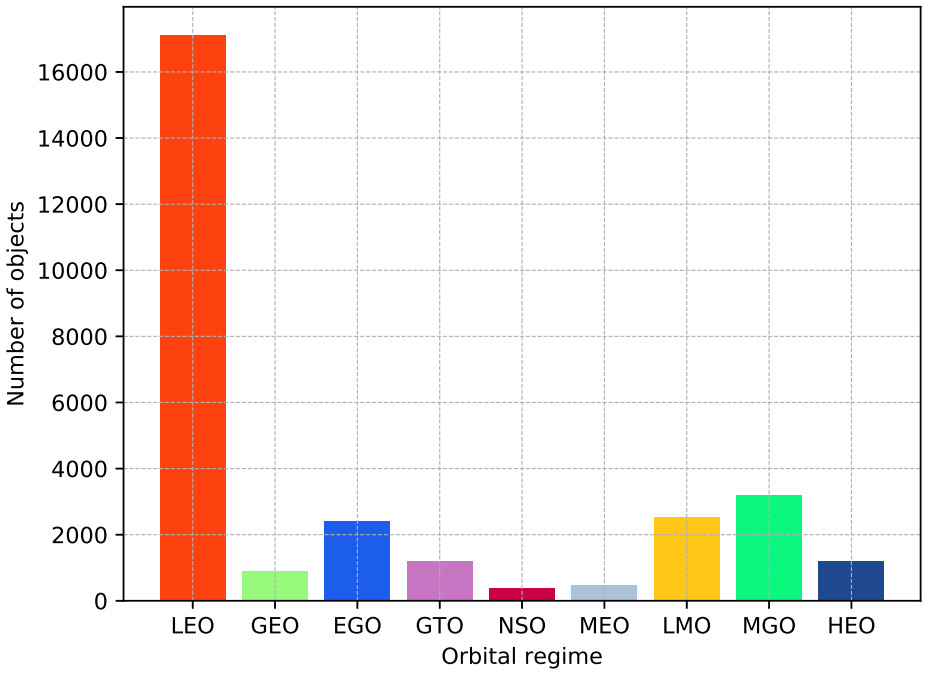

Figure 1.1: Distribution of RSOs according to their orbital regime in DISCOS (up to mid October 2021).

These numbers include both functional and non-functional artificial objects (commonly referred to as **space debris** [9]). A functional object might also be defined as **operational** or **cooperative**, while space debris are **un-cooperative** objects since their motion cannot be artificially controlled.

The main sources of the generation of new RSOs can be grouped into three categories:

1. **launch events**.
2. **intentional release** of mission-related objects.
3. on-orbit **fragmentation events**.

In contrast to this, an object may not be considered an Earth-orbiting RSO anymore if it escapes Earth's sphere of influence (in interplanetary or deep space missions) or if it decays in the atmosphere due to natural perturbations or induced de-orbiting. Atmospheric re-entry is typical for objects residing in LEO [6].

Of the total number of objects, around 81% of the total in DISCOS (23,953) has been identified and correlated to a source, while the genesis of the remainder is unclear. Launch events are commonly responsible for the release of two types of RSOs. The main target of a launch is in general an operational spacecraft, but if non-reusable vehicles are employed, then their stages can become non-cooperative RSOs if their decay was not planned. The number of launch events per year has not been following a rectilinear trend in the 60 years of space age, due to a great influence of different external factors. As an example, a modulation over a period of 11 years is generally noticeable [6], as it represents the duration of a solar cycle (implying constraints at mission level). Also geopolitical events had an impact, such as the collapse of the Soviet Union, that led to a steep reduction of launch events at the beginning of the '90s [7]. Figure 1.2 reports the number of launches as reported by the DISCOS catalogue up mid October 2021. It is noticeable that the trend has been increasing in the last ten years (after the 90's decline) and is reaching the peaks of the golden age of the '70s.

Future market predictions foresee an increase in launch-events-related RSOs due to the general reduction of the cost of access to space [10], the increasing popularity of micro/nano satellites [11] and CubeSats [12] (often deployed in swarms), the build-up of new satellite constellations [13] and the growth of emerging space agencies. This trend has been already observed in the last two years (2020 - 2021): the United Nations Office for Outer Space Affairs (UNOOSA) reports a total of 1,273 launched payloads in 2020 and a peak of 1,389 in year 2021 (between January and October) [14]. As of mid October 2021, the DISCOS catalogue contains a total of 9,520 identified objects ($\approx$ 32% of the total) which can be associated to this category, considering payloads (both operational and non-operational systems, as well as calibration objects, for a total number of 7,554) and rocket bodies (1,966 objects).

The second main source of new RSOs is related to the intentional release of mission-related

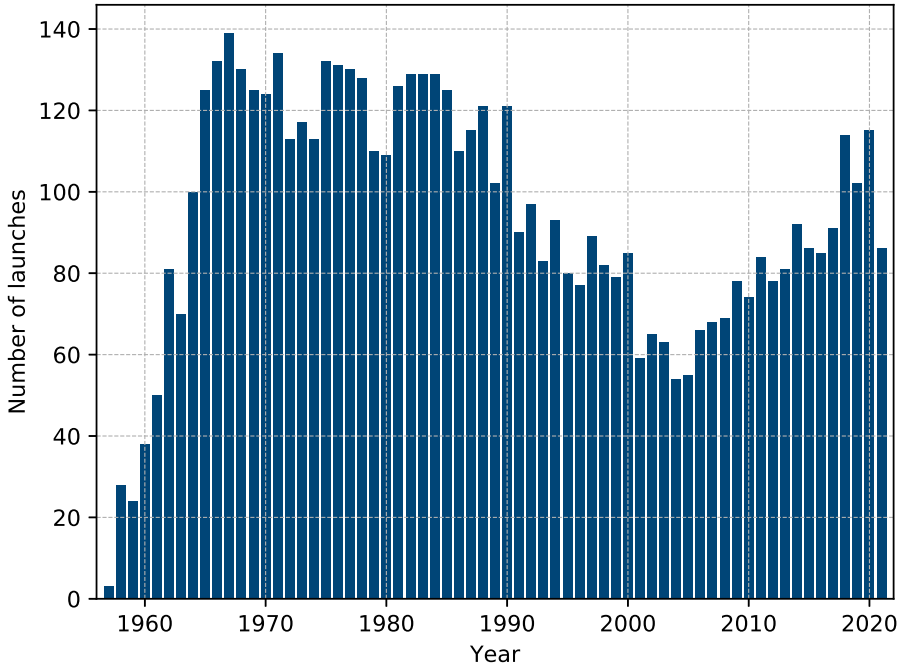

Figure 1.2: Number of launches per year according to DISCOS (up to mid October 2021).

objects. Such events can both occur during the launch phase and in the operational phase of a satellite. Considering launchers, a major contribution to this category is represented by Solid Rocket Motors (SRMs) firings, which generate slag (diameter in the order of mm) and dust particles (diameter in the order of μm), mainly composed of aluminium oxide (Al_2O_3) [6]. Other sources of mission-related objects for launchers are the jettisoning of fairings or adapters. Spacecrafts and payloads can instead release expendable devices such as lens covers or yo-yo de-spin devices; other objects could also be left in orbit during Extravehicular Activities (EVAs) [6]. By mid October 2021, the number of DISCOS objects afferent to this category is 1,305, approximately the 4.4% of the total.

The last main source of RSOs is represented by debris which come from on-orbit fragmentation events. In ESOC's Space Environment Annual Report [2], a fragmentation is loosely defined as *"an event on-orbit that creates space debris without purpose, including but not limited to collisions, explosive break-ups, and tear and wear"*. Adopting this definition, also objects coming from unintentional releases will be considered in this group. The category includes both objects whose original fragmentation event has been identified and documented and those of unclear genesis but correlated to a potential source (which is possible through analysis of their orbital and physical properties). Figure 1.3 reports the number of confirmed fragmentation events occurred each year up to mid October 2021.

The total number is 639, with 278 of them just in the last two decades. On average, 9.8 events have occurred every year.

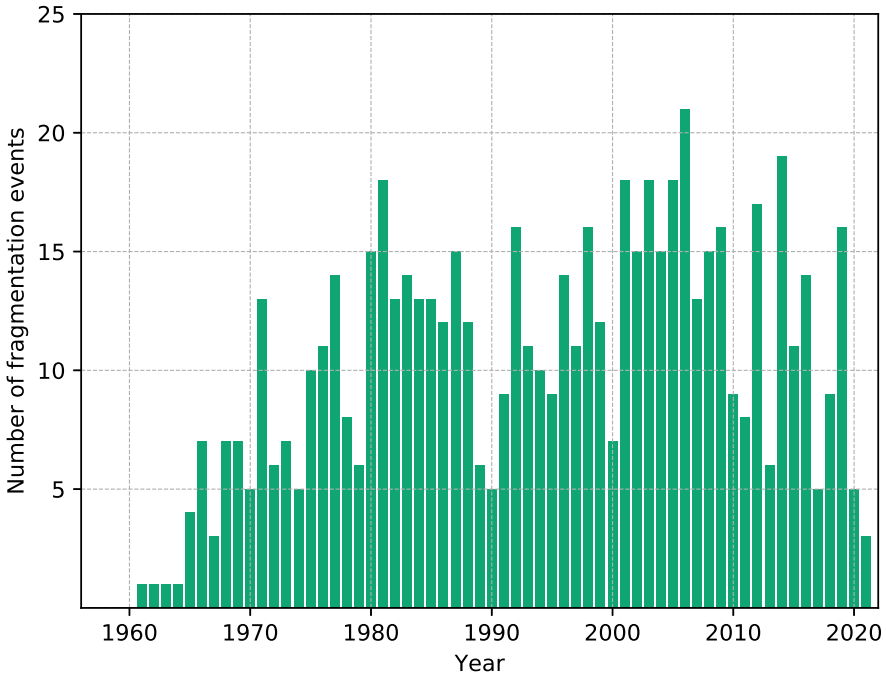

Figure 1.3: Number of fragmentation per year according to DISCOS (up to mid October 2021).

Fragmentation events might be subsequently categorised according to their origin and/or nature [2]: accidental (break-up due to design flaws), aerodynamics (overpressure due to drag), anomalous (unplanned separation of an object from a spacecraft), collision (also considering small impactors), deliberate (intentional fragmentation events), electrical (mostly related to battery explosions), propulsion (non completely passivated thrust systems leading to break-ups or explosions) and others. The greatest fragmentation events in history of space operations are represented by the ASAT (Anti-SATellite weapon) test conducted on the Fengyun 1C satellite in 2007, which created over 3,000 fragments, and by the collision between Cosmos 2551 and Iridium 33 in 2009 with over 2,500 objects generated [2]. An example of deliberate fragmentation is represented by the several ejections of the nuclear reactor coolant on board of Soviet RORSATs (Radar Ocean Reconnaissance Satellites) occurred in the '80s, which generated population of sodium–potassium alloy (NaK) droplets in LEO (between 900 and 950 km in altitude) [15]. These might be defined as *"historic, non-regenerative"* sources of space debris [6], as they were unique and singular events related to no-more-operational spacecrafts. Other examples are the

Westford copper needles, which were deployed in orbit in the '60s as part of a US radio communication experiment [16]. The total number of objects catalogued in DISCOS falling in this category by October 2021 is 13,128, around the 44% of the total.

Figure 1.4 shows a bar plot discriminating the nature or source of the artificial Earth-orbiting objects. It is evident that fragmentation events represent the most prominent source of new RSOs.

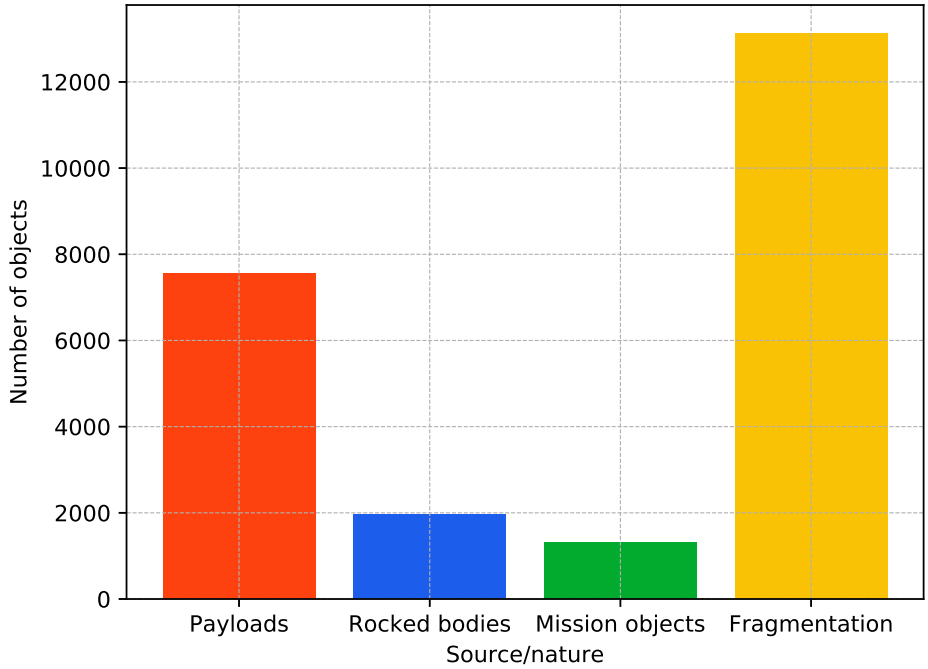

Figure 1.4: Distribution of RSOs according to their nature/source in DISCOS (up to mid October 2021).

1.2. The space debris problem

Apart from the classification of RSOs according to their origin, which gives a deeper insight on the main sources of objects in space, it is extremely important to distinguish and quantify the numbers of operational and non-operational objects or debris. According to DISCOS, the number of operational satellites in orbit is estimated to be around 5000 ($\approx$ 20% of the total) [5], which means that the tracked non-operational objects represents the 80% of the entries in the catalogue.

It is clear that space debris is the dominant type of resident space objects and it is essential to state that this population is actually way larger if one considers the objects

that cannot be observed and catalogued. As already mentioned, this is generally due to small size (in the order of centimetres and below), which make observation from Earth extremely difficult at the current technological level [6]. There are currently on-going studies to design systems capable of detecting the millimetre and sub-millimetre population of space debris, which generally propose in-situ measurements [17] [18] with dedicated instrumentation. The state-of-the-art methodology to infer information on such population is to use predictive mathematical models and employ them in numerical simulations, generally determining the debris or meteoroid flux on a given user-defined orbit. Examples of dedicated software are the ESA MASTER (Meteoroid and Space Debris Terrestrial Environment Reference) [19] or the NASA (National Aeronautics ans Space Administration) ORDEM (Orbital Debris Engineering Model) software [20]. Both MASTER and ORDEM are based on the statistical generation of a population (to a given epoch) mimicking all known debris creation mechanisms (such as SRM firings, multi-layer insulation degradation, release of paint flakes, predicted fragmentation events, with dimensions in the order of μm and greater), including historical sources (NaK droplets, Westford needles, past fragmentation events) and fusing information coming from external RSOs catalogues. To provide a representative number, as of November 1st 2016, the reference MASTER population consisted of 911,000 non-functional objects with dimensions greater than 1 cm [21]: it is glaring that debris is gradually clustering the environment.

The presence and the non-cooperativeness of space debris represent a serious threat to the safety of space operations since the risk of collision between objects increases. A collision event can be harmful as it can lead to fragmentation and possibly cause the failure of subsystems, systems or entire spacecrafts. Collisions can become a self-sustaining source of space debris: a first fragmentation event might generate fragments that subsequently lead to a second collision, then a third one, and so on, entailing a cascading failure. There is currently on-going research to determine optimal or sub-optimal strategies for Collision Avoidance Manoeuvres (CAMs) to be performed by operational spacecrafts in order to reduce the probability of collision [22] [23] [24].

The concerns of the community of scientists and experts over the increasing population of space debris and the consequent risks have grown in the last years. The earliest alarms were risen by Donald J. Kessler in the '70s who first theorised the later-called Kessler syndrome [25]. Such concerns later led to the creation of dedicated national working groups and of organisations promoting international cooperation. One example is the Inter-Agency Debris Coordination Committee (IADC), which is an inter-governmental forum created in the '90s from ESA, NASA and other national space agencies. One of their activities is to publish the IADC Space Debris Mitigation Guidelines [9], which

describe and suggest possible space debris **mitigation measures**, which are actions that shall be taken to reduce the adverse effects of debris and limit their self-generation. Such measures cover all the phases of a space mission, from the launch phase up to the disposal of the spacecraft, which shall be transferred into a graveyard orbit (especially if in GEO) or de-orbited until atmospheric re-entry [9]. The aforementioned collision avoidance manoeuvres are also a type of mitigation measure which can be actively taken to avoid fragmentation events. There are other entities currently concerned with the study of debris mitigation: one of them is the Orbital Debris Co-ordination Working Group (ODCWG), part of the International Organisation for Standardisation (ISO), which aims instead at defining applicable standards for debris mitigation practices.

Despite their importance, it is important to remark that mitigation measures are actually just a tool to limit the growth rate of non-cooperative RSOs but not to effectively reduce the population size. Studies have shown that the current space environment is not in a stable point, meaning that even in the case of a no-further release scenario (considering no human interaction with space) the population of RSOs would still slowly increase due to the domino effect created by on-orbit collisions. The predictions forecast that even in LEO, where objects can naturally re-enter thanks to atmospheric drag, the number of newly generated fragments would still overpass the number of decayed objects [26]. Investigating the factors that dominate this stability, it was proven that mitigation measures are currently not sufficient to reach a steady state and that more actions, called **remediation measures**, shall be taken to tackle the issue [27]. Three possible strategies that can be undertaken jointly with mitigation measures to achieve stability are:

1. to **limit the launch rate** to reduce the injection of payloads and rocket bodies.
2. to **reduce** the satellites' **maximum lifetime** (the IADC currently suggests maximum 25 years in LEO [9]) before disposal.
3. to deploy **Active Debris Removal (ADR)** systems

The last topic is of great interest at the moment and the on-going research is thriving. ADR systems are on-orbit tools used to capture any type of space object and eventually dislocate it, such that it could re-entry the atmosphere or could be transferred to a graveyard orbit. Current proposed solutions include pulling, pushing or contact-less technologies [28].

Taking into account all the considerations made so far about the risks of having a growing population of inoperative space objects, as well as the importance of mitigation/remediation measures, it is clear that the first crucial step is to gain **awareness**

of the whole RSOs environment. Both active satellites and debris shall detected, catalogued and their orbits continuously predicted. A better knowledge of the observable environment also entails greater realism in the simulators for the debris population in the sub-centimetre domain. All of these data (true and simulated) can be used afterwards to predict the evolution of the RSOs population and support further studies on mitigation measures and removal systems. This is typically accomplished via medium and long-term (up to 100 years) numerical analyses for different scenarios [6] with dedicated propagators. An example of the latter is the DELTA (Debris Environment Long-Term Analysis) software developed by ESA [29], which allows to simulate the evolution of the debris environment in the case of unchanged operational practices or varying parameters such as the launch rate per year, the explosion rate and the SRM firings rate.

1.3. Space Surveillance and Tracking (SST)

The **detection, cataloguing and orbit prediction activities** for RSOs fall under the so-called discipline of **Space Surveillance and Tracking (SST)**, considered as a branch of Space Domain Awareness (SDA) or Space Situational Awareness (SSA) (as by ESA's definition [30]). SSA also focuses on the monitoring and prediction of Space Weather (SWE) and on the detection of Near-Earth Objects (NEOs), which are natural bodies that can potentially impact the planet. SST operations generally rely on a network of sensors which observe the sky performing object tracking or surveillance activities. The collected data is then processed at dedicated ground stations, which also monitor the sensors and schedule their tasks. The types of sensors usually employed are optical (as telescopes or Satellites Laser Ranging Stations, or SLRs) or microwave (such as radars) [6]. The instrumentation is generally ground-based, but there is growing interest in space-based technologies, currently being tested in operational scenarios. All of the SST sensors can provide angular measurements of the position of the object (right ascension and declination, or azimuth and elevation); microwave instruments and SLRs can also provide range measurements, while range-rate measurements (via Doppler shifting) can only be obtained by radars. Generally, these measurements are passive, in the sense that no active link with the object is established. Ground-based radars are mainly used to detect objects in LEO and MEO, while for higher altitudes (as in GEO) the power associated to the electromagnetic radiation would not be sufficient to sense objects, hence optical sensors are employed [31]. Radars have the advantage of being operative under all lighting conditions, whereas optical sensors have limitations regarding the amount of environmental light and the relative brightness of the visible space object. Furthermore, optical sensors are in general not suitable for tracking in LEO (at the current technological level), as the high

velocity of the object and the smaller sensor field of view with respect to radars entail the necessity of rapidly adapting the pointing. On the other hand, the inherent advantage of optical sensors is the possibility of reaching higher spatial resolutions.

The biggest SST network currently operating is the Space Surveillance Network (SSN), which under the supervision of the United States Space Command (USSPACECOM). The network is made of radio frequency and optical sensors displaced all over the world and two Command and Control centres located in mainland United States. The network is currently being augmented with the US Space Based Space Surveillance SBSS System, a satellite at $\approx 630\,km$ altitude equipped with an optical camera. A map of all the centres that constitute the SSN is reported in Figure 1.5.

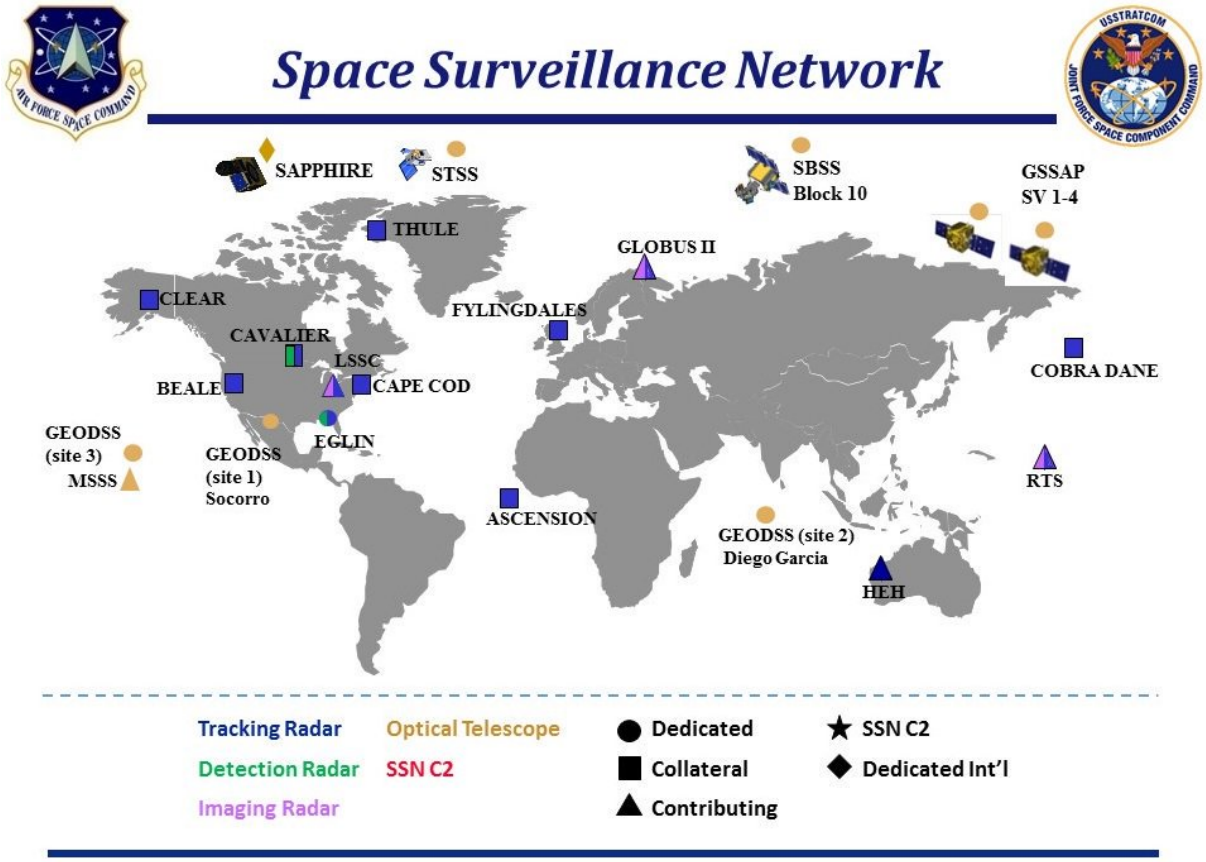

Figure 1.5: Location of the SSN sensors and facilities. Credits 18$^{\text{th}}$ SPCS [32].

In Europe, ESA started the already mentioned SSA program, which lead to the institution of new offices and centres dedicated to SST activities, relying on observation data coming from its own telescopes or from external partners. European national space agencies have built their own SST facilities both in mainland and in other continents. In the last fifteen years, the European commission established and funded a SST support framework, whose goal is to coordinate and develop the European SST capabilities to ultimately

provide high quality services. This program is called EUSST (European Union SST): the involved actors are 7 national space agencies or other public entities (France, Germany, Italy, Poland, Portugal, Romania, Spain, forming the SST Consortium) and the European Satellite Centre (SatCen), building up the so-called SST Cooperation. Figure 1.6 shows a map of all the SST sensors that are operated by the members of the EUSST programme.

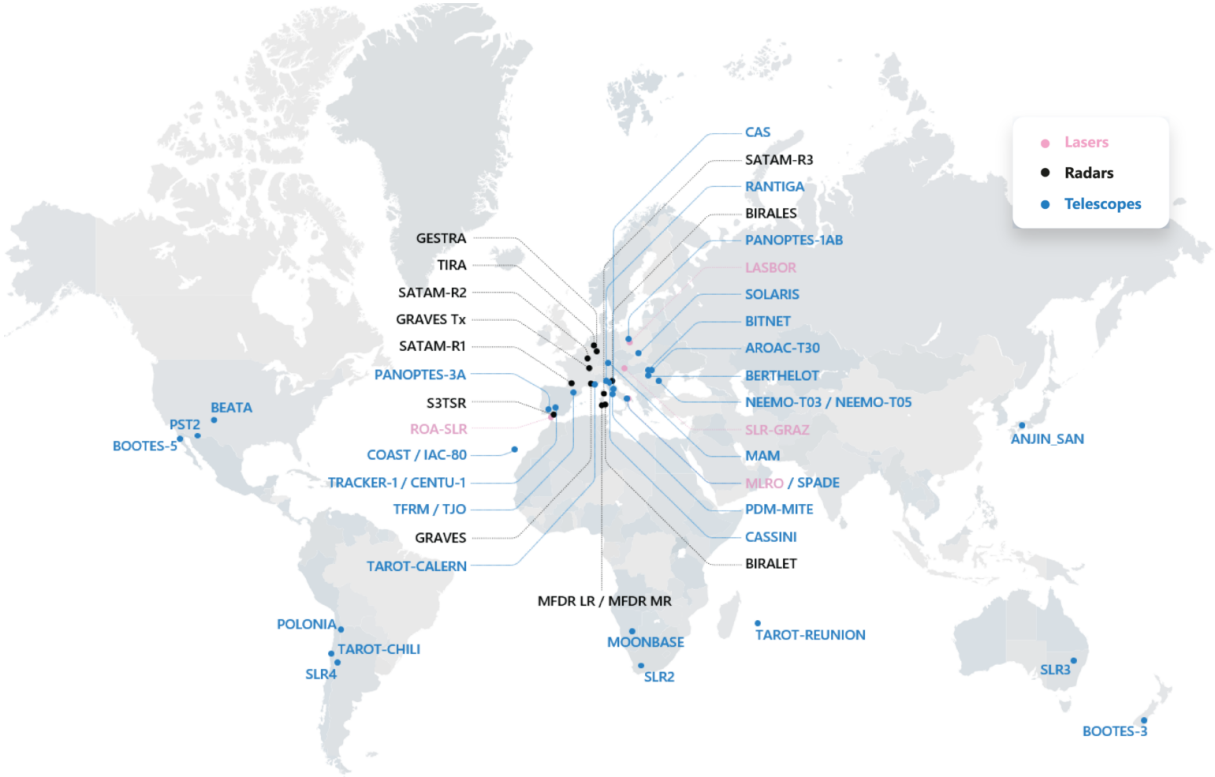

Figure 1.6: Map of the EUSST sensors network. Credits EUSST [33].

The outcome of a single sensor observing an object is generally referred to as **track**, which is a set of observations over a short time period assumed to belong to the same object [34]. An **observation** is instead a set of **measurements** taken at a specific time instant. A SST sensor can generally observe an object and produce a track every couple of orbital periods, according to the objects' orbit, location of the sensors and their fields of view. Tracks from surveillance instrumentation are defined as **Uncorrelated Tracks (UCTs)** and in the particular case of optical sensors they might be called **Uncorrelated Optical Observations (UCOs)** as well [35]. The term **uncorrelated** is employed as surveillance sensors generally do not have any information on the identity of the observed objects, in opposition to tracking sensors, which are designed to follow specific objects as they fly in space. Other terms that can be used for uncorrelated observations (generally optical ones, for the limited field of view of the sensors) are **Too Short Arcs (TSAs)** [31] or **Very Short Arcs (VSAs)** [36] when their duration is under 0.2% of the orbital period

of the object [37]. The following dissertation will follow these definitions, which might be found under different names in SST scientific literature.

SST activities, along with helping in gaining greater awareness of the space environment, can be further exploited to provide different services to satellite and launch operators. For instance, SST centres can forecast a possible impact between a satellite and debris by propagating very precise ephemerides, and emit a warning so that satellite operators can program a collision avoidance manoeuvre. Conjunction Data Messages (CDMs) are a recommended standard format defined by the Consultative Committee for Space Data Systems (CCSDS) [38], to exchange conjunction information between the originators of Conjunction Assessments (CAs) and the satellite owners/operators. A CDM contains information about a single conjunction between two objects: it provides position and velocity at the time of closest approach for both objects in a given reference frame, the covariance associated to the objects' states, the expected miss distance and the probability of collision. Other services provided by SST centres include mission assistance during launch, deployment and end-of-life phases, re-entry prediction and fragmentation analysis.

1.4. Space Traffic Management (STM)

All the procedures mentioned so far about collision avoidance can be placed within a greater framework, defined as Space Traffic Management (STM). The International Academy of Astronautics (IAA) provides the following definition of STM: *"Space traffic management means the set of technical and regulatory provisions for promoting safe access into outer space, operations in outer space and return from outer space to Earth free from physical or radio-frequency interference"*. The latter was first given in a Cosmic Study published by the IAA in 2006 [39], in which the requirements and prospects for managing future space traffic, as well as analysing the possible means to implement them, were described. STM is therefore mainly concerned with the study and application of policies, both at international and national level, which regard the planning, the coordination and the synchronisation of activities to improve the safety and sustainability of operations in space. Traffic management regulations are just a part of the wider **space law** discipline. The United Nations (UN) are involved at an intergovernmental level through the already mentioned Office for Outer Space Affairs. One of the main tasks of the latter is to assist and advise the UN Committee on the Peaceful Uses of Outer Space (COPUOS), which promotes international cooperation for peaceful uses and exploration of space (as example, it issued the 1979 Moon Treaty [40] and keeps track of the 1963 Partial Test Ban Treaty [41]). The COPUOS also redacted its own debris mitigation guidelines in 2010

[42], based on the IADC technical content but taking into consideration the aforementioned UN treaties and principles on the respect of outer space. In 2018, the committee developed the Guidelines for the Long-term Sustainability of Outer Space Activities [43], addressing all aspects that threat the sustainability of the space environment. Another goal of the OOSA is to encourage states or other international intergovernmental organisations (such as ESA or EUMETSAT, the European Organisation for the Exploitation of Meteorological Satellites) to register objects launched into space. The office has maintained its own register of space objects since 1962, originally with the goal of supporting the COPUOS in discussions about political and legal issues concerning outer space. As space law has evolved in the years, the register is now a means to assess the share of each state's international responsibility for space objects.

Other examples of international bodies concerned with STM are the already mentioned IADC, with its debris mitigation guidelines, or the ITU (International Telecommunication Union), which regulates the frequency band allocation of satellites in GEO [44], in order to prevent harmful electromagnetic interference. In Europe, the European Commission is currently investigating STM and funding two major projects: EUSTM (European Union STM) [45] and SPACEWAYS [46], both part of the Horizon 2020 research and innovation program. The first project is led by GMV and involves Avio, GOMspace and Onera among the others; the second one has stakeholders such as Airbus, Arianegroup and Elecnor Deimos. The goal of these projects is to assess the current and the required European technical capabilities in the domain of SSA and develop a STM baseline to support the interests of the European Union.

1.5. Cataloguing activities

A **catalogue** is one of the main outcomes of SST activities. It is an automated database containing updated information about every detected and tracked RSO. In every catalogue, each object has an unique ID and associated information about its orbit (determined through observations) and other physical (or not) properties. This last piece of information can include the object type, dimensions, mass, average cross section and launch or fragmentation year. The aforementioned DISCOS catalogue by ESOC includes comprehensive information on the estimated size, mass, cross sections, launch date, launch site and satellite operator (if a payload). The catalogue mainly relies on information from own and contracted research. DISCOS does not directly provide orbital data, but this can be retrieved from other sources: in fact, the majority of DISCOS objects is also labelled with a COSPAR ID (Committee on Space Research International Designator) or a NORAD ID

(North American Aerospace Defence Command catalogue number), which are identifiers used in other catalogues. The NORAD IDs were instituted for SpaceTrack's SATCAT catalogue (or simply SpaceTrack), publicly accessible on the internet (via [47] or [48]). This publication relies on data processed by the 18$^{\text{th}}$ Space Control Squadron (SPCS)[2] of the United States SPACECOM, which obtains raw data from all over the SSN. In SATCAT, information about each object is clustered in text files formatted according to the Two Line Elements (TLE) set standard. A TLE contains both the NORAD and the COSPAR ID, the reference epoch, the first and the second derivative of the mean motion, the starred ballistic coefficient B^* or the solar radiation pressure coefficient, a set of Keplerian elements (inclination, right ascension of the ascending node, eccentricity, argument of perigee, mean anomaly and mean motion) and the number of completed revolutions at the epoch of publication. TLE data comes from the fitting of observation measurements with semi-analytical solutions of the equations of motion following the Simplified Generalised Perturbations (SGP) model or Simplified Deep Space Perturbations (SDP), describing the perturbed dynamics of an object including gravity gradient, luni-solar attraction and atmospheric drag [49]. Five versions of these models (SGP, SGP4, SDP4, SGP8, SDP8) were developed, but currently only SGP4 is employed. The latter includes a mode for near-Earth objects (period $< 225\ min$) and a deep-space mode (period $> 225\ min$, according to NORAD's definition [49]). TLEs have the advantage of providing meaningful data in a compact form, but the major drawback is their low accuracy and the absence of meaningful data quantifying the uncertainty on the orbital elements [50]. SpaceTrack is periodically updated with the TLEs of 17000 on-orbit objects, with dimensions down to 10 cm, limited by the current capacities of the sensors in the SSN. The 18$^{\text{th}}$ SPCS also maintains another catalogue, known as High Accuracy Catalogue (HAC) [51] or Special Perturbations (SP), from the name of the high accuracy orbit propagator employed in orbit determination processes. The catalogue is not publicly available and accredited access must be requested. Another popular public catalogue is published and maintained by the JSC Vimpel Interstate Corporation and the Keldysh Institute of Applied Mathematics [52]. The catalogue relies on data coming from JSC Vimpel's own telescopes and from external partners. The information contained in this catalogue is typically merged and used in synergy with SpaceTrack as the latter lacks of information about objects in HEO and GEO, while the former strongly focuses on them. The JSC Vimpel catalogue is updated approximately every two weeks and by October 2021 contains information about ≈ 7000 objects. Other private institutions and companies manage their own catalogues, relying on in-house data or on external SST networks.

[2] In the recent past, it was maintained by the Joint Space Operations Centre (JSpOC) at the Vandenberg Air Force Base, California, USA.

In order to provide high quality services, a SST operator must be able to publish a catalogue as more complete as possible, taking into account the current technological observation limits. The catalogue must be accurate and precise, as small inaccuracies in the estimation of orbital properties can lead to failures in assessing collision risks or predicting re-entries. Furthermore, the catalogue shall be updated as more frequently as possible. The **cataloguing activities** can be grouped in two categories or phases:

- **catalogue build-up**: related to the detection and identification of new RSOs without prior information.
- **catalogue maintenance**: related to the update of the orbital information (or of any other kind of parameter) of already catalogued objects.

These two phases are not clearly separated nor sequential, but the activities respectively pertaining to each of the two are interconnected: this synergy is of extreme importance for robust cataloguing. As new tracks arrive to the processing centre, there are several processes and cross-checks to understand if they belong to non-catalogued objects (for build-up) or if they are instead related to already existing RSOs (for maintenance). All the processing steps of build-up and maintenance form a scheme known as **cataloguing chain** [53].

The heart of the build-up phase is the analysis of the measurements to gather those belonging to the same object (**observation association** or **correlation**) and the determination of orbital properties via a fit of the data (**orbit determination**), to finally issue a new RSO in the catalogue. Observation association/correlation can be deemed straightforward for tracking data, but becomes rather challenging in survey activities as the identity of the observed objects is unknown at first. Track association is a crucial step in the cataloguing process as in general an orbit cannot be accurately estimated from a single track [34]. As this association problem involves tracks, it is usually defined as **track-to-track** correlation/association [53]. In past works regarding SST topics, the problem was referred to as observation-to-observation association/correlation [54], while the term track was used to indicate the orbit of an RSO in a catalogue. In the following dissertation, the well-established estimation of the state of an RSO is referred to as **orbit**. Depending on the quantity and quality of the a priori knowledge of an object, the inferral of the orbital state can follow Initial Orbit Determination (IOD) (when there is lack of a-priori information) or Orbit Determination (OD) algorithms [53]; in general, IOD is used to retrieve a first guess on an orbit, which is subsequently refined via OD. Classical OD methods include the batch least-squares estimator, in which measurements are clustered and processed together in a single time, or sequential estimators, which are

basically state observers (or filters) which update the solution sequentially by taking one measurement at a time. Any OD process, along with the estimate of the orbital state, provides an associated covariance matrix, expressing the uncertainty of the estimation associated with measurements noise or uncertainty in the dynamical modelling.

Track-to-track association is a NP-hard (Non-deterministic Polynomial-time hard) combinational optimisation problem, which means that the computational cost increases exponentially with the number of objects. It is currently an active area of research, with different strategies to tackle the problem, as brute-force approaches are generally computational unaffordable: this is particularly true in operational scenarios, where run-time performance shall be maximised in order to be able to process data in real time. This also entails that manual operations shall be avoided and the association tasks completely automatised, in order not to lose an important fraction of the survey sensing data. Different methodologies have been proposed so far to tackle the problem. Only a few of them will be mentioned here, as track-to-track correlation is not the main scope of this dissertation but is still a part of it. Nonetheless, the following description is useful to introduce some concepts that are largely employed in SST research and operations and that are useful to pose some basis for the discussion in the next chapter. Pastor et al. [55] proposed an algorithm in an association framework, in which tracks are at first associated to generate a so called **hypothesis** of association. Each hypothesis is scored based on the likelihood of the correlation and, as more tracks are processed, new hypotheses are generated either associating new tracks or adding them to previous ones. This process generates a so-called **association tree**. The tree can be pruned if hypotheses are demonstrated to wrong or branches of hypotheses can be merged if proven to belong to the same shared object. Siminski et al. [56] also developed an association framework employing the Mahalanobis distance as a metric for the correlation likelihood. The Mahalanobis distance is a statistical quantity that is widely used in these kinds of problems and represents the distance between a point and a distribution. The work also made use of Constrained Admissible Regions (CARs), another very popular concept in SST research first introduced by Milani et al. [36]. An admissible region can be defined as the set of physically acceptable orbits where an object might lie according to its observations; if constraints on some orbital parameters (i.e. semi-major axis, eccentricity) are enforced, then it shall be called a constrained admissible region.

The association/correlation problem is declined also in other forms and solved in both build-up and maintenance phase. When a track needs to be compared against an assessed orbit, to see if it might belong to it, the association is usually defined as **track-to-orbit** correlation. The problem can be cast in two domains: in the measurements domain, when

the track is compared against synthetic measurements generated from the orbit [53], or in the orbit domain, when the track undergoes IOD/OD and the estimated orbital state is subsequently analysed with respect to the catalogued element [57] [58]. Track-to-orbit association is typical in the first steps of the build-up phase: as a new track arrives to the processing station, it is first compared against established orbits to see if it belongs to an already catalogued object and so to avoid initialising a duplicated object. The last correlation problem is **orbit-to-orbit** association, which is used to compare two established objects. The techniques afferent to this category are generally used to cross-correlate two catalogues for quality control or for self-correlation to seek for any duplicate object [53].

1.6. The impact of manoeuvring objects on SST activities

The sources of the generation of new RSO have been widely discussed so far (launch events, intentional release of mission-related objects, on-orbit fragmentation events). However, when dealing with catalogue build-up activities, a new potential RSO might be detected if an operational spacecraft performs an on-orbit manoeuvre. As a manoeuvre results in a change of the satellite orbital elements, if no action is taken to detect and characterise it, an already catalogued object would then be detected as *new* when observing it again. Examples of typical manoeuvres done in Earth orbits are Station Keeping (SK), orbit raising or lowering and the aforementioned collision avoidance manoeuvres. Typical station keeping manoeuvres for GEO satellites are the North-South (NS) and the East-West (EW) manoeuvres. The first ones are required to counteract the effect of perturbations (mainly third body effects) on inclination, while the second are done in order not to cross the boundaries of the assigned longitude slot, as a natural drift due to Earth's obliquity and solar radiation pressure leads bodies towards the equilibrium points located at 73° E and 104° W. Similarly, also navigation satellites in NSO or other constellation satellites perform regular manoeuvres to keep their formation. Earth observation satellites in LEO, usually at altitudes comprised between 700 and 800 km, have to perform regular SK to counteract the natural decay induced by drag. Orbit raising or lowering manoeuvres are instead intended to move a spacecraft onto another co-planar orbit: an example can be a transfer from LEO to GEO via a GTO.

To provide some references, GEO satellites with chemical thrusters can perform regular station keeping burns at intervals ranging from once a week up to once every couple of months, depending on the propulsion system and on the properties of the satellite itself

[59]. Spacecrafts equipped with electric thrusters usually perform longer burns but way more frequently, even multiple times a day. Constellation satellites in LEO can perform a burn every couple of weeks in order to correct their mean anomaly and keep the designed arrangement [60]. If one considers these manoeuvring frequencies for all the satellites in the aforementioned classes, it is clear that manoeuvres constitute a big share in the sources of potential detection of new resident space objects [35]. The **manoeuvre detection problem** is generally coupled with **estimation** (in terms of magnitude, direction, duration, epoch), which is required in the orbit determination processes to update the new properties of the RSO. Manoeuvres represent a puzzling problem in cataloguing activities, because if not correctly detected and taken into account, both in build-up and maintenance, issues may arise. The track/orbit associations done with survey data are deeply impacted by an object performing a manoeuvre. In the case of track-to-orbit correlation, when an uncorrelated track of a post-manoeuvre orbit is compared against objects in the catalogue, unless the latter takes into account the manoeuvre plan (if reported by the satellite operators to the SST operators), any association will generally fail for burns with sufficiently high magnitude and after enough time to impact the orbital state. If nothing is done to take manoeuvres into account, as more post-manoeuvre tracks arrive to the SST processing stations they will be likely correlated, eventually giving rise to a new object in the catalogue. In tracking activities instead, the problem is slightly relieved as there is generally no need to correlate observations, leading to simpler manoeuvre detection. The estimation problem however is still challenging and of crucial importance: as example, if a manoeuvre is not taken into account when performing orbit determination, the resulting estimation will lack of accuracy and not represent the true trajectory of the spacecraft. The worst condition that might occur in tracking scenarios is having observability issues: if a manoeuvre is not detected and estimated, the sensor might not be tasked to be pointed in the correct direction, making the RSO fall outside its field of view and resulting in a loss or in ambiguities.

These considerations show the two major effects that unaccounted manoeuvres can have on catalogues: **duplication of objects** and **degradation of the precision** of the orbital states. They both lead to a loss in accuracy of a catalogue, which is reflected on the overall quality of the services provided by a SST operator. The consequences might be even extremely dangerous: as example, high-risk collision events might not be predicted sufficiently in advance or re-entry analyses might be completely imprecise. It is then clear that an automated routine to detect and estimate manoeuvres shall be properly integrated within the cataloguing chain, to improve the robustness of both build-up and maintenance phase and the overall accuracy of the catalogue.

1.7. Scope of the thesis

The **scope of the thesis** is to present a novel and operationally feasible methodology for manoeuvre detection and estimation, which shall be included as part of maintenance chain for RSOs. The methodology is conceived for a foreseen real time application, so particular care is given to its computational efficiency. Manoeuvre detection and estimation are posed as a track-to-orbit association problem between the orbit of an RSO, estimated some days before the manoeuvre, and a set of uncorrelated tracks, received afterwards. Manoeuvre estimation, which does not require any a-priori information of the latter, is a **two-step process**:

1. starting from the UCTs and the pre-manoeuvre orbit, a **first guess** for the manoeuvre is estimated employing a batch-least squares parameter estimation method with a simple dynamical model.

2. after having obtained the first guess, a **refined** manoeuvre estimation and post-manoeuvre orbit are computed via high-fidelity batch least-squares orbit determination.

As already mentioned, due to the impact of the manoeuvre on orbital dynamics, most post-manoeuvre tracks will not be correlated against any object in the catalogue. Such tracks, if compared to the pre-manoeuvre orbit in the measurements space, can show high residuals (which are the difference between true and predicted observations). Hence, the latter are employed in the detection strategy, where the occurrence of a manoeuvre is determined when certain thresholds are exceeded. The potential manoeuvre is estimated at first by following an optimal control approach, where the velocity increase (i.e., a ΔV) is used within a cost function, depending on the measurements and on the pre-manoeuvre orbit, to be minimised. This algorithm is an evolution, adaptation and extension of a methodology presented by Pastor et. al [35]. Differently from the previous work, focused on the GEO regime, the work presented here targets LEO objects, subject to faster and more non-linear dynamics; to this aim, the development of an **improved propagation model** for the manoeuvre estimation process is presented with the goal of minimising the associated computational cost while maintaining reasonable accuracy for the LEO regime. This task represents of the major contributions of the following dissertation.

The result of the estimation is a pool of possible solutions, from which a proper **a-priori estimate** is chosen according to a selection criterion based on the weighted errors of the residuals and on the control effort. The selection strategy is an evolution of the one proposed in GEO. Figure 1.7 below presents a flow chart of the cataloguing maintenance

phase, in which the role of the proposed algorithm to get the first manoeuvre estimate is highlighted.

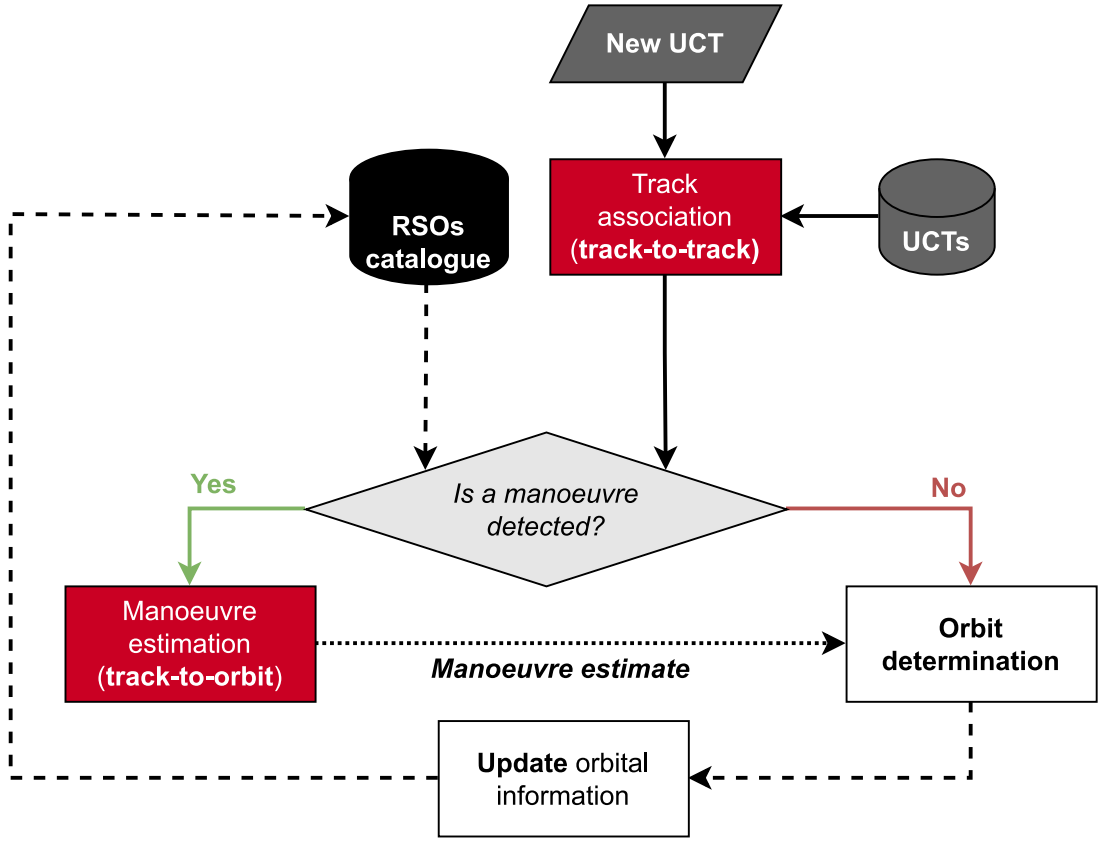

Figure 1.7: Catalogue maintenance accounting for manoeuvres.

The methodology is presented for a single-satellite scenario, considering just one RSO orbit and sets of tracks belonging to the very same object. Nonetheless, it can be trivially extended to a wider **multi-target association framework**. In fact, if one considers a typical surveillance scenario with multiple catalogued orbits, the estimated manoeuvres can represent a preliminary link, or hypothesis, established between the UCTs and the object (with its pre-manoeuvre orbit). The union of these hypotheses builds up an association tree, which needs to be evaluated and pruned in order to finally promote the best correlation which connects the involved catalogued orbit and the processed observation data, being able to determine which object performed a manoeuvre.

Following the proposed methodology, the manoeuvre detection time is considerably reduced since no new object initiation is performed (as done instead in orbit-to-orbit associations), benefiting the whole cataloguing process and its quality. Nonetheless, the estimation of the post-manoeuvre orbit and the manoeuvre itself has mediocre accuracy if only measurements from a single post-manoeuvre track are used, losing the ability to

associate future tracks. Hence, the track-to-orbit correlation process must be preceded by a track-to-track association step (developed by Pastor et al. [55]), used to cluster together enough post-manoeuvre tracks corresponding to the same RSO. This is of course trivial in scenarios where tracks are known to belong to the same object, but is a fundamental step in the multi-target multi-sensor association framework. The employment of the track-to-track association process allows to reach estimation accuracy (for both the manoeuvre and post-manoeuvre orbit) analogous to no-manoeuvre scenarios if enough tracks are gathered.

Tests are performed considering a simulation scenario including **radar tracks** and the orbit of a single satellite, providing a clear understanding of the performances of the methodology and serving as a basis for the development of the multi-target association framework. Results are presented and discussed, emphasising the benefits and the limitations of the overall approach.

1.8. Structure of the thesis

The dissertation is structured in 5 chapters.

- Chapter 1 introduces the manoeuvre detection and estimation problem and its impact on SST activities.
- Chapter 2 provides a description of the state-of-the-art methodologies.
- Chapter 3 presents the track-to-orbit correlation methodology for manoeuvre detection and estimation, as well as development of the dynamical model tailored for the LEO regime.
- Chapter 4 describes the simulation scenario used for testing the algorithm and reports the obtained results, providing a comprehensive description of them.
- Chapter 5 is dedicated to conclusions, to the description of the current status of the work, and finally to future developments.

2 | State of the art

2.1. Introduction

Spacecraft manoeuvre detection and estimation is an area of active research. This section presents some of the methodologies proposed so far in the literature giving a brief description about their core, in order to delineate what are the available tools and strategies that can be implemented to tackle the problem.

The methodologies can be at first divided into two categories:

1. based on **direct SST observations**
2. based on **historical data** (mainly TLEs)

The first category groups all the methodologies aimed at detecting and estimating a manoeuvre with observations (or derived orbit estimations) obtained from SST sensors, both ground-based (in the vast majority of the cases) and space-based. The second category gathers instead the algorithms which are devoted to the processing of long time histories of orbital parameters of a satellite. The most common type of historical data is represented by TLEs, due to their simplicity, availability and popularity.

This chapter will be focused on the on the first category, as it is the research topic of this dissertation. Before starting the presentation of the state-of-the-art algorithms for manoeuvre detection and estimation from observations, it is useful to subdivide the group into two major classes: methodologies for **surveillance data** and those developed for **tracking data**. The main difference between the two is that in the tracking case the problem of correlating tracks or orbits (meaning to cluster tracks of the same shared objects or to assign tracks to a known orbit) is generally deemed to be solved; in the surveillance case, the task of detecting and estimating a manoeuvre shall be integrated within the data association framework, making the whole problem more challenging. One of the most critical aspects in this scenario is that tracks can be separated by large observation gaps (in the order of days or weeks), meaning that if a manoeuvre takes place in these time windows, it will be very likely to observe large position and velocity

discrepancies between subsequent tracks: the capability of correlation becomes minimum if a robust manoeuvre detection scheme is not taken into account. The availability of the measurements strongly depends on the type, location and tasking of the SST sensors which, coupled with the orbital properties of a satellite (mainly period and inclination), determine the visibility windows. Nevertheless, it is important to remind that even in case of non-manoeuvring objects the correlation of UCTs is a hard task, due to uncertainties in state estimation coming from sensor and process noise. Apart from this classification, the development of a manoeuvre detection and estimation algorithm can be influenced by the orbital region of applicability. In fact, this can impact the models that shall be used for the description of the orbital motion, the type of available measurements (radar for lower altitudes, optical for higher altitudes), as well as the typical manoeuvre patterns followed by the satellites. Similarly, also the intended use of the methodology can cast some constraints: as example, if the algorithm is supposed to co-operate for a real-time catalogue maintenance, the run-time performance becomes of key importance, as the amount of data to be processed can become extremely large. On the other hand, if manoeuvre detection and estimation shall only be implemented as a post-processing analysis, it might be possible to develop more sophisticated and precise tools at the cost of greater computational effort.

2.2. Detection and estimation with surveillance data

One of the first and most important works in this field was presented by Holzinger et al. [61], who proposed a methodology within the problems of a track-to-orbit and orbit-to-orbit correlation. The concepts presented in this paper have been reprised many times by several authors, with further modifications and novel implementations. The joint data association/manoeuvre detection problem is cast as an Optimal Control Problem (OCP) in which the distance metric is built to be proportional to the thrust control effort of a satellite (assumed to be continuous). The selection of this parameter is based on the observation that spacecrafts generally perform optimal or sub-optimal manoeuvres in order to minimise propellant consumption (minimum energy expenditure), entailing that associations of tracks which are close in the control metric sense are more likely. The main goal is therefore not to perfectly estimate the manoeuvre (the true ΔV is upper bounded by the performance function through a simple inequality), but to score and test the generated hypotheses to decide whether an incoming observation could have been affected by a manoeuvre. The methodology is validated and tested for a geostationary cluster. Jaunzemis et. al [62] went on with the optimal control problem approach by implementing a binary hypothesis testing framework for manoeuvre detection within track association. This tool

allows to detect anomalies (hence manoeuvres) in associations of tracks by evaluating a pair of Probability Distribution Functions (PDFs) based on the control effort metric; the integration of these PDFs provides the probabilities of false alarm and of missed detection of a manoeuvre. This strategy, which employs Gaussian mixture models to describe state uncertainties, is compared with tests based on the Mahalanobis distance, which is proven to be less effective at detecting manoeuvres, especially for large observation gaps. Siminski et al. [63] also followed the optimal control approach: in this case, the core of the methodology is to extend the distribution of possible post-manoeuvre states according to the concept of admissible region, which is in this case delimited by a maximum ΔV threshold. When first initialising an association hypothesis between a track and a orbit, the post-manoeuvre state is taken in the admissible region as the one which minimises ΔV. In order to completely reconstruct the orbit after the manoeuvre, each hypothesis must be tested against new incoming observations to eventually verify and promote it. Using the same optimal control theory foundations, Serra et al. [64] researched manoeuvre detection and estimation within track-to-orbit associations with optical observations. The idea of the authors is to solve the association problem as an optimal control problem by implementing the control effort metric in the orbit space, so estimating states just from single tracklets. As single optical observations are not sufficient to perform a full estimation, the concept of admissible regions (in terms of range and range-rate) is introduced in order to limit the set of compliant and physically feasible orbits, therefore building up a probabilistic IOD process. The admissible regions are inferred from the line-of-sight measurements, from which it is possible to determine the allowed semi-major axis range (connected to the orbital energy) and the maximum eccentricity. The region is subsequently convexificated in order to drive the method to convergence. A work which might be considered similar, even if not fully reprising Holzinger's theory, was presented by Dutta and Raquepas [65], introducing a stochastic optimal control perspective to the problem of manoeuvre detection within the track association problem. At first, an initial population of samples representing the pre-manoeuvre state (related to a pre-manoeuvre track) are generated following Gaussian statistics and subsequently propagated following non-linear dynamics (using Monte Carlo simulations) with the possibility of having either an impulsive or a low thrust manoeuvre (modelled as series of Dirac's deltas). These random post-manoeuvre state are compared in terms of statistics with the true post-manoeuvre states (available at the end of an observation gap), helping identifying and estimating the classes of manoeuvres that are able to correctly steer the initial probability distribution to the final observed one. In order to reduce the computational effort related to detection and estimation, the authors developed a linearised optimisation tool to provide a quicker estimate of the minimum stochastic control effort.

A different path that was undertaken to tackle manoeuvre detection and estimation within the data association problem stems from conjunction analysis. In fact, the basis of this theory allows to make an analogy between the track/orbit correlation problem and the assessment of a collision between two objects. Hill [66] proposed a methodology for track-to-orbit associations with optical tracklets. When a new track is not correlated against any established object, it undergoes a process of preliminary IOD (with two or four angle pairs) cast as an optimisation problem: making the assumption of minimum fuel consumption, the goal is to find the orbit that passes closest to the trajectory of another satellite. The results of the process are a miss distance and a velocity difference, that can be mapped into an error metric. The manoeuvre is hypothesised as the one that minimises such function; subsequently, the orbital state vector obtained by IOD is refined employing a linear batch least-squares estimator and finally the force vector representing the manoeuvre is estimated starting from the equations of motion.

Recent works proposed the possibility of detecting a manoeuvre in the data association problem via statistical inference, processing data about previous satellites' manoeuvres. The core idea backing up these methodologies is that some types of satellites (generally in GEO) show repetitive patterns (as example, station keeping), whose recognition, if characterised in a statistical fashion, can be efficiently exploited to solve the problem. The literature generally defines this methodologies as part of the *heuristics* category. In the publications [63] and [67], Siminski et al., along with the optimal control approach for manoeuvre estimation, proposed a novel methodology which includes information about historical satellite data. A freshly received track is compared against catalogued objects employing a statistical technique known as Kernel Density Estimator (KDE): this allows to determine the density function of the probability that a post-manoeuvre state can be associated to a given pre-manoeuvre orbit. The KDE processes historical data and is able to recognise recurrent manoeuvre patterns. Each manoeuvre is represented in the form of a feature vector, which includes the mean orbital elements of the pre and post-manoeuvre states, the variation in eccentricity and the time elapsed from the previous manoeuvres contained in the historical data. The hypothesised manoeuvre (which shall be further verified as more tracks are processed) is taken as the one that maximises the density function estimated by the KDE. The algorithm is applied to satellites in GEO using optical observations. Escribano et al. [68] [69] proposed a novel formulation for manoeuvre detection within the track-to-track association problem following a Stochastic Hybrid System (SHS) framework, whose flexibility allows to fuse information coming from very different sources, such as historical data and optimal control theory. The state of the system is estimated from observations via a Sequential Monte Carlo (SMC) scheme,

employed to address the high-non linearity of the dynamics in a bi-modal fashion, for which either a non-manoeuvring or a manoeuvring mode can be triggered. When a manoeuvre is detected, the estimation is done via a Monte Carlo Markov Chain (MCMC) algorithm, as the dynamics of the manoeuvring object cannot be properly characterised. This method allows to disregard the underlying physical process and, given the available measurements, provides the samples of the probability distribution function of the post manoeuvre state, known as the a-posteriori distribution. The distribution is eventually limited by defining an admissible region based on the control effort required to reach certain range and range-rate values, which is expressed as a ΔV sum of two single Keplerian burns connecting the two tracks. The resulting probability distribution coming from MCMC is scaled to include information about the computed ΔV and, if available, about previous manoeuvres through a kernel density estimator (similarly to [67]). Each hypothesis is finally scored using a likelihood function and the chain is repeated to prune, promote and finally confirm the the most probable manoeuvre as more data is processed by the system. The algorithm is tested simulating optical observations for an object in GEO.

Finally, it is important to mention that the work presented by Pastor et al. [35], which serves as the basis of this thesis, also presented a second manoeuvre estimation method based on an orbit-to-orbit association problem. After having initialised an orbit from the received post-manoeuvre UCTs (having gathered enough via track-to-track association and performing OD), a manoeuvre is estimated by hypothesising a double impulsive burn connecting the pre-manoeuvre and the post-manoeuvre orbit. The two impulses are characterised as perturbations to the orbital states via linear dynamics. Also in this case, a multi target association framework is set up and so multiple hypotheses for the manoeuvre, evaluated in terms of ΔV, are retained. The algorithm is tested with simulated data and real optical observations of GEO satellites coming from the Spanish Space Surveillance and Tracking Operations Centre (S3TOC).

2.3. Detection and estimation with tracking data

The problem of manoeuvre detection and estimation is generally not only a concern of SST, but it impacts other fields which present possible tracking scenarios. For this reason, the literature on the topic is very vast [70] and applications are found also in the automotive, aeronautics and naval field (among many others). As this dissertation is concerned with space scenarios, the following section will be just focused on the methodologies that have been developed for SST activities.

Most of the strategies developed for tracking scenarios might be defined as manoeuvre

detection filters (MDFs) [71]. These tools are OD sequential estimators (for which the Kalman filter can be considered a progenitor) including some strategy or metric for manoeuvre detection. In general, these methods only provide the estimation of the state (both pre and post-manoeuvre) but not one of the manoeuvre; the magnitude and direction of the latter can be inferred afterwards through various techniques. The capabilities of detection and estimation are crucial because, as already mentioned in Section 1.6, unaccounted manoeuvres can severely degrade the performances of any OD process. It is worth mentioning that these algorithms, even if specifically developed for tracking scenarios, might find applications also in surveillance cases if posed in a wider data correlation problem.

One of the first manoeuvre detection strategies was presented by Woodburn et al. [72], developing a methodology to be implemented in any sequential orbit determination process. A filter is used to estimate states as measurements are available; whenever a manoeuvre is detected (due to increased residuals), the OD process continues to go on but with an artificially inflated covariance, taking into account the higher uncertainty in the velocity sub-matrix. The covariance inflation is a technique used to reduce the confidence of a filter, so that it can process measurements of the post-manoeuvre tracks and converge towards the new orbit. Tracking data is processed after the manoeuvre epoch until the confidence in the state estimation returns to acceptable levels. At this point, the estimated data are used to initialise a smoothing process, going backwards in time until the pre-manoeuvre time. The manoeuvre is finally estimated from the difference between the smoothed pre and post-manoeuvre states. Another methodology with covariance inflation was published by Li et al. [73], implementing a Strong Unscented Kalman Filter (SUKF) to counteract the performance degradation caused by the sudden change of state represented by manoeuvres. The key of strong tracking filters is to use a time-variant fading factor, which can be evaluated in real time from the measurement innovation (i.e. the residual between true observations and predicted ones), in order to inflate the predicted error covariance and avoid the divergence of the filter. The metric which determines the occurrence of a manoeuvre in this case is based on ranging measurements. The main advantage of these methods is their simple implementation; however, the drawbacks are that the selection of the covariance inflation factors are not derived from any physical consideration and that it is assumed to obtain good post-manoeuvre states quickly, which is in general not true.

A work still pertaining to the manoeuvre detection filter class is by Kelecy and Jah [74], who proposed a simple methodology to detect unaccounted in-track burns. This algorithm relies on the sequential estimator and smoother of the the Orbit Determination

Toolkit (ODTK) [75], as the manoeuvre detection metric is based on the ratio between the differences in the estimated and smoothed states, as well as their covariance, across a manoeuvre event. The strategy is tested for a LEO satellite and manoeuvres are estimated starting from the variations of the semi-major axis, assuming they can occur due to either drag or in-track burns. Variations in the semi-major axis are a reflection of variations in the orbital energy, which are indeed related to a ΔV. The study also demonstrates the complication of determining the manoeuvre epoch and the challenges set by low thrust manoeuvres, which in some cases cannot be discriminated from other non-conservative perturbations. Huang et al. [76] developed a strategy specific for objects in LEO having orbital state already estimated with sufficient accuracy. Assuming minimum ΔV impulsive burns, the authors propose a simple analytical methodology to hypothesise which kind of manoeuvre a spacecraft has performed by analysing the orbital elements. Two options are available: a single tangential impulse or double tangential kick at perigee and apogee. If it is assessed at first that a single tangential burn might have occurred, Second Order Cone Programming (SOCP) is employed to refine orbit determination and estimate the manoeuvre. Vazquez et al. [71] presented a methodology to be implemented in an operational scenario and validated it using real radar data for two satellites in LEO (Sentinel 1-A and Swarm C) coming from the Spanish Space Surveillance and Tracking Surveillance Radar (S3TSR). The idea is to employ an Unscented Kalman Filter (UKF) to estimate orbital states from tracks even with large observation gaps (up to 3 days) and detect a manoeuvre by evaluating a figure of merit based on observation residuals and state covariance. The estimation process is based on the OREKIT orbit propagator and includes a smoother to better process data when larger batches of measurements are available. The methodology also makes use of Reachable Sets (RS), which are defined as following: *"given a system that evolves from an initial condition (or set of initial conditions), and possibly has some control inputs, the reachable set is the set of states at which the system can arrive (i.e., the states that can be reached) at a given time"*. This concept is used to make two a-posteriori analyses: the first one employs real and simulated attributables (which are fits of measurements providing single values at the middle epoch of an observation; refer to [36] for a more comprehensive view) to discriminate a post-manoeuvred state from a ballistic one employing the Mahalanobis distance; the second one proposes a ΔV metric in a stochastic optimal control framework, opposed to the Mahalanobis distance, to the same aim. Another manoeuvre detection filter was proposed by Bergmann et al. [77] to detect and characterise manoeuvres of objects in GEO using optical measurements. The methodology employs two non-linear sequential estimators (EKF and Unscented Kalman Filter, UKF) and is able to detect manoeuvres employing a metric very similar to [71] (still based on observation residuals and covariance). Once

that a burn is identified, the pre and post-manoeuvre states are refined via a batch least squares estimator and subsequently conjunction analysis is employed to determine the ΔV components (as done by Hill [66]). A similar approach was followed by Herzog et al. (2017) [78], which exploited optical observations of EUMETSAT's GEO satellites. Two predicted orbital states, defined at two different epochs, are both propagated in a span defined by the two reference times; simultaneously, a probability of collision is computed at each step by considering a collision radius equal to double the satellite's radius (as, theoretically, the collision is between the satellite and itself) and Gaussian distributions for uncertainties on the reference states. A manoeuvre is assumed to be detected if the time plot of the probability of collision presents a clear isolated peak surpassing a given threshold.

An interesting approach for MDFs that has gained popularity over the years is the so called Multiple Model Adaptive Estimation (MMAE) [79], built to tackle the non-linearity and the spacecraft motion-mode uncertainty. The term MMAE (or more simply Multiple Models, MM) refers to any formulation that provides an estimation formulated over multiple models for the dynamics, that can be either static or adaptive (according to some varying parameters), in order to augment the description of the motion of a spacecraft. There are several ways to define and combine these multiple models, but in general a MMAE algorithm uses one or several families of filters and combine their outputs to improve the overall estimate. The National Research Council of the United States widely supports the development of such methods when dealing with non-linear filtering problems. In fact, in a publication aimed at assessing the SPACECOM's astrodynamic standards [80], it is stated that: *"[...] because it can take some time for a filter to settle down, such 'state-augmented' or 'multiple model' filtering techniques can be particularly valuable for converging sooner with limited data."*

A family of algorithms belonging to the MMAE is the so-called Input Detection and Estimation (IDE) methods. The dynamical model used for the state estimation is set side by side with an estimator which is capable of detecting if a manoeuvre (or any other sort of anomaly) has occurred and predict its characteristics, in order to provide them as a feedback and improve the overall state estimation. Ko and Scheeres [81] presented an algorithm based on an Extended Kalman filter with the use of the Thrust Fourier Coefficients (TFCs). The authors demonstrated that it is possible to connect any two arbitrary orbital states via an equivalent manoeuvre that can be expressed as a Fourier series of 14 terms (function of the eccentric anomaly). The unknown manoeuvre is mathematically expressed as a control acceleration and the coefficients of the Fourier series (namely, the TFCs) are determined analytically from the pre and post-manoeuvre states (averaging

Gauss's planetary equations). The state estimator is able to recognise a manoeuvre by detecting any measurement residual exceeding a defined threshold. Another family of MMAE was introduced by Guang et. al [82], who presented the concept of the Variable Structure Estimator (VSE). Orbit determination is performed via an EKF, which is put side by side with a manoeuvre observer: this is a linear estimator, able to retrieve the thrust vector at each step starting from the information about state estimates at the current and previous integration times. The manoeuvre estimator is triggered whenever the measurements' residuals become sufficiently large. The estimated control finally provides a feedback to the OD process to have more accurate estimation during the manoeuvre and after it. A similar group of methodologies is represented by the joint dynamic/kinematic filters, as the algorithm presented by Ye et. al [83]. The authors propose two parallel filters to perform state estimation: the first one, called primary, is a high-fidelity orbital model and is used to provide high-precision tracking results; the second, called auxiliary, on the other hand employs a simple Markov process to estimate the unknown acceleration of the spacecraft (namely a manoeuvre). In ballistic conditions, the primary is used for tracking, while the auxiliary filter is used to detect manoeuvres (with a metric defined on the estimated semi-major axis), as it is more sensible to them. Once that a manoeuvre is detected, the tracking can continue with the auxiliary filter or the primary can be re-started with a new initial solution based on the post-manoeuvre measurements.

Interacting Multiple Models (IMM) are a further expression of the MMAE. In this framework, several filters employing different dynamical models are run in parallel performing state estimation. Each filter is associated to a given motion mode of the target and such mode has, at each time step, a specified probability of being in effect. The outputs of the filters are finally combined according to these probabilities, which are usually modelled as a Markov process: this means that a probability at time step k only depends on the variables at time $k-1$. Lam [84] implemented IMM to address unpredictable and unknown manoeuvring plans. In this case, state estimation (with EKFs) is done for both a normal orbiting mode and a manoeuvring mode. The first mode only includes position and velocity estimation, while the second one has also acceleration, which provides an estimate of the unknown manoeuvre. The probability of each mode is based on a likelihood function determined by measurements residuals and covariance. Jia et al. [85] followed a similar path developing an IMM Cubature Kalman Filter (CKF) for tracking and manoeuvre detection of a GEO spacecraft simulating Space Based Optical (SBO) sensors. Another related work is by Zucchelli et. al [86], in which the Interactive Multiple Models filters are posed in a larger multi-target association framework (with promotion, pruning and merging of hypotheses). Here, uncertainty propagation is performed via a

Multi Fidelity (MF) method. The latter combines a hierarchy of models with varying fidelity to obtain highly accurate yet fast predictions; in general, these methods make use of a few iterations of the most accurate (and therefore expensive) models, and many iterations of the least accurate, but fastest, models. Goff et al. [87] developed a filter-through IMM methodology. The state estimation is done for a single non-manoeuvring mode and a family of manoeuvring modes, each one associated with a given level of covariance inflation: the higher the expected manoeuvre magnitude, the higher the covariance. The measurements' residuals and covariance define both the probability of the modes (via a likelihood function) and the manoeuvre detection metric; when the latter overpasses a certain threshold, the IMM are triggered. The covariance inflation benefits the filters' convergence, whose final outputs are combined according to the model probabilities. In a parallel work [88], the same authors proposed a manoeuvre estimation method to reject the inaccuracies that might still be present in any post-manoeuvre orbit estimation. In a conjunction assessment fashion, a set of points close to the closest approach between the pre and post-manoeuvre orbits are considered with their corresponding ΔV components, retrieved by the difference in velocity of the states. Summing up each velocity increment to each point in the pre-manoeuvre set, a range of post-manoeuvre orbits is propagated. The true solution is finally taken as the one that minimises a cost function based on the observation residuals.

Manoeuvre detection filters have also been developed following the optimal control theory. The most famous work in this field is by Lubey [89]. The author proposed a sequential estimator to reconstruct and compensate for mismodelled or unmodelled dynamics, such an unknown manoeuvre, by solving an optimal control problem based on the distance metrics proposed by Holzinger [61]. The same metrics are also employed for manoeuvre detection. The filter is known as Optimal Control Based Estimator (OCBE) and can be intended as a generalisation of the Kalman filter. The methodology has been recently implemented by Greaves and Scheeres [90] in order to detect manoeuvres of cislunar vehicles starting from simulated optical measurements taken from the L_2 point. This work also foresees the future importance of cislunar situational awareness, as the increased international interest in the development of this region will lead to the generation of traffic and debris. Another application of Lubey's OCBE was found in the work by Ravago and Jones [91] which employed a Labelled Multi-Bernoulli filter (a form of recursive filter), a tool that pertains to the discipline of multi-target tracking. Through this algorithm, it is possible to keep track of different moving objects in a given scenario by introducing the concept of Random Finite Sets (RFSs) [92] and by assigning a label (having a unique ID and the time of the *birth* of the target) to each object. In order to compute the probability

distribution functions of the target states, the filter performs a two-step estimation: at first, a prediction step with Bayesian statistics; in the second place, an update step which takes into account the available measurements to correct the prediction. This last phase entails active data association to assign observations to the correct object: the selected metric is the Mahalanobis distance, meaning that a measurement is correlated to the closest target in the Mahalanobis sense. The contribution of the OCBE is found in the update step, where it serves as the update engine for the state estimates and provides means of detecting and estimating a manoeuvre.

3 | Methodology for manoeuvre detection and estimation

This chapter is devoted to the development of the manoeuvre detection and estimation algorithm. Section 3.1 describes the employed methodology for detecting whether a manoeuvre has happened based on the residual of the observations. Afterwards, Section 3.2 presents the manoeuvre estimation algorithm, cast as a parameter estimation with an optimal control approach, to obtain the first manoeuvre guesses. The strategy to extract the most suitable first estimate among the pool of solutions (improved with respect to the previous work [35]) is reported in Section 3.2.2. Section 3.2.3 presents the development of a dynamical model for orbit propagation as required by the proposed estimation algorithm. The model is built over the previous one used for manoeuvre estimation of GEO objects [35], which employed linear dynamics.

3.1. Manoeuvre detection

As a spacecraft performs impulsive manoeuvres, due to the change in the velocity, a divergence in the residuals with respect to the pre-manoeuvre orbit is expected to be noticeable. The residuals represent the difference between the true measurements taken by a sensor and those predicted by an analytical model. This divergence is sought in the measurements space, therefore a comparison of tracks with observations reconstructed from the given pre-manoeuvre reference orbit is required. This choice is due to the requirements of real-time operations of the algorithm, which imply the necessity to detect a potential manoeuvre as soon as the first post-manoeuvre track arrives. However, since a post-manoeuvre orbit cannot be reliably estimated from a single track [93], it is essential to operate in the measurements space.

Consider the pre-manoeuvre orbit under analysis (with subscript A), estimated with pre-manoeuvre tracks. The ephemerides of such orbit can be propagated with a high-fidelity numerical propagator in time defined by the variable t, computing the trajectory of an extended state vector as:

$$\mathbf{y}_A(t) = [\mathbf{x}_A(t), \mathbf{p}_A(t)] \in \mathbb{R}^{(6+n_p)} \tag{3.1}$$

The first part of the vector, $\mathbf{x}_A(t) \in \mathbb{R}^6$, is the aggregation of the Cartesian position vector $\mathbf{r}_A(t) \in \mathbb{R}^3$ and velocity vector $\mathbf{v}_A(t) \in \mathbb{R}^3$. On the other hand, the vector $\mathbf{p}_A(t) \in \mathbb{R}^{n_p}$ is a set of dynamical parameters which have been estimated during the orbit determination process. The vector here considered is propagated in the GCRF frame.

Consider now a possible post-manoeuvre track. It can be decomposed into a set of observations $\{\mathbf{z}_k\}$, where each $\mathbf{z}_k = \mathbf{z}(t_k)$ is a vector containing separate measurements taken at the observation times t_k for $k = 1, \ldots, K$, with K being the total number of observations in the track.

The selected metric for manoeuvre detection is the **weighted root mean square residual** of each measurement type in the track with respect to the pre-manoeuvre orbit:

$$WRMS_i = \sqrt{\frac{1}{K}\sum_{k=1}^{K}\frac{\rho_{i,k}^2}{\sigma_i^2}} \tag{3.2}$$

where the index $i = 1, \ldots, I$ refers to the type of measurement (e.g., azimuth, elevation, range, range-rate). The term $\rho_{i,k} = z_{i,k} - \mathbf{h}(t_k, \mathbf{x}_A(t_k))$ represents the residual of the i-th type of measurement at the epoch of the k-th observation (t_k). The function $\mathbf{h}(t_k, \mathbf{x}_A(t_k))$ is an analytical model to reconstruct measurements starting from the state vector of the pre-manoeuvre orbit, described in Appendix A.2. The denominators σ_i are the standard deviations of the measurements, quantifying the expected 1-sigma noise of the sensor for a given measurement type.

Having defined such metric, a manoeuvre is expected to have occurred if the WRMS of a single track crosses a **threshold** called absolute WRMS threshold. The selection of its value is based on data observation, assuming the sensor measurement noise is properly characterised, and descends from a trade-off: the threshold should be sufficiently low to trigger true manoeuvre detection, but also sufficiently high to discard any possible outlier and avoid false manoeuvre detection. A challenging case for this approach is encountered when, in the case of low magnitude burns, the first post-manoeuvre track arrives closely to the manoeuvre epoch (in the order of 1-2 hours). As only a short time period after the manoeuvre has passed, the divergence of the observations could be not sufficiently high to overpass the threshold: the track would therefore resemble an outlier and not trigger the detection of a true manoeuvre. The robustness of the strategy is

improved, and the issue partially solved, with the application of a **secondary threshold** (as opposed to the **primary threshold**): if a post-manoeuvre track is detected through the primary threshold, the algorithm looks to the past to find tracks that exceed the secondary threshold. Since these past tracks are supposed to show a smaller divergence with respect to the one detected with the primary threshold (as a shorter time since manoeuvre has passed), the value of the secondary threshold should be lower than the primary. The selection of the values for the thresholds, as well as the time interval to look for post-manoeuvre tracks into the past when applying the secondary thresholds, will be discussed in Section 4.3. A scheme of the applied manoeuvre detection strategy is presented in Figure 3.1.

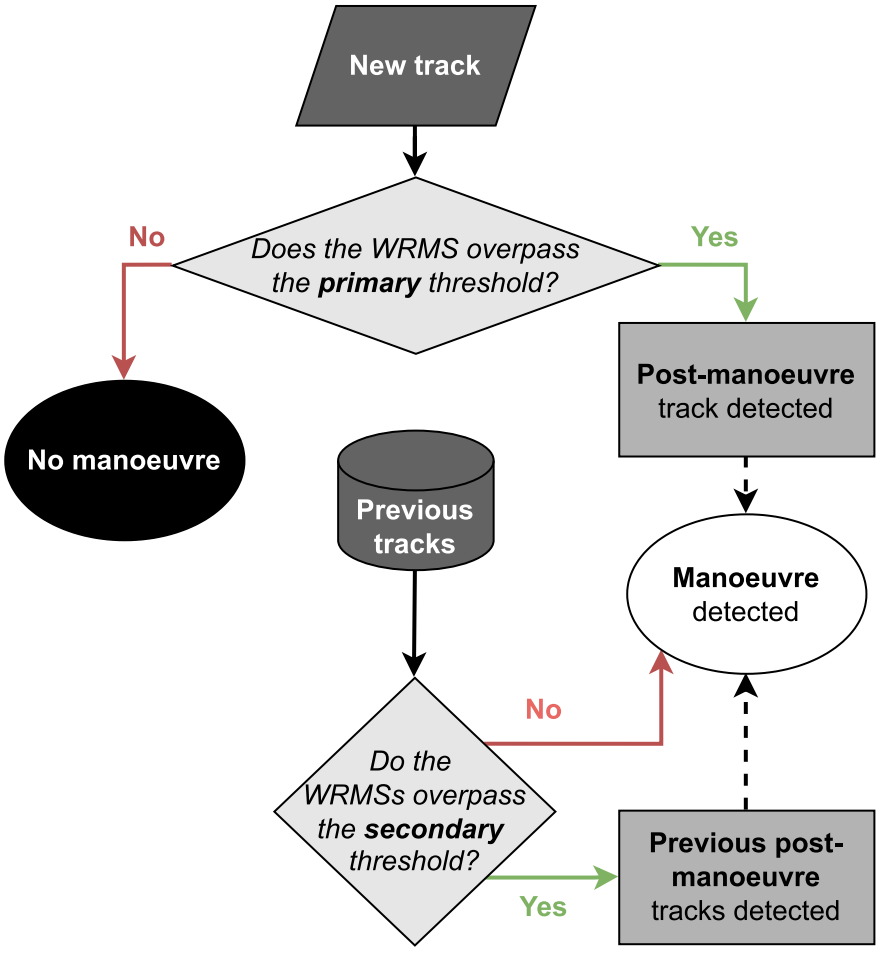

Figure 3.1: Manoeuvre detection scheme.

3.2. Manoeuvre estimation

3.2.1. Batch-least squares parameter estimation for first manoeuvre estimates

When a manoeuvre is detected via the manoeuvre detection algorithm, the latter provides a set of tracks which are labelled as post-manoeuvre. These can be decomposed into the observations $\{\mathbf{z}_l\}$, where each $\mathbf{z}_l = \mathbf{z}(t_l)$ contains all the measurements taken at the observation times t_l for $l = 1, \ldots, L$, with L being the total number of observations in all tracks. At a certain epoch, defined as t_M, an impulsive manoeuvre is assumed to take place. The pre-manoeuvre orbit $\mathbf{x}_A(t)$ will therefore drift towards $\mathbf{x}_B(t, \mathbf{u})$, named post-manoeuvre orbit (or also orbit B). Given the hypothesis of impulsive burn, the two orbits intersect at t_M: their position vectors $\mathbf{r}_A(t_M)$ and $\mathbf{r}_B(t_M)$ are the same, while the difference in velocity is given by the manoeuvre $\mathbf{u} \in \mathbb{R}^3$, such that $\mathbf{v}_B(t_M) - \mathbf{v}_A(t_M) = \mathbf{u}$. Having the pre-manoeuvre orbit and the post-manoeuvre tracks, the manoeuvre $\mathbf{u}$ occurring at t_M is found as the one that minimises the residuals of the true observations $\{\mathbf{z}_l\}$ with respect to the post-manoeuvre orbit $\mathbf{x}_B(t, \mathbf{u})$ (as represented in Figure 3.2). This methodology was already developed for manoeuvre estimation of GEO objects [35].

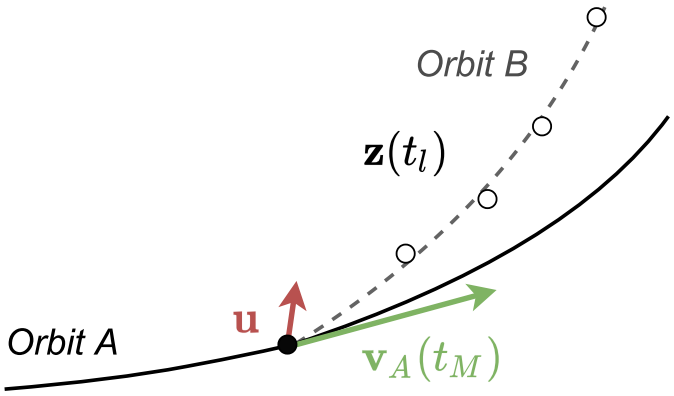

Figure 3.2: Graphical representation of the manoeuvre estimation method.

This is equivalent to a **parameter estimation problem** using $\mathbf{u}$ as solve-for parameters, while keeping t_M fixed to a given value, as it was proven that a joint estimation is unsatisfactory due to the non-linearities of the problem [35]. The residuals at each observation time t_l can be computed as $\boldsymbol{\rho}_l = \mathbf{z}(t_l) - \mathbf{h}(t_l, , \mathbf{x}_B(t_l, \mathbf{u}))$, which is a vector of dimension equal to the number of considered measurement types (denoted as I). As already stated in Section 3.1, the problem is cast in the measurements space since in general there are not enough post-manoeuvre tracks to reliably estimate $\mathbf{x}_B(t, \mathbf{u})$. The goal is to find the manoeuvre for which the weighted square of the difference between the predicted

observations and the true measurements becomes the smallest possible, or, rewording, the manoeuvre which best fits the observations in a least-squares of the residuals sense. This is achieved by minimising the following cost function:

$$J = \frac{1}{L}\sum_{l=1}^{L} \boldsymbol{\rho}_l^T W \boldsymbol{\rho}_l \tag{3.3}$$

Equation (3.3) is similar to Equation (3.2). The matrix $W \in \mathbb{R}^{I\times I}$ is the **weighting matrix**, which accounts for the expected errors of the measurements and puts into effect the non-dimensionalisation of the residuals. Assuming that the errors are non-correlated, W is a diagonal matrix with its components being the squared inverse of expected uncertainties σ_i of the measurements.

$$W = \begin{bmatrix} 1/\sigma_1^2 & & \dots & & 0 \\ \vdots & \ddots & & & \vdots \\ 0 & \dots & 1/\sigma_i^2 & \dots & 0 \\ \vdots & & & \ddots & \vdots \\ 0 & & \dots & & 1/\sigma_I^2 \end{bmatrix} \tag{3.4}$$

The cost function might be rewritten by considering a linearisation of the residuals with respect to a reference value for the manoeuvre $\mathbf{u}^*$ [7], such that:

$$\begin{aligned} \boldsymbol{\rho}_l &= \mathbf{z}_l - \mathbf{h}\left(t_l,\, \mathbf{x}_B\left(t_l\right)\right) \\ &\approx \left[\mathbf{z}_l - \mathbf{h}\left(t_l,\, \mathbf{x}_B\left(t_l,\, \mathbf{u}^*\right)\right)\right] - \left[\frac{\partial \mathbf{h}\left(t_l,\, \mathbf{x}_B\left(t_l,\, \mathbf{u}^*\right)\right)}{\partial \mathbf{u}} \cdot \left(\mathbf{u} - \mathbf{u}^*\right)\right] \\ &\approx \Delta\mathbf{z}_l - G_l \cdot \Delta\mathbf{u} \end{aligned} \tag{3.5}$$

Hence, J becomes a function of the **reference manoeuvre** $\mathbf{u}^*$ and of the **correction** $\Delta\mathbf{u}$:

$$J \approx \frac{1}{L}\sum_{l=1}^{L} \left[\Delta\mathbf{z}_l - G_l \cdot \Delta\mathbf{u}\right]^T W \left[\Delta\mathbf{z}_l - G_l \cdot \Delta\mathbf{u}\right] \tag{3.6}$$

The term $\Delta\mathbf{z}_l = \mathbf{z}_l - \mathbf{h}\left(t_l,\, \mathbf{x}_B\left(t_l,\, \mathbf{u}^*\right)\right) \in \mathbb{R}^I$ represents the difference between the true measurements and those reconstructed from the reference trajectory $\mathbf{x}_B^*(t_l) = \mathbf{x}_B\left(t_l,\, \mathbf{u}^*\right)$. The term $G_l \in \mathbb{R}^{I\times 3}$ is instead the **Jacobian**, which represents the partial derivatives of the measurements at a given observation time t_l with respect to the estimated parameters.

The minimum of J can be found by assuming G_l to have full rank and setting its partial derivative with respect to $\Delta\mathbf{u}$ equal to zero:

$$\frac{\partial J}{\partial \Delta\mathbf{u}} = \sum_l \frac{\partial \left\{ [\Delta\mathbf{z}_l - G_l \cdot \Delta\mathbf{u}]^T \cdot W \left[\Delta\mathbf{z}_l - G_l \cdot \Delta\mathbf{u}\right] \right\}}{\partial \Delta\mathbf{u}} = 0 \tag{3.7}$$

Identifying $\mathbf{a} \equiv [\Delta\mathbf{z}_l - G_l \cdot \Delta\mathbf{u}]$, $\mathbf{b} = W \cdot \mathbf{a}$, $\mathbf{c} \equiv \Delta\mathbf{u}$ and using the relation [7]:

$$\frac{\partial \mathbf{a}^T\mathbf{b}}{\partial \mathbf{c}} = \mathbf{a}^T \cdot \frac{\partial \mathbf{b}}{\partial \mathbf{c}} + \mathbf{b}^T \cdot \frac{\partial \mathbf{a}}{\partial \mathbf{c}} \tag{3.8}$$

Equation (3.7) can be rewritten as:

$$\sum_l \{ [\Delta\mathbf{z}_l - G_l \cdot \Delta\mathbf{u}]^T W(-G_l) + [\Delta\mathbf{z}_l - G_l \cdot \Delta\mathbf{u}]^T W^T(-G_l) \} = 0 \tag{3.9}$$

Introducing the sums $\Delta\mathbf{z} = \sum_l \Delta\mathbf{z}_l$ and $G = \sum_l G_l$, the minimisation problem can be finally expressed through the following **normal equations**:

$$(G^T W G)\, \Delta\mathbf{u} = (G^T W)\, \Delta\mathbf{z} \tag{3.10}$$

This linear system is solved for the unknown $\Delta\mathbf{u}$, from which $\mathbf{u} = \mathbf{u}^* + \Delta\mathbf{u}$ can be retrieved. As the model $\mathbf{h}$ is non-linear, the simplified loss function (Equation (3.6)) differs from the true one and the value of $\hat{\mathbf{u}}$ is not the exact solution of the estimation problem. However, this can be improved by iterating the solution of the equations and updating the reference at step n $\mathbf{u}_n^*$ with the estimation $\hat{\mathbf{u}}_{n-1}$ of the previous step, until convergence is reached. Having no a-priori information on the manoeuvre, the initial value of the iterative process is set to $\mathbf{u}^* = \mathbf{0}$. It is important to remark that to avoid a non-unique determination of $\mathbf{u}$, it shall be always verified that the number of measurements is at least equal to the number of unknowns (equal to 3, which are the components of $\mathbf{u}$).

Equation (3.10) is almost equivalent to the solution of a batch least-squares orbit determination process, with the main difference being in the matrix G. In fact, the leading matrix of the normal equations for classic orbit determination (for estimation of position and velocity) is just the derivative of the reconstructed measurements with respect to a reference state vector [7]. The matrix G can be decomposed as following:

$$G = \sum_l \frac{\partial \mathbf{h}\left(t_l,\, \mathbf{x}_B\left(t_l,\, \mathbf{u}^*\right)\right)}{\partial \mathbf{u}} = \sum_l \frac{\partial \mathbf{h}\left(t_l,\, \mathbf{x}_B\left(t_l,\, \mathbf{u}^*\right)\right)}{\partial \mathbf{x}_B\left(t_l,\, \mathbf{u}\right)} \cdot \frac{\partial \mathbf{x}_B\left(t_l,\, \mathbf{u}^*\right)}{\partial \mathbf{u}} = \sum_l H_l \cdot \frac{\partial \mathbf{x}_B\left(t_l,\, \mathbf{u}^*\right)}{\partial \mathbf{u}} \tag{3.11}$$

$H_l \in \mathbb{R}^{I\times 6}$ represents the partial derivatives of the measurements with respect to the state vector (which were derived in Appendix A.2). The term $\partial \mathbf{x}_B\left(t_l,\, \mathbf{u}^*\right)/\partial \mathbf{u} \in \mathbb{R}^{6\times 3}$ is instead known as **transition-sensitivity** product[1] and depends on the dynamical model used for the propagation of the state.

3.2.2. Selection of first manoeuvre estimate for subsequent re-estimation

To carry out the manoeuvre estimation, the least-squares problem must be solved for a set of t_M values comprised in an interval T (from the last track used to estimate the pre-manoeuvre orbit to the first post-manoeuvre track being considered). Therefore, the output of the proposed manoeuvre estimation algorithm is a pool of solutions for every $t_M \in T$, each one associated to a WRMS and to an estimated manoeuvre $\hat{\mathbf{u}}$. In order to compute a preliminary post-manoeuvre orbit, there is the need to select a proper manoeuvre estimate, this is, a combination of t_M and $\mathbf{u}$. A simple strategy is proposed:

1. at first, the global minimum in terms of WRMS (Equation (3.3)) is detected and then just the solutions with a value of $\sqrt{J}$ **lower than the 115%** of the minimum are retained.
2. among this set, the solution associated to the **lowest control effort** $\|\hat{\mathbf{u}}\|$ (with $\|(\cdot)\|$ representing the Euclidean norm of a vector) is eventually selected.

$\sqrt{J}$ is selected as the leading metric for the short-listing as it quantifies the quality of the estimation. The rationale behind the second step in the selection strategy is that manoeuvres performed by satellites are normally designed to be optimal in terms of fuel consumption. The percentage value for taking the solutions with minimum WRMS is configurable and could be eventually modified. The current 15% has proven to be a reasonable value in the tests performed so far, as it allows to locate all the local minima regions having similar values and to account for the errors introduced by the discretization of T. In general, this selection strategy proves to be robust in selecting satisfactory estimates. The selection criterion is slightly different from the previous one [35], where

[1] This definition is generally given to any partial derivatives of the state with respect to parameters to be estimated.

the best solution was taken as the one with lowest $\|\hat{\mathbf{u}}\|$ but just among the local WRMS minima, without considering any margin for enlarging the pool. Nonetheless, the new proposed strategy can be applied also to GEO manoeuvre estimation, as it is able to is able to retrieve the same estimates as the previous one.

It is important to remark that this selection strategy is intended to be as simple as possible at deriving a reliable first estimate and is tailored to a single-satellite scenario. Further developments, aimed at extending the correlation problems to multiple RSOs, shall be posed in a multi-target association framework. In this regard, a possible approach would be to consider the solutions associated to the $\sqrt{J}$ minima as hypotheses and creating a tree of track-to-orbit associations. These will be evaluated, pruned and eventually promoted through the analysis of more post-manoeuvre tracks to finally associate each set of post-manoeuvre tracks to the correct manoeuvrable RSO.

Once that the a-priori estimates for the manoeuvre time and components have been found as described above, it is possible to perform a high-fidelity orbit determination process, with a numerical propagator, which determines the post-manoeuvre orbit and refines the initial guesses. The steps of the manoeuvre estimation algorithm are summarised in Algorithm 1.

Algorithm 1 Manoeuvre estimation

1: **Requiring**: pre-manoeuvre orbit $\mathbf{y}_A(t)$ and observations $\{\mathbf{z}_l\}$.
2: **for** $t_M \in T$ **do**
3: Set the initial solution $\mathbf{u}^* = \mathbf{0}$.
4: Solve Equation (3.10) iteratively.
5: **end for**
6: Locate solution with minimum WRMS $\sqrt{J}_{min}$.
7: Retain solutions with $\sqrt{J} \leqslant 1.15 \cdot \sqrt{J}_{min}$.
8: Among the pool of solutions, select the one with minimum $\|\hat{\mathbf{u}}\|$.
9: Perform orbit determination including the manoeuvre estimate as parameter.

3.2.3. Development of dynamical model for manoeuvre estimation

Having set the physical and mathematical framework, the last step required to complete the manoeuvre estimation algorithm is to define a dynamical model for $\mathbf{x}_B(t, \mathbf{u})$, required for the computation of the predicted measurements $\mathbf{h}(t, \mathbf{x}_B)$ and of the matrix G as a function of time and of manoeuvre size $\mathbf{u}$ (at a given manoeuvre time t_M). The require-

ment of computing multiple solutions for a set of t_M values before the final selection imposes a requirement to have a computationally efficient propagation algorithm; the use of a typical numerical propagator would entail a very large computational cost, which is something to be avoided considering the requirement of real time operation of the algorithm. For this reason, a simple, fast and yet sufficiently accurate dynamical model partially based on linear dynamics is developed. The model is an improvement of the fully-linear one employed in manoeuvre estimation of GEO objects [35]. Manoeuvres are expected to be small and thus causing a reasonably modest change in the orbit (with ΔVs in the order of $10^{-2} \div 10^{-6}$ of the velocity), allowing the use of linearisation techniques.

Consider the pre-manoeuvre orbit under analysis (identified with the subscript A), as presented in Section 3.1. Along with the trajectory of the extended state vector, a product of the orbit determination process and propagation is the full transition matrix $\Psi(t, t_0)$, estimated with respect to a reference time t_0. This matrix represents the linear mapping between the initial extended state vector $\mathbf{y}_A(t_0)$ and the state vector at any time t:

$$\Psi(t, t_0) = \frac{\partial \mathbf{y}_A(t)}{\partial \mathbf{y}_A(t_0)} \in \mathbb{R}^{(6+n_p)\times(6+n_p)} \tag{3.12}$$

The matrix $\Psi(t, t_0)$ can be conveniently divided into four submatrices [7]:

$$\Psi(t,\, t_0) = \begin{bmatrix} \Phi(t,\, t_0) & S(t) \\ \mathbf{0} & \mathbb{I}_{n_p} \end{bmatrix} \tag{3.13}$$

with $\Phi(t,\, t_0) \in \mathbb{R}^{6\times 6}$ and $S(t) \in \mathbb{R}^{6\times n_p}$. $\mathbb{I}_{n_p}$ is the identity matrix of dimension $n_p \times n_p$. The first submatrix represents the linear mapping of the position and velocity vectors at a time t with respect to the initial state, also known as **state transition matrix (STM)**:

$$\Phi(t,\, t_0) = \frac{\partial\, \mathbf{x}_A(t)}{\partial \mathbf{x}_A(t_0)} \tag{3.14}$$

The second term instead, named as sensitivity matrix, is the partial derivative of the state vector with respect to the dynamical parameters: $S(t) = \partial \mathbf{x}_A(t)/\partial \mathbf{p}$.

Consider now the post-manoeuvre trajectory $\mathbf{x}_B(t)$, whose time evolution can be computed through the following differential equation:

$$\frac{\mathrm{d}\mathbf{x}_B}{\mathrm{d}t} = \mathbf{f}(t,\, \mathbf{x}_B);\ \text{with:}\ \mathbf{x}_B(t_0) = \bar{\mathbf{x}}_B \tag{3.15}$$

Only the state vector components of the post-manoeuvre orbit are considered in the model, assuming that the dynamical parameters (which would be included in a complete state vector $\mathbf{y}_B(t)$) are the same of the pre-manoeuvre trajectory. Considering a deterministic model, the right-hand side term includes the accelerations which impact the motion. These contributions might be split as follows:

$$\mathbf{f}(t,\,\mathbf{x}_B) = \mathbf{f}_K(t,\,\mathbf{x}_B) + \sum_i \mathbf{f}_i(t,\,\mathbf{x}_B);\ \text{with: } \|\mathbf{f}_K(t,\,\mathbf{x}_B)\| \gg \|\mathbf{f}_i(t,\,\mathbf{x}_B)\| \tag{3.16}$$

with $\mathbf{f}_K(t,\,\mathbf{x}_B)$ representing the Keplerian motion of the body (two-body motion), while the term $\mathbf{f}_P(t,\,\mathbf{x}_B) = \sum_i \mathbf{f}_i(t,\,\mathbf{x}_B)$ accounts for the perturbing accelerations.

Let's derive the Taylor expansion of $\mathbf{x}_B(t)$ with respect to the a reference trajectory $\mathbf{x}_{B,ref}$:

$$\mathbf{x}_B(t) = \mathbf{x}_{B,ref}(t) + \frac{\partial \mathbf{x}_{B,ref}}{\partial \mathbf{x}^0_{B,ref}}(t)\cdot\Delta\mathbf{x}_{B,0} + \frac{1}{2}\Delta\mathbf{x}^T_{B,0}\cdot\frac{\partial^2\mathbf{x}_{B,ref}}{\partial(\mathbf{x}^0_{B,ref})^2}\cdot\Delta\mathbf{x}_{B,0} + \dots \tag{3.17}$$

where $\mathbf{x}^0_B$ is the initial state of the satellite and $\Delta\mathbf{x}_{B,0}$ is the deviation with respect to the reference $\mathbf{x}^0_{B,ref}$. Retaining only the zero and first-order terms, the series becomes:

$$\mathbf{x}_B(t) \approx \mathbf{x}_{B,ref}(t) + \frac{\partial \mathbf{x}_{B,ref}}{\partial \mathbf{x}^0_{B,ref}}(t)\cdot\Delta\mathbf{x}_{B,0} = \mathbf{x}_{B,ref}(t) + \Delta\mathbf{x}_B(t) \tag{3.18}$$

with:

$$\Delta\mathbf{x}_B(t) = \frac{\partial \mathbf{x}_{B,ref}}{\partial \mathbf{x}^0_{B,ref}}(t)\cdot\Delta\mathbf{x}_{B,0} \tag{3.19}$$

Let's consider the initial state of the propagation at $t = t_M$, which is the manoeuvre epoch. Therefore, the free time variable t shall be intended as $t \geqslant t_M$. Taking $\mathbf{x}_{B,ref}(t) = \mathbf{x}_A(t)$ as the reference trajectory, the post-manoeuvre state can be simply obtained by computing the deviation $\Delta\mathbf{x}_B(t)$. Consequently, the latter will depend on the derivative $\partial\mathbf{x}_A/\partial\mathbf{x}^0_A$ (which is the STM of orbit A referred to t_M, namely $\Phi(t,\,t_M)$) and on the difference between the initial states, which is a function of the manoeuvre $\mathbf{u}$. The deviation $\Delta\mathbf{x}_B(t)$ can be split in different components, each one representing one contribution to the motion of the satellite, as shown in Equation (3.16). The expression for the post-manoeuvre trajectory is reformulated as:

$$\begin{aligned}\mathbf{x}_B\left(t,\, t_M,\, \mathbf{u}\right) &= \mathbf{x}_A\left(t\right) + \Delta\mathbf{x}_B\left(t\right) \\ &= \mathbf{x}_A\left(t\right) + \Delta\mathbf{x}_K(t,\, t_M,\, \mathbf{u}) + \Delta\mathbf{x}_P\left(t,\, t_M,\, \mathbf{u}\right)\end{aligned} \tag{3.20}$$

with:

$$\Delta\mathbf{x}_K(t,\, t_M,\, \mathbf{u}) + \Delta\mathbf{x}_P\left(t,\, t_M,\, \mathbf{u}\right) = \Phi\left(t,\, t_M\right) \cdot \left(\mathbf{x}_B^0 - \mathbf{x}_A^0\right) \tag{3.21}$$

The first deviation term, $\Delta\mathbf{x}_K\left(t,\, t_M,\, \mathbf{u}\right)$, accounts for the Keplerian motion. The second one, $\Delta\mathbf{x}_P\left(t,\, t_M,\, \mathbf{u}\right)$, is instead representative of all the effects of the perturbations on the motion. As the trajectory shall be propagated from the manoeuvre epoch on, the initial states $\mathbf{x}_A^0$ and $\mathbf{x}_B^0$ are simply connected through the impulsive manoeuvre $\mathbf{u}$:

$$\mathbf{x}_A^0 = \mathbf{x}_A\left(t = t_M\right) \tag{3.22}$$

$$\mathbf{x}_B^0 = \mathbf{x}_B\left(t = t_M,\, \mathbf{u}\right) = \mathbf{x}_A^0 + \left[\mathbf{0},\, \mathbf{u}\right]^T \tag{3.23}$$

These two states are indeed acting as boundary values for the manoeuvre estimation problem. The expression of the deviations can be found by making the two contributions to the motion explicit, as done in Equation (3.16). The subscripts $(\cdot)_{\mathbf{xv}}$ represents the submatrices of the partial derivatives with respect to just the velocity components, as the difference in the two initial states does not have any position component.

$$\begin{aligned}\Delta\mathbf{x}_B = \Phi_{\mathbf{xv}}\left(t,\, t_M\right) \cdot \mathbf{u} &= \left(\frac{\partial\mathbf{x}_A\left(t\right)}{\partial\mathbf{x}_A^0}\right)_{\mathbf{xv}} \cdot \mathbf{u} \\ &= \left(\frac{\partial\mathbf{x}_{A,K}\left(t\right)}{\partial\mathbf{x}_A^0} + \frac{\partial\mathbf{x}_{A,P}\left(t\right)}{\partial\mathbf{x}_A^0}\right)_{\mathbf{xv}} \cdot \mathbf{u} \\ &= \left[\Phi_{K,\mathbf{xv}}\left(t,\, t_M\right) + \Phi_{P,\mathbf{xv}}\left(t,\, t_M\right)\right] \cdot \mathbf{u}\end{aligned} \tag{3.24}$$

The two matrices Φ_K and Φ_P represent the state transitions of orbit A associated to the two contributions to the motion. To improve the accuracy of the model, the first term, related to the Keplerian motion, can be transformed and included in its full non-linearity. In fact, it is noticeable that $\Phi_{K,\mathbf{xv}}\left(t,\, t_M\right) \cdot \mathbf{u}$ is the first-order term of the Taylor expansion of the difference between two Keplerian trajectories propagated starting from the initial states in Equation (3.22) and Equation (3.23):

$$\begin{aligned}\mathbf{x}_{B,K}(t) - \mathbf{x}_{A,K}(t) &= \mathbf{f}_K(t,\, \mathbf{x}_{B,K}) - \mathbf{f}_K(t,\, \mathbf{x}_{A,K}) \\ &= \left(\frac{\partial \mathbf{x}_{A,K}(t)}{\partial \mathbf{x}_A^0}\right)_{\mathbf{xv}} \cdot \mathbf{u} + \frac{1}{2!}\,\mathbf{u}^T \cdot \left(\frac{\partial^2 \mathbf{x}_{A,K}(t)}{\partial (\mathbf{x}_A^0)^2}\right)_{\mathbf{xv}} \cdot \mathbf{u} + ... \\ &\approx \Phi_{K,\mathbf{xv}}(t,\, t_M) \cdot \mathbf{u}\end{aligned} \tag{3.25}$$

The subscript $(\cdot)_{\mathbf{xv}}$, in the case of the third order tensor, represents the subtensor associated to the derivatives with respect to the velocity components. Finally, the deviation associated to the Keplerian motion can be included in the dynamical model in the form:

$$\Delta\mathbf{x}_K(t,\, t_M,\, \mathbf{u}) = \mathbf{x}_{B,K}(t,\, t_M, \mathbf{u}) - \mathbf{x}_{A,K}(t,\, t_M) \tag{3.26}$$

Each Keplerian trajectory can be found from $\mathbf{f}_K(t,\, \mathbf{x})$, built up from the analytical expressions of the two-body problem, considering the initial conditions in Equation (3.22) and Equation (3.23). Knowing the orbital elements and solving Kepler's equation numerically, it is possible to compute the true anomaly as a function of time for each propagation step. Then, the state vector can be retrieved with the typical conversion routine that transforms the Keplerian elements into a Cartesian state vector.

To complete the dynamical model, it is necessary to compute $\Phi_P(t,\, t_M)$, representative of all the other contributions to the motion except for the central gravity. Its value is not directly available nor easily calculable via analytical expressions. However, as the STM $\Phi(t,\, t_0)$ of the orbit A is available as an input, the time evolution of Φ_P can be simply computed by subtracting $\Phi_K(t,\, t_M)$, which in turn can be derived from $\mathbf{x}_{A,K}$. Its expression, already presented in Equation (3.24), is:

$$\Phi_K(t,\, t_M) = \frac{\partial\, \mathbf{x}_{A,K}(t)}{\partial\, \mathbf{x}_A^0} \tag{3.27}$$

Having the function $\mathbf{x}_{A,K} = \mathbf{f}(t,\, \mathbf{x}_{A,K})$, the STM can be built up at each time step. In this case, it was chosen to employ a numerical scheme (2^{nd} order central differences) to compute the partial derivatives with respect to the initial state $\mathbf{x}_A^0$. The same matrix could also be derived from the analytical expressions of the state transition of Keplerian elements, and subsequently applying conversion routines to retrieve the Cartesian coordinates [7]. Recalling that the full STM $\Phi(t,\, t_0)$ shall be transformed in order to be referred to the manoeuvring time t_M, the expression for $\Phi_P(t,\, t_M)$ is:

$$\Phi_P(t, t_M) = \Phi(t, t_M) - \Phi_K(t, t_M) \tag{3.28}$$
$$= [\Phi(t, t_0) \cdot \Phi(t_0, t_M)] - \Phi_K(t, t_M) \tag{3.29}$$
$$= \left[\Phi(t, t_0) \cdot \Phi(t_M, t_0)^{-1}\right] - \Phi_K(t, t_M) \tag{3.30}$$

Finally, all the terms shall be assembled together for final expression of $\mathbf{x}_B(t, t_M, \mathbf{u})$:

$$\begin{aligned}\mathbf{x}_B(t, t_M, \mathbf{u}) = \mathbf{x}_A(t) &+ \\ &+ [\mathbf{x}_{B,K}(t, t_M, \mathbf{u}) - \mathbf{x}_{A,K}(t, t_M)] + \\ &+ \left\{\left[\Phi(t, t_0) \cdot \Phi(t_M, t_0)^{-1}\right] - \Phi_K(t, t_M)\right\}_{\mathbf{xv}} \cdot \mathbf{u}\end{aligned} \tag{3.31}$$

In the former work by Pastor [35], the dynamical model for describing the post-manoeuvre trajectory considered both the Keplerian motion and the perturbations under linear dynamics:

$$\mathbf{x}'_B(t, t_M, \mathbf{u}) = \mathbf{x}_A(t) + \Phi(t, t_M)_{\mathbf{xv}} \cdot \mathbf{u} \tag{3.32}$$

The expression for $\mathbf{x}_B(t, t_M, \mathbf{u})$ could be rewritten as a function of $\mathbf{x}'_B(t, t_M, \mathbf{u})$:

$$\begin{aligned}\mathbf{x}_B(t, t_M, \mathbf{u}) = \mathbf{x}'_B(t, t_M, \mathbf{u}) &+ \\ &+ [\mathbf{x}_{B,K}(t, t_M, \mathbf{u}) - \mathbf{x}_{A,K}(t, t_M)] - \Phi_K(t, t_M)_{\mathbf{xv}} \cdot \mathbf{u}\end{aligned} \tag{3.33}$$

Having derived the equation of the dynamical model, it is required to define an expression for $\partial \mathbf{x}_B(t, \mathbf{u}) / \partial \mathbf{u}$ (for a fixed t_M) to build up the contributions to the normal equations matrix (Equation (3.11)). Differentiating Equation (3.31) with respect to $\mathbf{u}$:

$$\frac{\partial \mathbf{x}_B(t, \mathbf{u})}{\partial \mathbf{u}} = \frac{\partial \mathbf{x}_{B,K}(t, \mathbf{u})}{\partial \mathbf{u}} + [\Phi(t, t_M) - \Phi_K(t, t_M)]_{\mathbf{xv}} \tag{3.34}$$

The first term on the right-hand side is the state transition matrix of the Keplerian trajectory $\mathbf{x}_{B,K}(t, \mathbf{u})$, since a variation of $\mathbf{u}$ directly implies a variation on the initial state $\mathbf{x}_B^0 = \mathbf{x}_B(t = t_M, \mathbf{u}) = \mathbf{x}_A^0 + [\mathbf{0}, \mathbf{u}]^T$. The derivatives of $\mathbf{x}_A(t)$ and $\mathbf{x}_{A,K}(t)$ with respect to the velocity increment are null since they do not depend on it.

The reason behind the development of this enhanced version of the linear model, which will also be referred to as **Keplerian + linear perturbations model** (Equation (3.31)), is the foreseen application in LEO, where dynamics are faster and subject to higher non-linearities if compared to the GEO environment. In fact, with the simple linear model

(Equation (3.32)), larger errors are expected for high-magnitude burns and for longer propagation times; this is particularly true for in-track burns, whose major effect is to change the semi-major axis of the orbit (and therefore the orbital period). With respect to the linear one, the Keplerian + linear perturbations model requires the propagation of two Keplerian orbits and the computation of two state transition matrices at each integration step. However, via an efficient implementation of these two operations, the computational cost can be kept low so not to impact the run-time performances of the manoeuvre estimation algorithm. It is worth to mention that this cost could be reduced by the employment of the analytical method for the computation of the Keplerian STMs.

4 | Results

The following chapter presents a variety of results obtained by the tests and the application of the manoeuvre detection and estimation methodology. Section 4.1 shows some test cases, performed with different manoeuvres, to understand the level of accuracy of the dynamical model for the manoeuvre estimation algorithm and to compare it to its previous version. Section 4.2 introduces the simulation scenario used for the application of the manoeuvre detection and estimation methodology, highlighting the most important steps of the workflow. Section 4.3 briefly describes the results of the application of the manoeuvre detection step, reporting its performances and underlining its limitations. Finally Section 4.4 and its subsections describe the results of the developed manoeuvre estimation algorithm to obtain first guesses, as well as the advantages obtained by performing re-estimation with the high-fidelity orbit determination process.

4.1. Results of the accuracy tests for the dynamical models

The dynamical model presented in Section 3.2.3 is tested to define its performances. It is compared against a high-fidelity numerical propagator, to determine the level of error reached in the propagation, and against the linear propagator previously employed for manoeuvre detection of GEO objects ($\mathbf{x}'_B(t, \mathbf{u})$, Equation (3.32)), to assess the benefits of using this newly developed model. The subject of the tests is a LEO object, whose characteristics are reported in Table 4.1. The state vector is expressed in GCRF.

The orbit of the satellite is propagated for a total of 5 days, considering a manoeuvre to happen at t_M after 1 day of simulation. The epochs are reported in Table 4.2. Considering an average orbital period, the post-manoeuvre time span (equal to 4 days) approximately corresponds to 58 satellite revolutions. Four days are, in general, sufficient to receive four radar tracks of a LEO object, so the propagation errors that are obtained with these simulations are expected to be similar to the ones in the application of the manoeuvre estimation algorithm presented in Section 3.2.

Epoch	September 5^{th}, 2018, 00:00
Position vector r	$[3528.52, -4599.69, 4232.54]^T\ km$
Velocity vector v	$[-3.72, 2.59, 5.91]^T\ km/s$
Mass	$1000\,kg$
Reference area	$10\,m^2$
Reference drag coeff.	3.334
Reference SRP coeff.	0.967

Table 4.1: Characteristics of satellite for propagation accuracy test.

Initial propagation epoch	September 5^{th}, 2018, 00:00
Manoeuvre epoch t_M	September 6^{th}, 2018, 00:00
Final propagation epoch	September 10^{th}, 2018, 00:00

Table 4.2: Propagation times for the LEO object.

To start, a high-fidelity propagation is performed. The force contributions included in the dynamical model are reported in Table 4.3.

Gravity field	30×30
Atmospheric drag	MSISE90 model
Moon gravity	Third body perturbation + $J2$ gravity interaction
Third body perturbations	Sun and other planets
Planetary tides	Solid tides only
Solar radiation pressure	Cannonball model

Table 4.3: Force models of the high-fidelity propagator.

The propagation generates the trajectory of $\mathbf{x}_A(t)$, required for both the linear and the Keplerian + linear perturbations models. A total of 9 simulations is performed considering different impulsive manoeuvres Radial – In-track – Cross-track (RIC) frame: two radial burns, two in-track burn and two cross-track burns. Considering a position vector $\mathbf{r}$ and a velocity vector $\mathbf{v}$, the RIC frame is a local frame defined by the unit vectors:

$$\begin{aligned} \hat{\mathbf{r}} &= \frac{\mathbf{r}}{\|\mathbf{r}\|} \\ \hat{\mathbf{i}} &= \hat{\mathbf{c}} \times \hat{\mathbf{r}} \\ \hat{\mathbf{c}} &= \frac{\mathbf{r} \times \mathbf{v}}{\|\mathbf{r} \times \mathbf{v}\|} \end{aligned} \tag{4.1}$$

For each manoeuvre direction, tests are made with a burn with magnitude equal to 0.01 m/s, 0.1 m/s and 1.0 m/s. These orders of magnitude are selected as they are representative of the majority of the manoeuvres which are analysed in the following sections. Along with the propagation of the two linearised dynamical models, a trajectory $\mathbf{x}_B^{num}(t)$, considering the impulsive manoeuvres, is computed using the high-fidelity dynamical model.

The results of the tests are presented in plots which represent the Root Mean Square Error (RMSE), divided in position and velocity components, of the difference between the high-fidelity and the approximated trajectories, namely the RMSE of $\mathbf{x}_B^{num} - \mathbf{x}_B$ and of $\mathbf{x}_B^{num} - \mathbf{x}'_B$. The difference in the position components is defined as $\Delta\mathbf{r}$, while the one for the velocity components is $\Delta\mathbf{v}$. The errors are averaged in rolling mean over time windows approximately equal to an orbital revolution of the satellite (computed at t_M after the manoeuvre), in order to filter out oscillations with the same period. In each of the plots, the vertical dashed line represents the manoeuvre epoch.

The plots in Figure 4.1 present the results for the radial burns. For the 0.01 m/s and 0.1 m/s impulses, both models perform well in terms of accuracy. The errors stay beneath the mm/s level in velocity, while for the position components they are below the order of m. For the 1.0 m/s burn, errors rise up to tenth of meters in position and cm/s in velocity. The Keplerian + linear perturbations model proves to be more accurate than the linear one in all three cases.

Results for the in-track burn simulations are shown in Figure 4.2. The divergence reached by the two propagators is higher in this case, since, as already mentioned, in-track burns have a greater secular effect on dynamics (due to their impact on the semi-major axis). For the 0.01 m/s burn, the errors arrive to approximately 7 m and 8 mm/s for the linear model, while ≈ 4 m and ≈ 4 mm/s for the other one. With manoeuvre magnitude equal to 0.1 m/s, errors reach the order of hundreds of meters in position and dm/s in velocity. With the last test case, the divergence rises up to kilometres in position and m/s in velocity. In all three cases, the propagation with the Keplerian + linear perturbations model is more accurate than the linear one; moreover, it is noticeable that the linear model starts diverging approximately one day before the other one.

The last results, for the cross-track burns, are represented in Figure 4.3. Again, as in the radial case, both models perform well for lower magnitude burns. However, surprisingly, the linear model outperforms the Keplerian + linear perturbations one. For the 0.01 m/s manoeuvre, the errors arrive to ≈ 1 mm and ≈ 6 mm in position, while to approximately 0.001 mm/s and 0.006 mm/s in velocity. The difference between the two propagators becomes more evident with the 0.1 m/s and 1.0 m/s cases, where the errors reach the order of metres in position and cm/s in velocity. The greatest accuracy of the linear model with respect to the Keplerian + linear perturbations one was not expected from theory, so the topic shall be investigated further. This phenomenon, which does not show up for the other test cases, might be related to the physics of the manoeuvre, which imply a change of plane (that is, a change in inclination and right ascension of the ascending node).

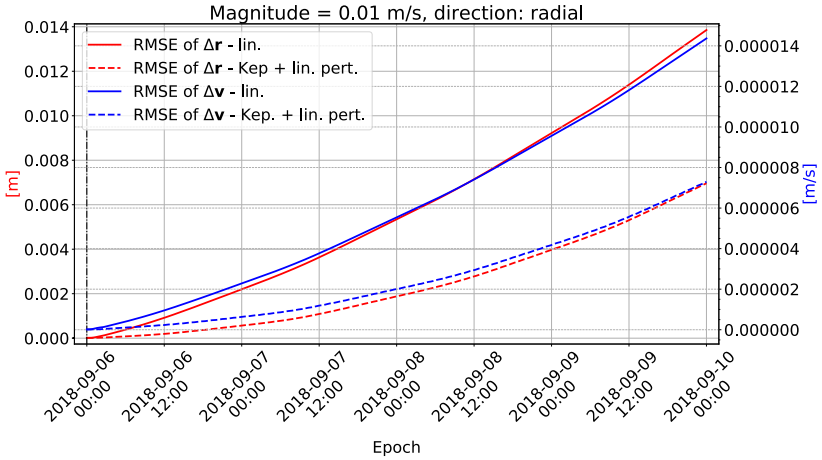

(a) 0.01 m/s

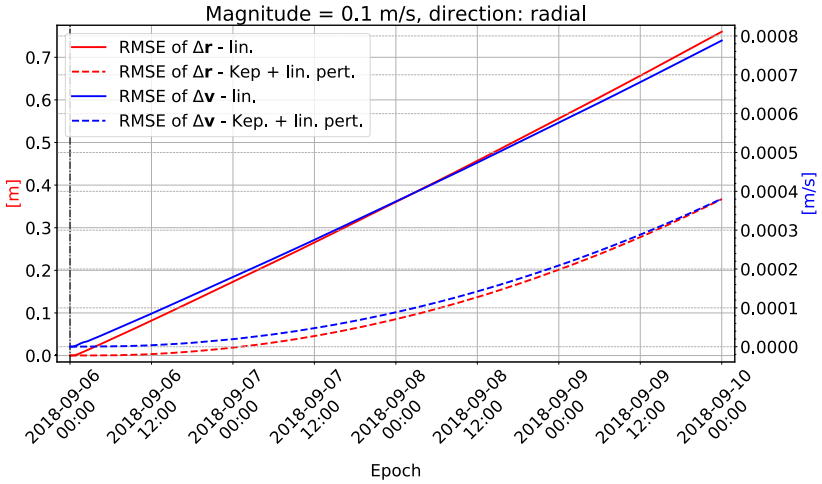

(b) 0.1 m/s

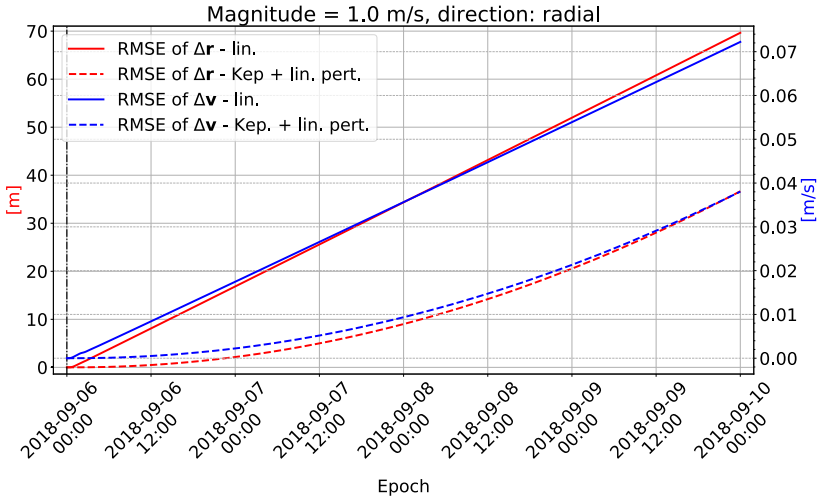

(c) 1.0 m/s

Figure 4.1: Test for propagation accuracy of the two dynamical models (*radial burns*).

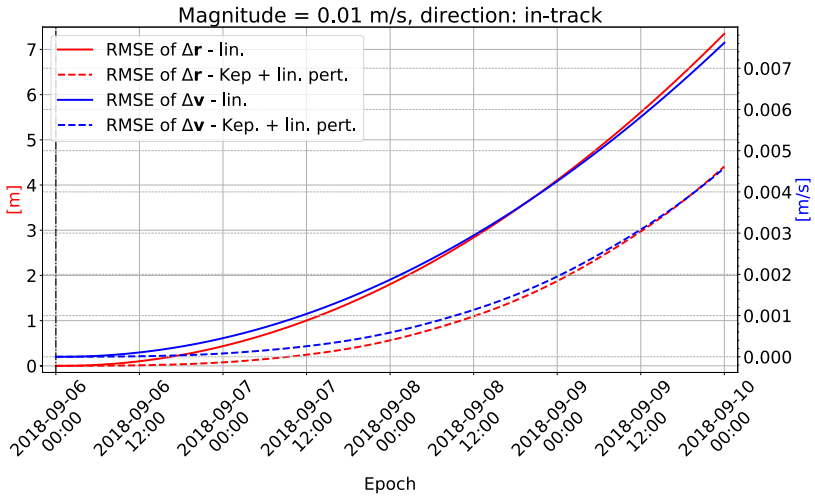

(a) 0.01 m/s

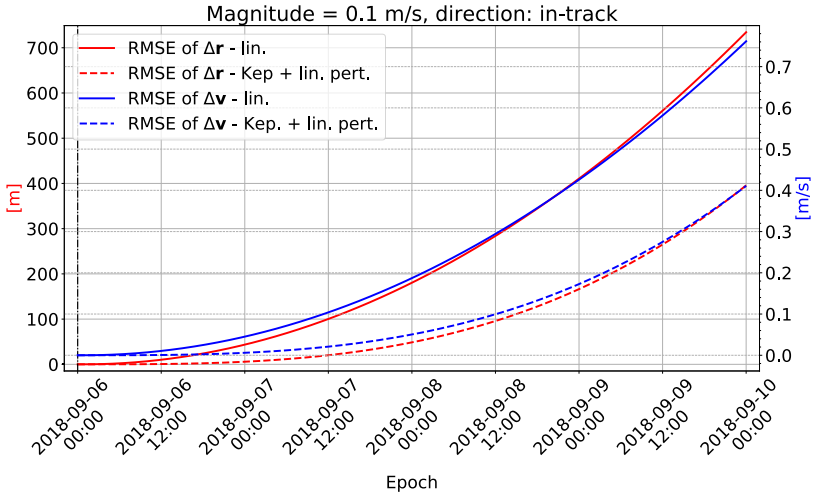

(b) 0.1 m/s

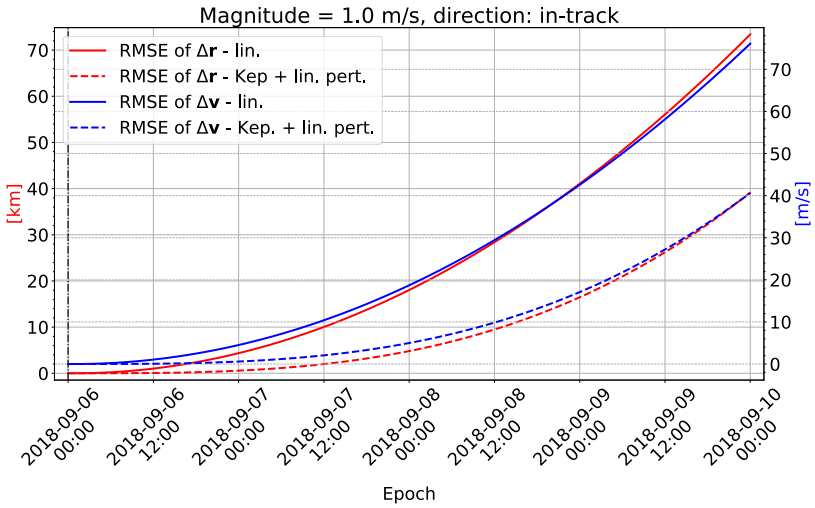

(c) 1.0 m/s

Figure 4.2: Test for propagation accuracy of the two dynamical models (*in-track burns*).

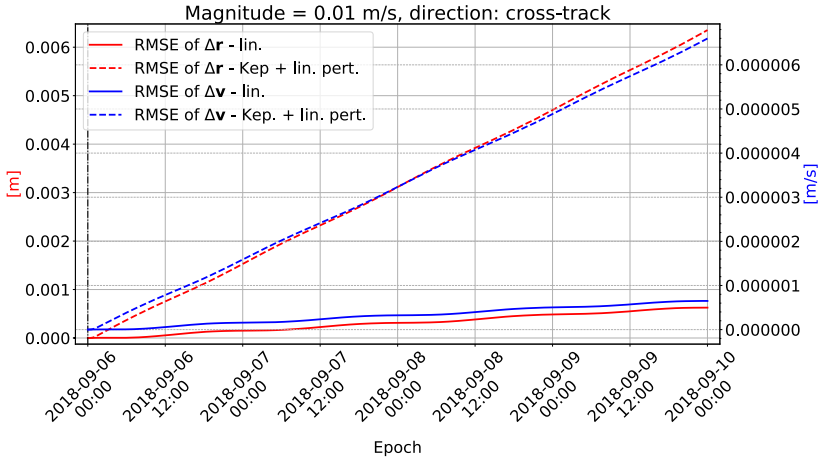

(a) 0.01 m/s

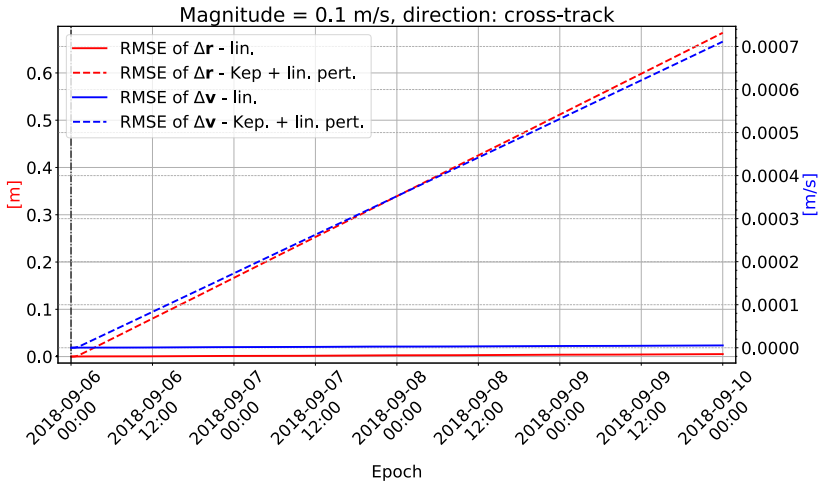

(b) 0.1 m/s

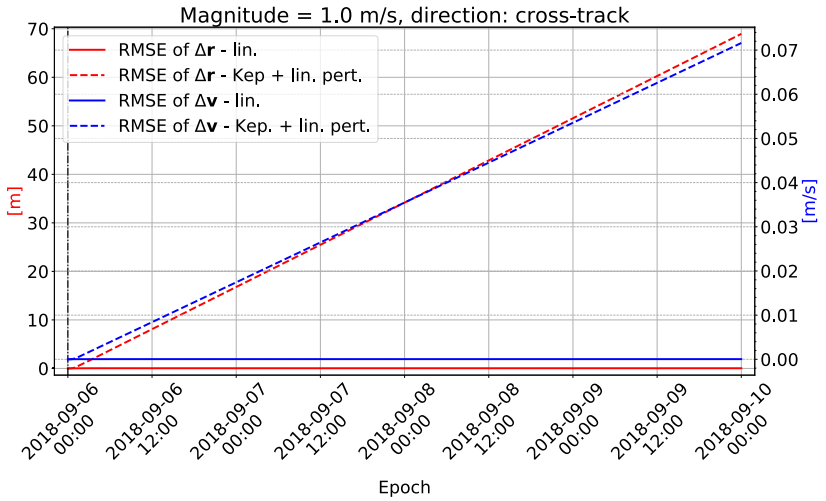

(c) 1.0 m/s

Figure 4.3: Test for propagation accuracy of the two dynamical models (*cross-track burns*).

4.2. Setup of simulation scenario

The combined manoeuvre detection and estimation algorithm is tested by setting up a simulation scenario resembling a cataloguing maintenance chain. The subject of the tests is **Sentinel 3-A**, which is on a low-eccentricity polar orbit, with a nominal altitude of 814 km and inclination of 98.65°. The time window considered for the simulation starts in 2017 and ends in 2019, for a total of three full years. The satellite performs a total of 22 manoeuvres, with burn magnitude varying from a few mm/s to m/s. Manoeuvres are either impulsive, with duration in the order of a few seconds, or long, with duration between 12 and 15 minutes. Both the initial orbit and manoeuvre history (reported in Appendix B) are publicly available [94] [95]. With such manoeuvre history, an orbit is propagated for the three years. The simulation considers one radar located in mainland Spain, having a pyramidal field of view with $43.2° \times 30°$ in semi-aperture, and whose noise parameters are reported in Table 4.4. The ground station does not have any measurement bias and is considered to be always operating and pointing towards the same direction.

Noise σ for 2-way range	**Noise σ for 2-way range rate**	**Noise σ for azimuth and elevation**
10 m	1000 mm/s	300 $mdeg$

Table 4.4: Noise sigmas of the simulated radar.

The tracks are generated considering the propagated orbit and the equations reported in Appendix A.2. Each track contains observations, separated by 5 seconds each, of the two-way range, two-way range rate, azimuth and elevation. The first two measurements are simply obtained by adding a factor 2 to the Equations (A.8) to (A.10) and considering no flight-time corrections. The duration of the simulated tracks is 2 minutes on average, which is determined by the satellite orbit, the location of the ground station and the field of view of the radar. The noise is added to each observation in the tracks as:

$$\mathbf{z}_k = \mathbf{h}\left(t_k,\, \mathbf{x}(t_k)\right) + \boldsymbol{\epsilon} \tag{4.2}$$

where $\boldsymbol{\epsilon}$ is a random vector of samples for Gaussian distributions with zero mean and standard deviation equal to the σ values reported in Table 4.4.

The simulation is run by considering observation windows composed of 18 successive tracks each (yielding a time span equal or greater than 9 days, with a typical revisit frequency of 12 hours as the satellite is on a polar orbit). Consecutive windows are shifted by just

1 track, in order to be able to analyse the effect of single tracks. The workflow is the following:

1. The 18 tracks in the observation window are **compared to a reference orbit** (in terms of WRMS). Such orbit is computed with tracks belonging to the window of four simulation steps before, to **avoid contamination** of any un-detected post-manoeuvre track. Considering the typical polar LEO revisit time, these reference orbits are referred to at least 2 days before the last track in the window. To make an example (numerating tracks in ascending order), if an observation window contains tracks from number 4 to 21, the reference orbit is the one computed with tracks 1 up to 18.

2. *If no manoeuvre is detected* (using the scheme presented in Section 3.1), a **new reference orbit** is **recomputed** via batch least-squares orbit determination employing the tracks within the observation window (and be used in subsequent steps). The high-fidelity OD is based on the numerical propagator described in Table 4.3.

3. *If a manoeuvre is detected*, the **manoeuvre estimation** algorithm is executed with the reference orbit (which is then the pre-manoeuvre orbit), and an **a-priori** manoeuvre **estimate** is computed.

   (a) If the manoeuvre is estimated with *up to 3 post-manoeuvre tracks*, it is not considered to be fully reliable.

   (b) On the other hand, if a manoeuvre is estimated with associations of *4 post-manoeuvre tracks* (enough to estimate a full orbit [93]), the estimates are deemed to be reliable, and the manoeuvre is considered to be confirmed.

   A **post-manoeuvre orbit** is then computed via batch-least squares orbit determination, adding the manoeuvre itself (manoeuvre vector and epoch) as a **dynamical parameter to be re-estimated**. In case of associations of less than 4 tracks, the post-manoeuvre orbit is still computed since for cataloguing purposes it is important to keep custody of the observations and have an up-to-date catalogue.

4. *Following the determination of a post-manoeuvre orbit with a confirmed manoeuvre*, the orbit is compared to the tracks of the newest observation window in the subsequent simulation step.

   (a) If the residuals of the tracks do *not trigger any manoeuvre detection* (meaning that their WRMS fall below the primary and secondary thresholds), both the manoeuvre estimate and the post-manoeuvre orbit are taken as the **new references** and the loop is continued. The manoeuvre is included as an estimation

parameter in the orbit determination processes of the subsequent steps for as long as the observation window includes both pre- and post-manoeuvre tracks, in order to refine its value.

(b) If the residuals of the tracks *trigger again manoeuvre detection*, meaning that the WRMS is still high, the manoeuvre and post-manoeuvre orbit estimation were not satisfactory. This situation occurs when the true manoeuvre that was tried to be estimated is a **long burn** (in the order of 10-15 minutes, which is a non-negligible portion of the orbital period).

To provide a reference, Figure 4.4 shows the distribution of the 22 true manoeuvres according to the time difference between the manoeuvre epoch and the arrival of the first post-manoeuvre track, $t_i - t_M$, and the difference between the manoeuvre epoch and the arrival of the fourth manoeuvre track, $t_f - t_M$. It is possible to notice that for the 31% of the manoeuvres (7 out of 22), the first 4 tracks arrive in the first 40 hours after the manoeuvre epoch, with the first one arriving in less than 5 hours. The most extreme case occurs when the first track arrives over 45 hours after the manoeuvre time and the fourth one arrives in more than 80 hours.

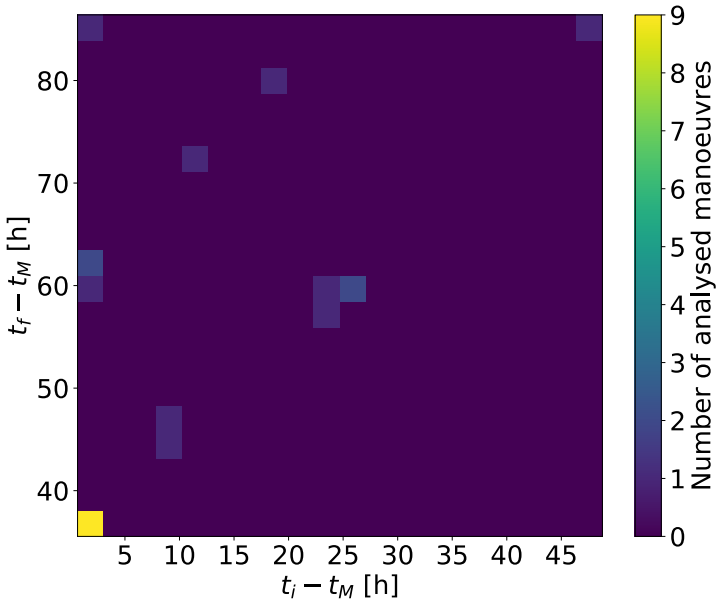

Figure 4.4: Distribution of the true manoeuvres according of the arrival times of the 1st and 4th track.

The selection of 4 as the number of post-manoeuvre tracks for a manoeuvre to be confirmed is suggested from the analysis of the test cases. Also associations of 3 tracks provided good results, but it was decided to have a safer margin. This is in-line with the results of literature regarding track-to-track associations [55], which states that 3 or 4 tracks are

usually sufficient to obtain correct correlations. As a reference, for a full RSO initialisation at least 4 tracks are required [93]. Good estimates could also be obtained with 2 tracks, but this proved not to be always the case. There is a large number of factors which can influence the results of the correlation, such as the manoeuvre magnitude, the manoeuvre direction, the time between tracks and the manoeuvre epoch, the time separation of tracks and observability issues. Hence, performing a parametric analysis to determine the impact of the single variables is a hard task.

The last point described in the workflow, concerning the detection of longer burns, derived from the analysis of 3 years of manoeuvres, as it was assessed that high residuals after manoeuvre estimation with 4 post-manoeuvre tracks only occurred when the true burn could not be considered impulsive anymore (with duration greater than $\approx 10\%$ of the orbital period, which is approximately 10 minutes[1].). This occurrences are due to the limitations of the proposed manoeuvre estimation algorithm, which correlates the orbit to the tracks via an impulsive burn. A test case representing a long burn will be presented in Section 4.4.3. In future developments of this work, the manoeuvre duration will also be added as a dynamical parameter to be estimated via the OD process, to increase the robustness of the simulation chain in these situations.

The second step of the estimation of the manoeuvre is done by introducing a **manoeuvre vector error** $\boldsymbol{\epsilon_u}$ and a **manoeuvre epoch error** ϵ_{t_M} as parameters, such that the first estimate can be re-estimated as:

$$\hat{\mathbf{u}}_{re} = \hat{\mathbf{u}} \cdot (1 + \boldsymbol{\epsilon_u}) \tag{4.3a}$$

$$\hat{t}_{M,re} = \hat{t}_M + \epsilon_{t_M} \tag{4.3b}$$

These two parameters can be introduced in the orbit determination process by computing their transition-sensitivity product (namely, the partial derivatives of the measurements with respect to these errors, similarly to Equation (3.11)) and including their contributions for each observation in the normal equations matrix. The transition-sensitivity matrices are calculated numerically via a 2^{nd} order central differences scheme.

A visual representation of the process at a simulation step k (resembling the maintenance scheme in Figure 1.7) is presented in Figure 4.5. The track-to-track association step is reported in the figure, even if it is not required in this simulation, since tracks are known to belong to the same object and are considered to be already associated. This process will be instead crucial for manoeuvre detection and estimation with tracks and orbits of

[1]The nominal orbital period of Sentinel 3-A is 108 minutes [94]

different satellites, in order to obtain associations of UCTs belonging to the same objects.

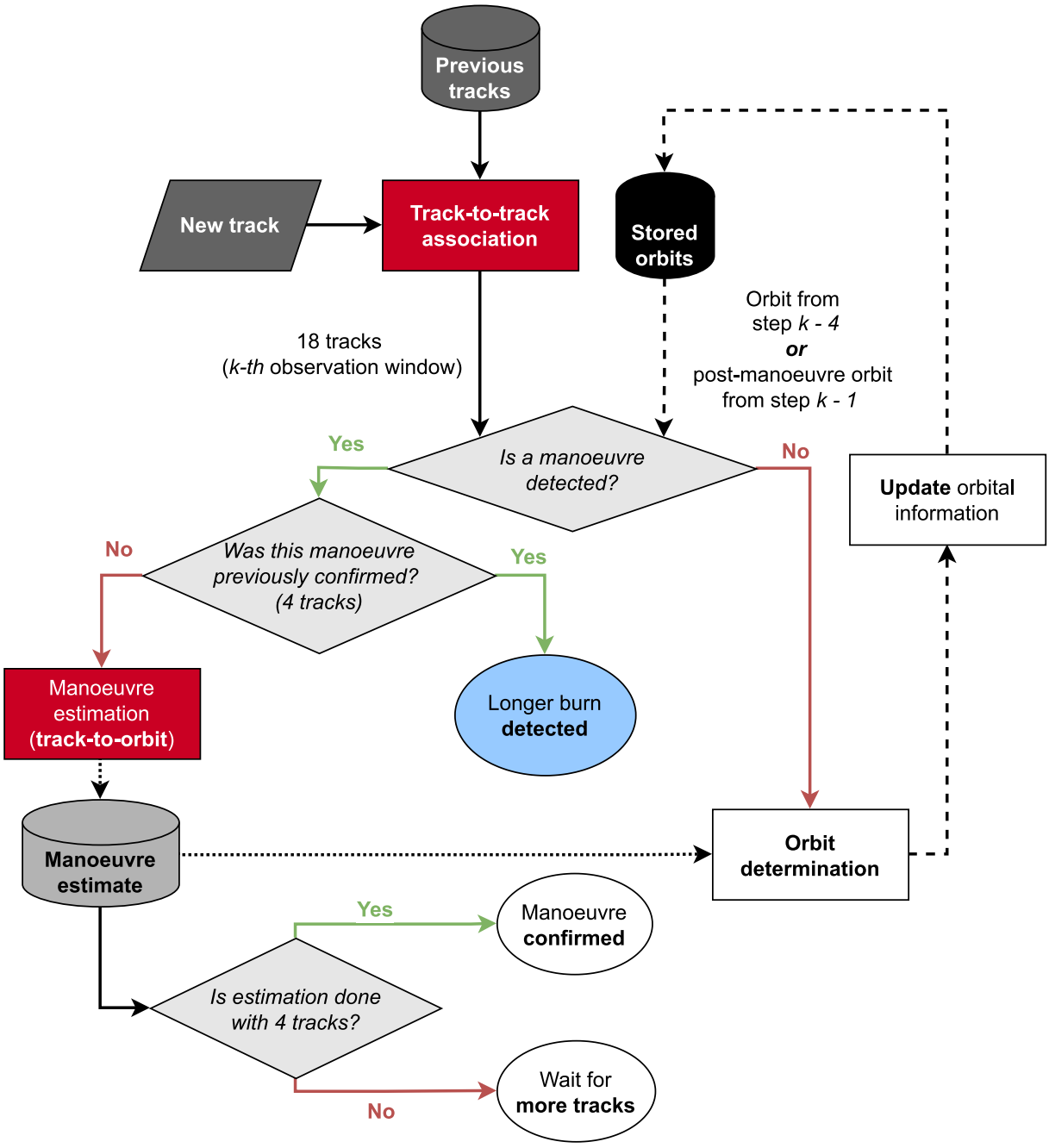

Figure 4.5: Graphical representation of the simulation scenario.

4.3. Results for manoeuvre detection

The primary and secondary thresholds to trigger manoeuvre detection are set to **5.0** and **2.5** respectively. For the application of the secondary threshold, it has been selected a maximum of **14 hours** to look for previous post-manoeuvre tracks. This value is slightly greater than the generic revisit time of a LEO satellite on a polar orbit.

To be consistent with detection theory, the following definitions are adopted:

1. the true manoeuvres which are correctly detected are labelled as **true positives**.
2. manoeuvres which do not occur but are still detected are named **false positives**.
3. true manoeuvres which are not detected are defined as **false negatives.**

The selection of these thresholds for the WRMS metric proves to be robust for manoeuvre detection. In fact, all 22 manoeuvres in the simulation time span are correctly detected, leading to 22 true positives and 0 false negatives. Even so, false positives are triggered in cases with long burn times (in the order of 10-15 minutes), as the estimation of the post-manoeuvre orbit and of the manoeuvre itself can be poor, generating high track residuals. As already mentioned, this effect is due to the limiting assumptions of the manoevure estimation algorithm. Some statistics regarding the performances of the manoeuvre detection strategy are reported in Table 4.5 and through a confusion matrix in Figure 4.6.

	Number	**Percentage**
True positives	22	75.86%
False positives	7	24.14%
False negatives	0	0%
Total	29	100 %

Table 4.5: Report of manoevure detection statistics.

However, there are three cases, reported in Table 4.6, where the first post-manoeuvre track is not immediately detected. This can be attributed to the fact that it arrives closely to the burn epoch and that the corresponding manoeuvre has relatively low magnitude. Nevertheless, the information about these observations are recovered and employed for manoeuvre estimation as soon as the second post-manoeuvre track, detected via the primary threshold, arrives, thanks to the application of the lower secondary threshold.

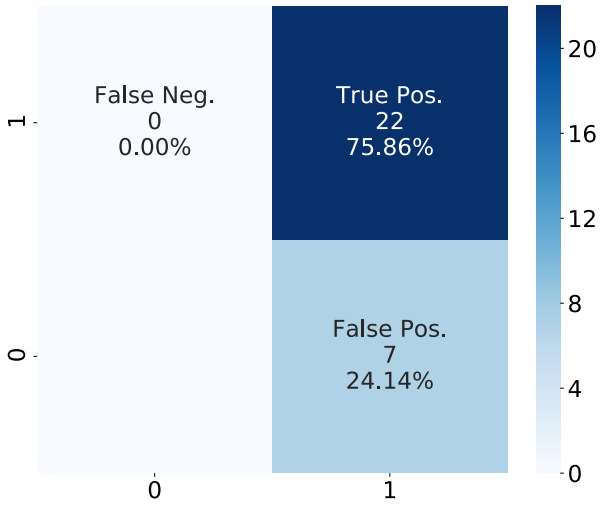

Figure 4.6: Confusion matrix for manoeuvre detection.

Manoeuvre epoch t_M	**Arrival time of first post-man. track**	**Manoeuvre vector (RIC frame)** $[mm/s]$
23/02/2017 09:40:17	1 h 11 min 17 s	$[-0.03, 4.02, 1.24]^T$
12/07/2017 09:44:24	1 h 0 min 55 s	$[-0.11, 5.59, 0.82]^T$
27/11/2019 08:04:59	2 h 25 min 48 s	$[-0.08, 3.22, -0.02]^T$

Table 4.6: Manoeuvres not detected at the first post-manoeuvre track.

Finally, it is important to remark that the selected values for the thresholds and the number of past hours have proven to be effective in this simulated scenario, but that a finer tuning could be required in order to adapt the methodology to a wider variety of cases.

4.4. Results for manoeuvre estimation

This subsection presents a set of results obtained by the application of the manoeuvre estimation algorithm, tested in the scenario using the Keplerian + linear perturbations dynamical model, and of the subsequent re-estimation via high-fidelity OD. The selected discretisation step for $t_M \in T$ is of 9 minutes, approximately 9% of the orbital period of the satellite. Section 4.4.1 presents some overall results obtained by the application of the two-step estimation, validating the process and showing how the estimation can improve with an increasing number of post manoeuvre tracks. This last theme is also reprised in Section 4.4.2, which presents a test case of the estimation of an impulsive manoeuvre,

supporting the choice of taking 4 tracks to confirm a manoeuvre and that the selection strategy for the selection of the most suitable a-priori estimate is effective. Section 4.4.3 highlights the major limitation of the methodology, which is the estimation of long burns. Finally, Section 4.4.4 presents a short analysis of the impact of the time elapsed since the manoeuvre and track separation on associations of 2 and 3 tracks.

4.4.1. General results

In order to understand the general performances of the proposed two-step estimation methodology, this subsection presents an overview of the results obtained for the estimation of the 22 manoeuvres performed in years 2017, 2018 and 2019 by Sentinel 3-A. Here, the two parameters which are considered to define the quality of the manoeuvre estimates are the errors in the estimated vector and the estimated epoch.

Figures 4.7 to 4.10 report the distributions of the estimation errors of the epoch and of the relative manoeuvre magnitude error (knowing the true manoeuvres). The smaller graphs in each figure represent the distribution (and the Cumulative Distribution Function, CDF) of the solutions according just to the magnitude error (on top) and the epoch error (on the right). The plots are presented for associations of an increasing number of post-manoeuvre tracks, from 1 to 4. Defining an association of post-manoeuvre tracks as a set of tracks {1, 2, 3, 4}, the associations in the distributions are {1}, {1, 2}, {1, 2, 3} and {1, 2, 3, 4}. The graphs on the left report the estimates coming from the estimation algorithm (using the Keplerian + linear perturbations dynamical model), while those on the right are the subsequent re-estimations of the first guesses employing high-fidelity orbit determination (point 3 in the workflow of Section 4.2).

The distributions on the left side show that, for an increasing number of post-manoeuvre tracks, the estimation error on both magnitude and epoch of the estimation algorithm tends to decrease, as well as the dispersion of the points. Associations of 1 track cannot be considered reliable since errors can reach very high values for both magnitude and epoch. The estimation is mediocre since a low number of measurements is involved and, at times, also because the track is received shortly after the manoeuvre, having such modest divergence with respect to the pre-manoeuvre orbit that is not captured by the estimation algorithm (due to the noise of the measurements and the accuracy of the dynamical model). For associations of 2 tracks, errors can reach up to 200% in magnitude and 800 minutes in epoch, which drop to 75% and 150 minutes for 3 tracks, and finally to maximum 60% and 100 minutes for 4 tracks. This confirms the choice of 4 as the number of post-manoeuvre tracks to confirm a reliable first manoeuvre guess (being in line with

literature), since the errors are at their minimum and the dispersion of the points is the lowest among all associations; nonetheless, also associations of 3 tracks can be eventually considered with a higher degree of uncertainty on the estimation. The outliers in terms of manoeuvre epoch are represented by long burns, which, as already stated, are not properly evaluated by the estimation algorithm and ambiguities in the selection of the first estimate arise, as it will be shown in Section 4.4.3. It is worth to notice that the errors in the manoeuvre epoch are multiples or fractions of the orbital period of the satellite (approximately equal to 100 minutes). Associating more than 4 tracks could be beneficial but also lead to poor estimations, since the dynamical models (both the linear one and the Keplerian + linear perturbations) could start diverging for tracks far from the manoeuvre epoch in cases of higher magnitude burns. Moreover, the computational cost of the manoeuvre estimation algorithm would increase as more measurements should be processed.

On the other hand, the distributions on the right side, related to high-fidelity orbit determination, show how the estimation error and the dispersion can improve in the second iteration of estimation. It is possible to notice that, for all numbers of associated tracks, this step benefits both the error on magnitude and epoch, though having a greater impact on the first one than on the second. This result was expected, as this estimation step is multi-parameter (since it considers both the manoeuvre vector and epoch) and is supported by a numerical propagator with higher fidelity with respect to the one developed in Section 3.2.3.

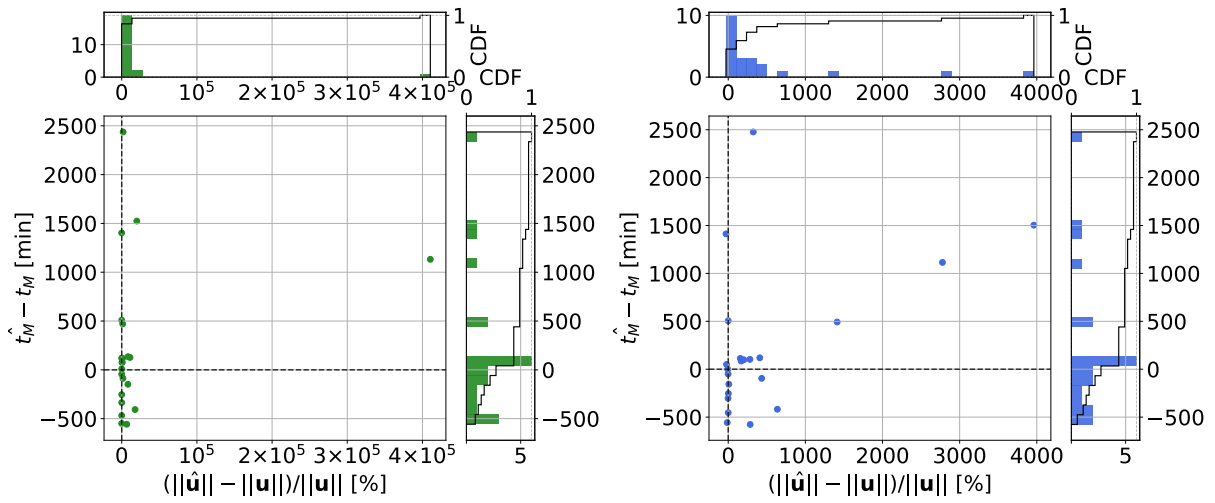

(a) (b)

Figure 4.7: Distribution of manoeuvre estimates (left) with estimation algorithm and high-fidelity orbit determination (right) (*1 track*).

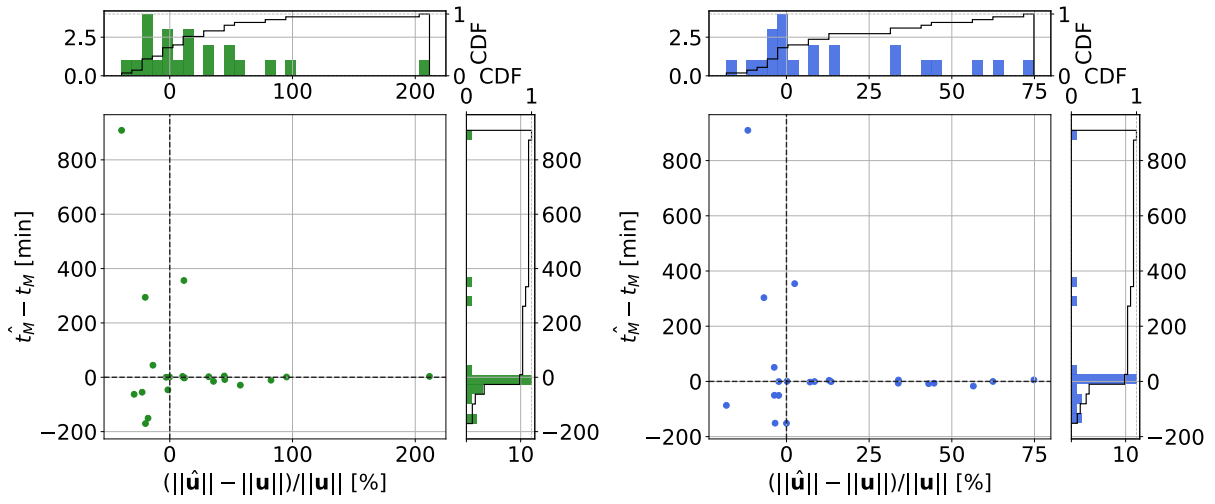

(a) (b)

Figure 4.8: Distribution of manoeuvre estimates (left) with estimation algorithm and high-fidelity orbit determination (right) (*2 tracks*).

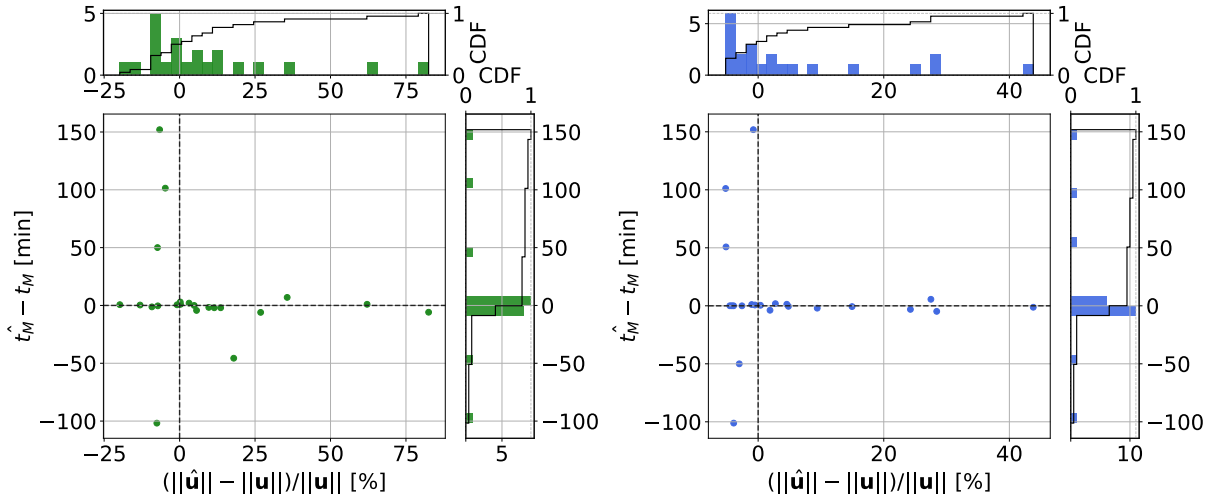

(a) (b)

Figure 4.9: Distribution of manoeuvre estimates (left) with estimation algorithm and high-fidelity orbit determination (right) (*3 tracks*).

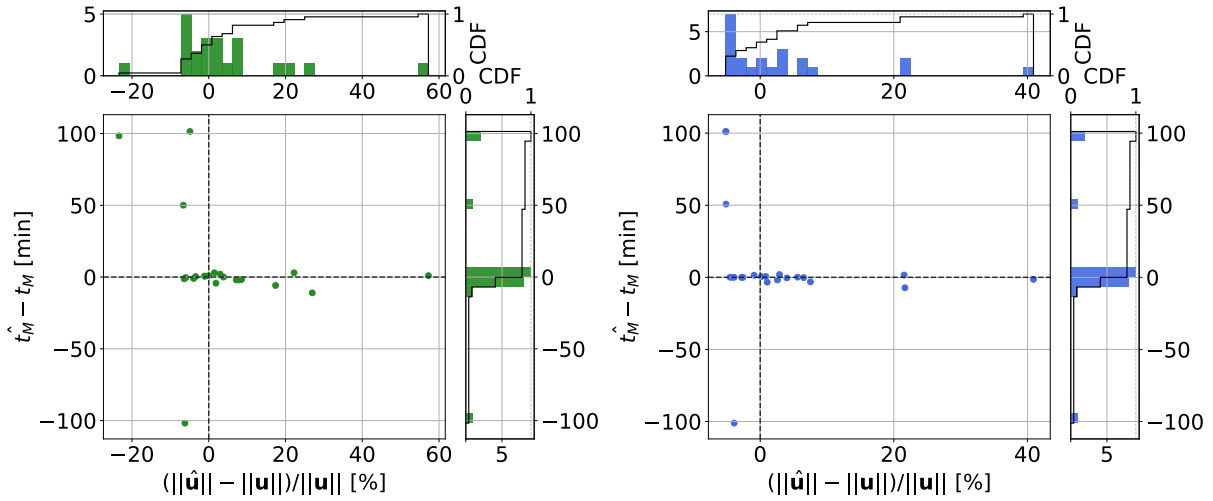

(a) (b)

Figure 4.10: Distribution of manoeuvre estimates (left) with estimation algorithm and high-fidelity orbit determination (right) (*4 tracks*).

Similarly to the previous ones, Figures 4.11 to 4.14 show how the relative estimation errors, defined in absolute value in the RIC frame, evolve as function of the number of associated tracks. Each plot shows the distributions, set side by side, of the errors for the a-priori manoeuvre estimate and for its re-estimation. It is again clear how associating more tracks is beneficial to the estimation process as the errors become lower and the dispersion is reduced. The component better estimated by the algorithm is the in-track one, which can reach error below 0.1% for associations of 3 or 4 tracks. On the other hand, greater errors can be found for the radial and cross-track directions, reaching 80% and 175% respectively when considering 4 tracks. This situation can be attributed to the fact that radial and cross-track burns, considering the order of magnitude of the Sentinel 3-A manoeuvres, have a low impact on the dynamics of the orbit as their secular effect (related to variations in the orbital period, and so of in energy) is modest. Hence, the estimation algorithm is less sensitive to the variations of these components and it is harder to estimate them with better precision. Nonetheless, this topic shall be investigated more, as the accuracy of the measurements is expected to have an important role as well.

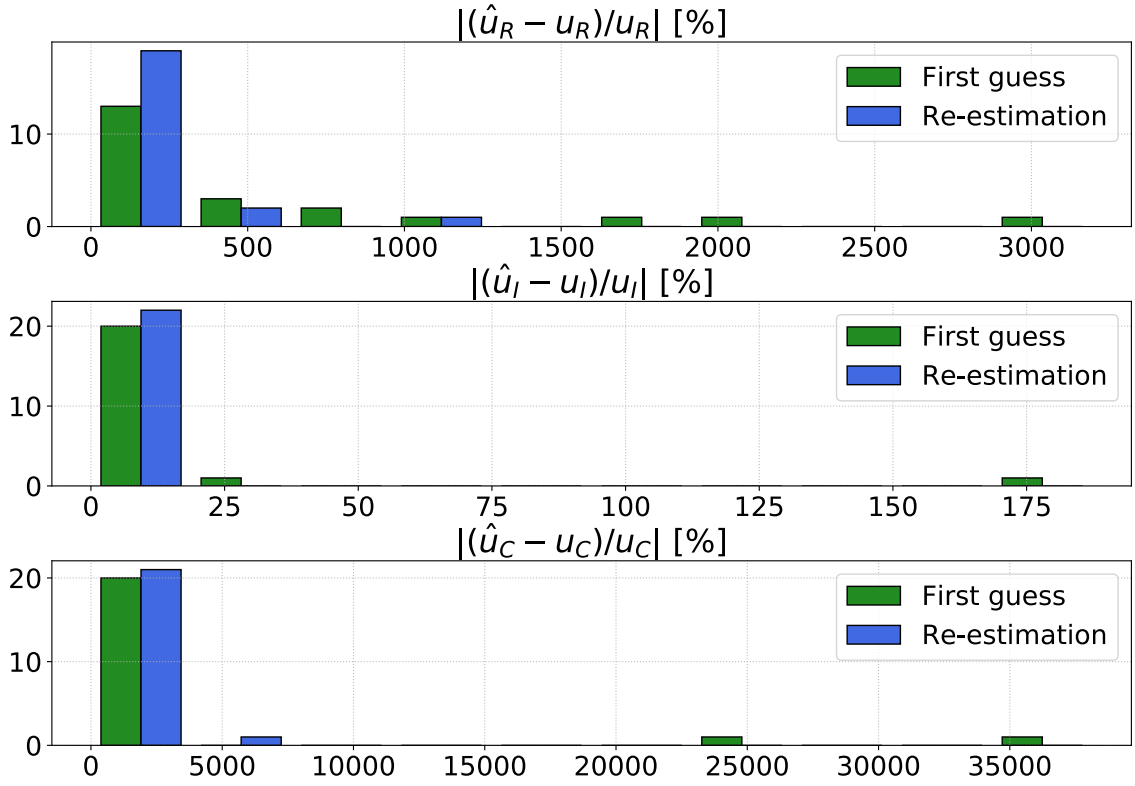

Figure 4.11: Distribution of the estimated manoeuvre components error (*1 track*).

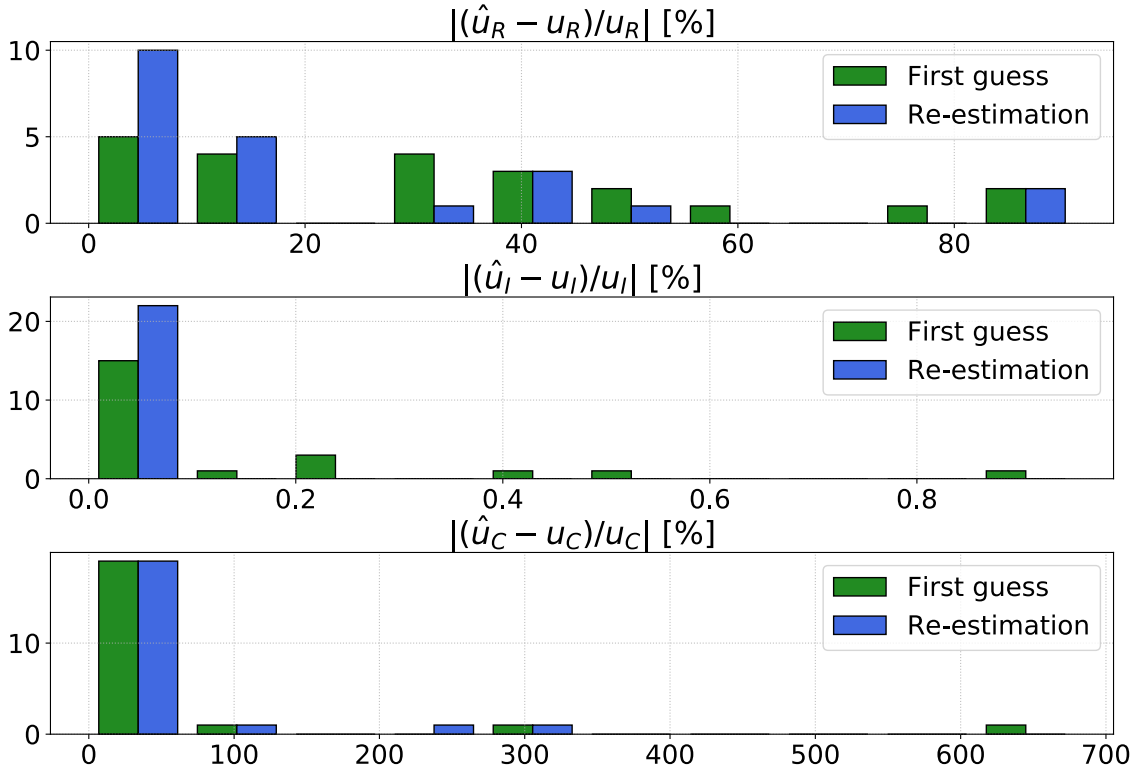

Figure 4.12: Distribution of the estimated manoeuvre components error (*2 tracks*).

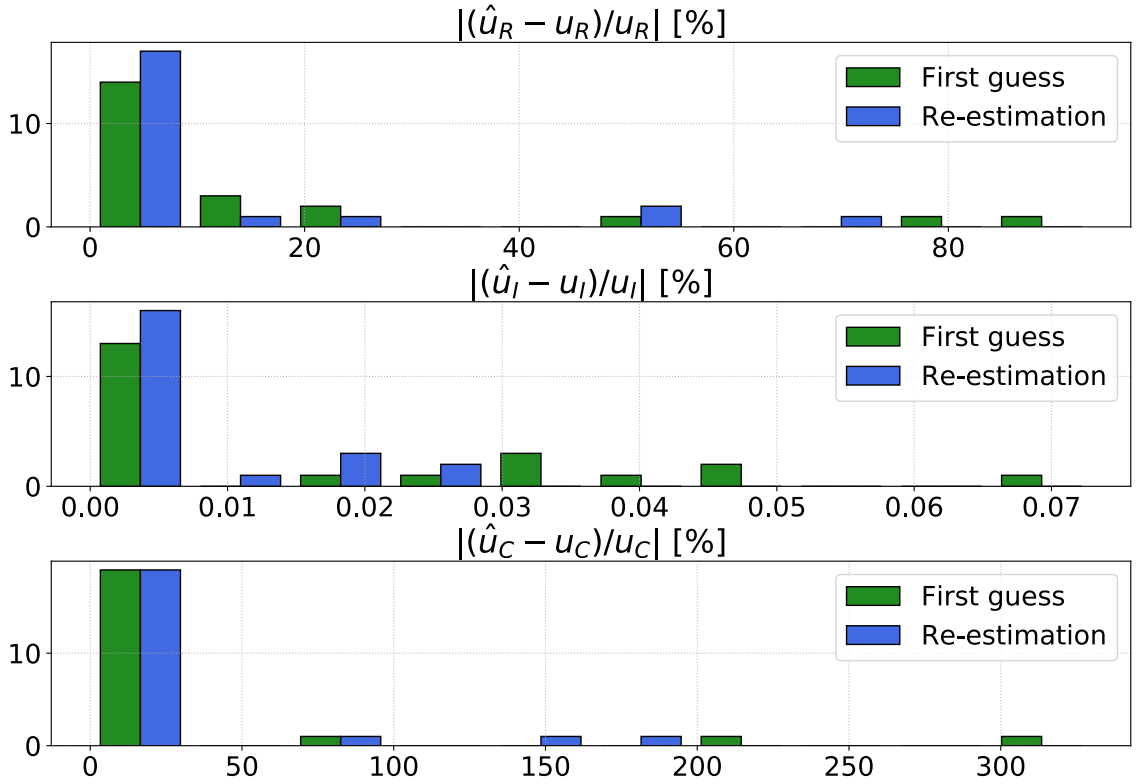

Figure 4.13: Distribution of the estimated manoeuvre components error (*3 tracks*).

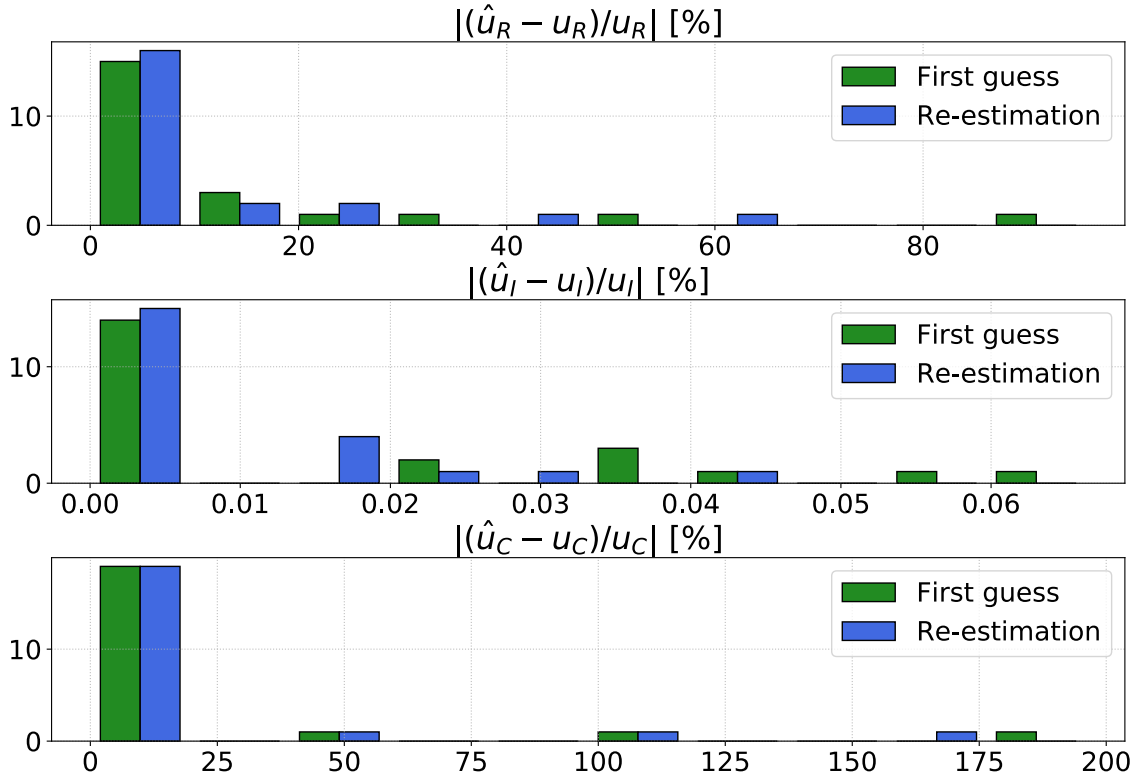

Figure 4.14: Distribution of the estimated manoeuvre components error (*4 tracks*).

4.4.2. Test case: impulsive manoeuvre

This subsection presents a test case taken from one of the 22 manoeuvres (representing an impulsive burn). The manoeuvre estimation is carried out employing the estimation algorithm with the Keplerian + linear perturbations dynamical model. The characteristics of the true manoeuvre are reported in Table 4.7. The manoeuvre vector is reported in the RIC frame. The arrival times represent the time in which tracks, whose duration is approximately 2 minutes, are generated. For the sake of simplicity, the involved post-manoeuvre tracks are numbered sequentially in the set {1, 2, 3, 4}.

Manoeuvre epoch t_M	July 12th, 2017, 09:44
Real manoeuvre components	$[0.111, 5.590, 0.819]^T$ mm/s
Manoeuvre magnitude	5.65 mm/s
Manoeuvre duration	3 s
Arrival time of tracks	t_M + 1 h, t_M + 11.5 h, t_M + 1 d, t_M + 1.5 d

Table 4.7: Characteristics of manoeuvre on July 12th, 2017.

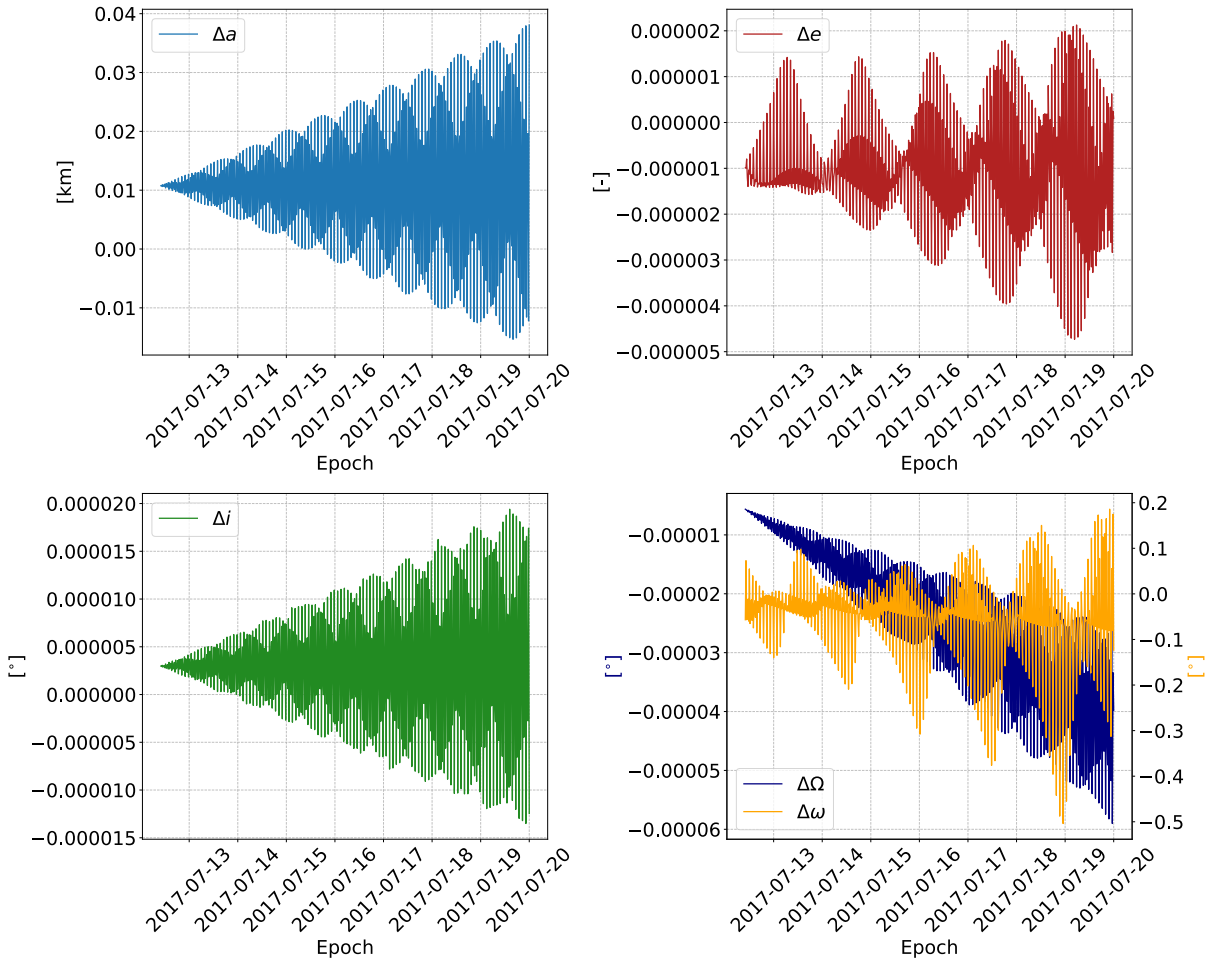

Figure 4.15: Differences in orbital elements of pre and post-manoeuvre orbit (manoeuvre on 12/07/17).

The manoeuvre has a major in-track component, so changes in the semi-major axis and eccentricity are expected to be noticeable. Figure 4.15 shows the evolution of the differences between the first five orbital elements (semi-major axis a, eccentricity e, inclination i, right ascension of the ascending node Ω and argument of pericentre ω) of the pre-manoeuvre and the post-manoeuvre orbits. All the differences in the orbital elements show periodic trends with increasing amplitude. The semi-major axis is the most affected parameter, showing a maximum difference of 40 m.

Figures 4.16 to 4.19 show the evolution of $\sqrt{J}$ and $\|\hat{\mathbf{u}}\|$ as a function of $t_M \in T$ for increasing number of associated tracks. The vertical dashed lines represent the true manoeuvre epoch and the estimated epoch $\hat{t}_M$. It is noticeable from Figure 4.16 that the manoeuvre estimation with a single track does not present any outstanding point or recognizable pattern, both in terms of $\sqrt{J}$ and $\|\hat{\mathbf{u}}\|$. As mentioned before, the estimation turns out to be not satisfactory since few measurements are used and as the track is

received very shortly after the manoeuvre. Any solution computed with a single track is generally not considered to be reliable.

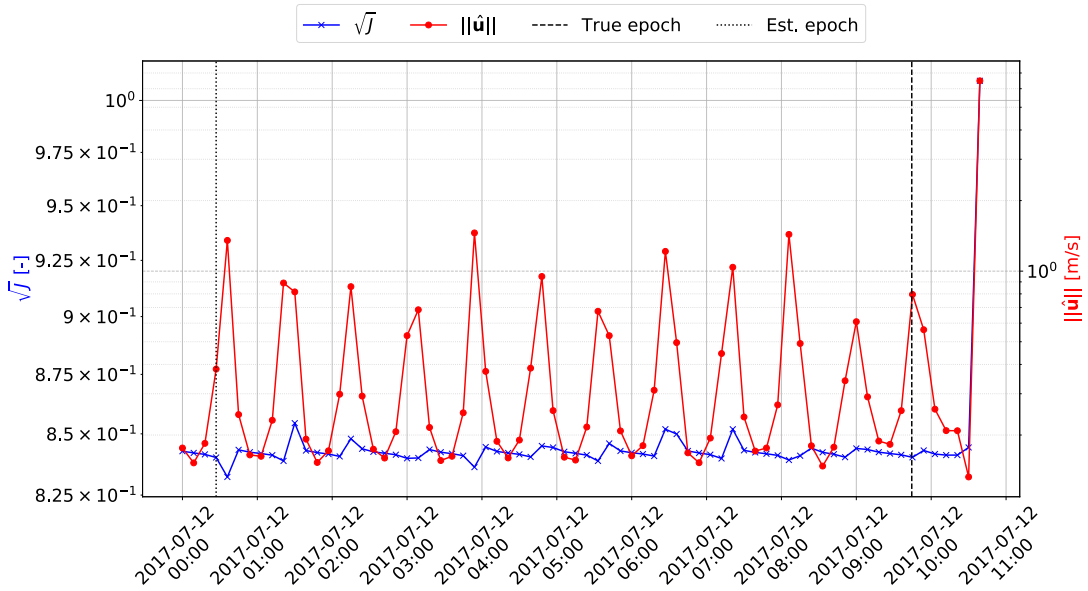

Figure 4.16: Initial estimation of manoeuvre on 12/07/2017 with tracks {1}.

Figure 4.17 presents the results of the manoeuvre estimation algorithm with the association of the first two post-manoeuvre tracks {1, 2}. The plots are less noisy than the previous case and different minima can be spotted. It is possible to see that the selected estimate has a very low epoch error (equal to the time discretization step), but the estimated manoeuvre (approximately 10^{-2} m/s) is one order of magnitude greater than the true one.

The functions $\sqrt{J}$ and $\|\hat{\mathbf{u}}\|$ show a different trend for associations of 3 tracks (Figure 4.18). Both the WRMS and the manoeuvre magnitude now present clear regions of minima, which are in general not coinciding and are separated by approximately 1.5 hours, equivalent to one orbital period of the satellite. This repetitive pattern can be associated to the in-track nature of the manoeuvre. The non-linear behaviour of the two functions and the dislocation of the minima is what suggested that a joint estimation of the manoeuvre vector and epoch estimation could not work; additionally, it was the rationale behind our selection strategy based on taking the optimal $\|\hat{\mathbf{u}}\|$ among the $\sqrt{J}$ minima.

The estimation with an association of 4 tracks, presented in Figure 4.19, highlights a solution that is optimal both in terms of WRMS and manoeuvre magnitude.

In this case, this minimum is exactly the chosen solution, being the most suitable estimate in the pool according to the proposed selection criterion. Its characteristics are reported

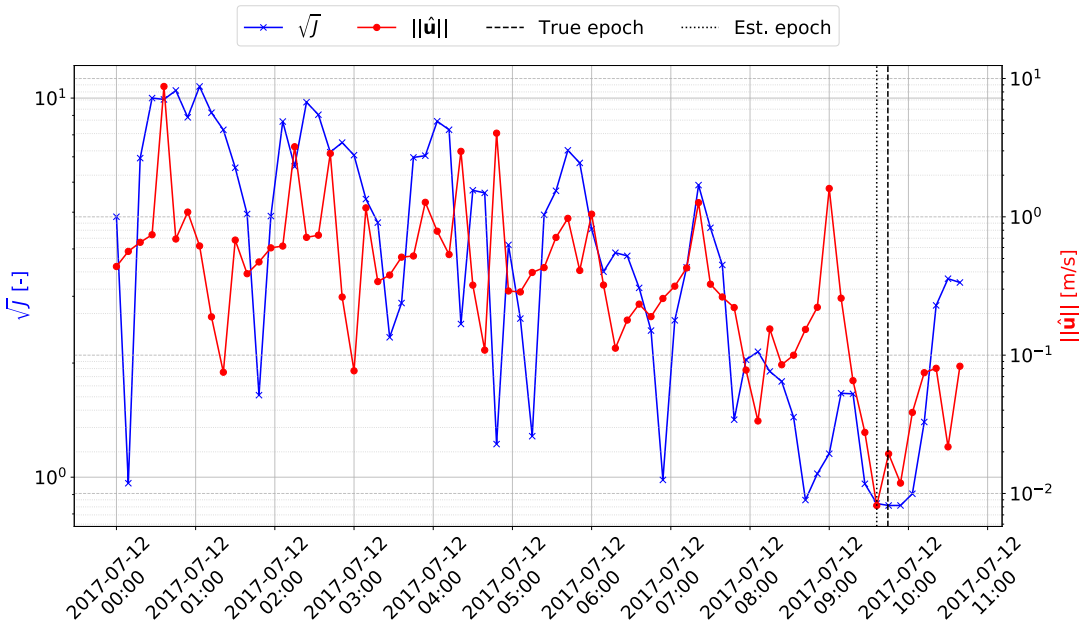

Figure 4.17: Initial estimation of manoeuvre on 12/07/2017 with tracks {1, 2}.

in Table 4.8. The manoeuvre epoch is very well estimated (with an error of 1 minute, due to time discretisation), as well as the in-track component of the manoeuvre, while slight errors are found on the radial and cross-track terms; nonetheless, the error in terms of magnitude (with respect to the true manoeuvre) is close to 1%. This estimate can be considered as a reliable first guess or initial estimate for the later complete estimation process.

Estimated $\hat{t}_M$	**Estimated $\hat{\mathbf{u}}$**	**Relative $\|\hat{\mathbf{u}}\|$ error**
July 12th, 2017, 09:45	$[0.354, 5.582, -0.02]^T$ mm/s	1.01 %

Table 4.8: Characteristics of chosen estimate for manoeuvre on 12/07/2017 with tracks {1, 2, 3, 4}.

Similar behaviours of $\sqrt{J}$ and $\|\hat{\mathbf{u}}\|$ as in Figure 4.19 are encountered in most of the test cases for associations of 4 post-manoeuvre tracks; differences can be present as the true manoeuvre shifts toward a more radial or a more cross-track burn, which has an impact on the period of the minima. An exception is made for some longer burns (10-15 minutes), in which the two functions might not show such clear patterns and the retrieved estimate can be unsatisfactory, both in terms of epoch and manoeuvre vector. This is expected, since the impulsive manoeuvre assumption of the estimation algorithm is not accurate at modelling the dynamics of a longer burn.

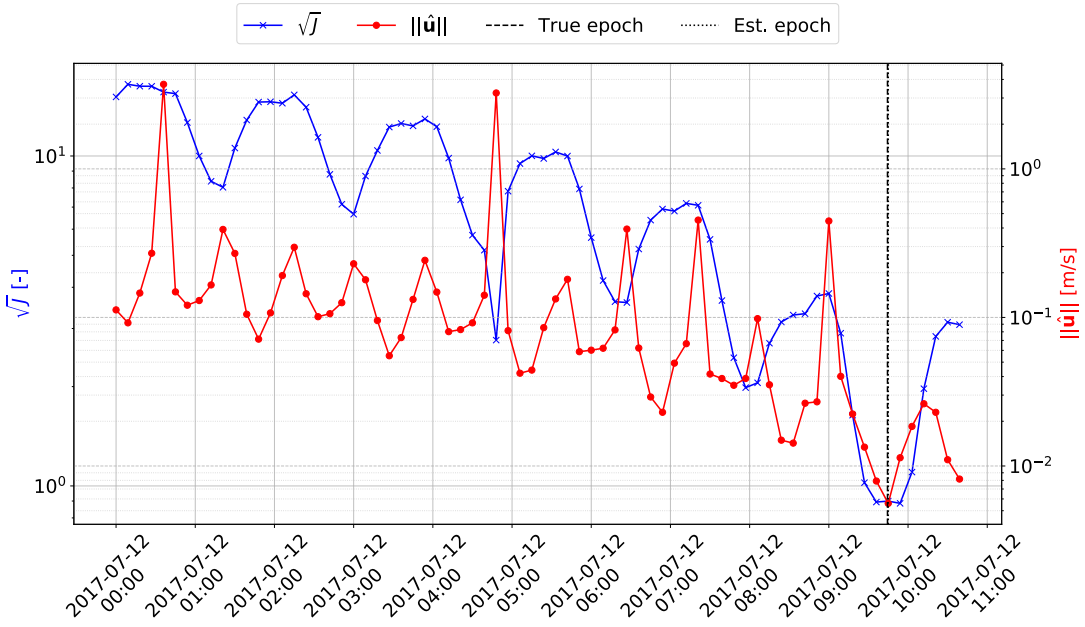

Figure 4.18: Initial estimation of manoeuvre on 12/07/2017 with tracks {1, 2, 3}.

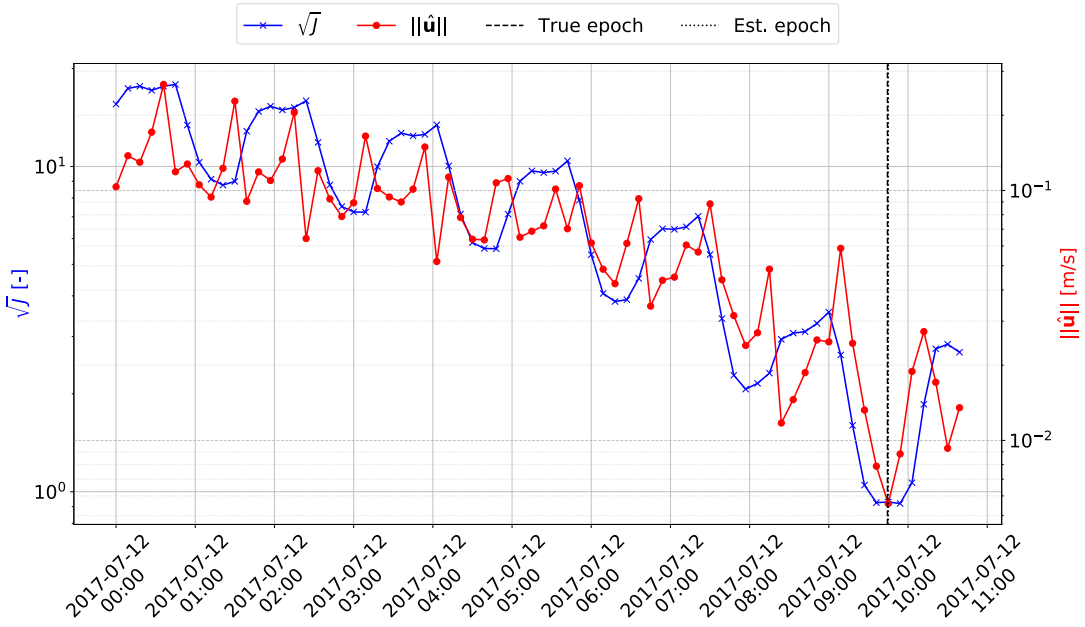

Figure 4.19: Initial estimation of manoeuvre on 12/07/2017 with tracks {1, 2, 3, 4}.

4.4.3. Test case: long manoeuvre

This subsection presents the result of the preliminary estimation of a long burn. The characteristics of the true manoeuvre are reported in Table 4.9. The manoeuvre vector is reported in the RIC frame. The involved post-manoeuvre tracks are numbered sequentially in the set $\{5, 6, 7, 8\}$. This manoeuvre is particularly harsh for the estimation algorithm, since it is a long burn with magnitude in the order of m/s.

Manoeuvre epoch t_M	September 6th, 2017 10:26
Real manoeuvre components	$[0.007, 0.014, 2.085]^T$ m/s
Manoeuvre magnitude	2.09 m/s
Manoeuvre duration	13.5 min
Arrival time of tracks	t_M + 1 d, t_M + 1.5 d, t_M + 2 d, t_M + 2.5 d

Table 4.9: Characteristics of manoeuvre on September 6th, 2017.

Figure 4.20 shows the differences in the first five orbital elements of the pre-manoeuvre and post-manoeuvre orbit. The manoeuvre has a major cross-track component but still an in-track component in the order of cm/s. In fact is possible to notice greater variations in the inclination (reaching maximum of 808 $mdeg$) and in the semi-major axis ($\approx$ 100 m), as well as a drift of the right ascension of the ascending node.

Figures 4.21 and 4.22 present the results of the application of the estimation for the association of tracks {5, 6, 7} and {5, 6, 7, 8}.

It is possible to observe that the $\sqrt{J}$ and $\|\hat{\mathbf{u}}\|$ minima are separated by approximately 50 minutes, which is half the orbital period of the satellite, due to the greater cross-track component of the manoeuvre. In Figure 4.21, three minima with $\sqrt{J} > 10$ can be identified. Associating the 4^{th} post-manoeuvre track allows to reduce this number to 2; however, in both cases, there is no clear solution standing out, as opposed to the test case with an impulsive manoeuvre. It is also noticeable that the solution closest to the manoeuvre epoch is associated to a local $\sqrt{J}$ minimum but is not included in the selection pool since its value is greater than the 115% of the absolute minimum. The selection strategy for the most suitable estimate therefore fails for both associations. Table 4.10 reports the characteristics of the estimated manoeuvre. The error on the manoeuvre epoch is approximately 1.5 hours (or one orbital period), while the relative error with respect to the true manoeuvre is 6.20%. The estimation error on the cross-track component is smaller component than the other two.

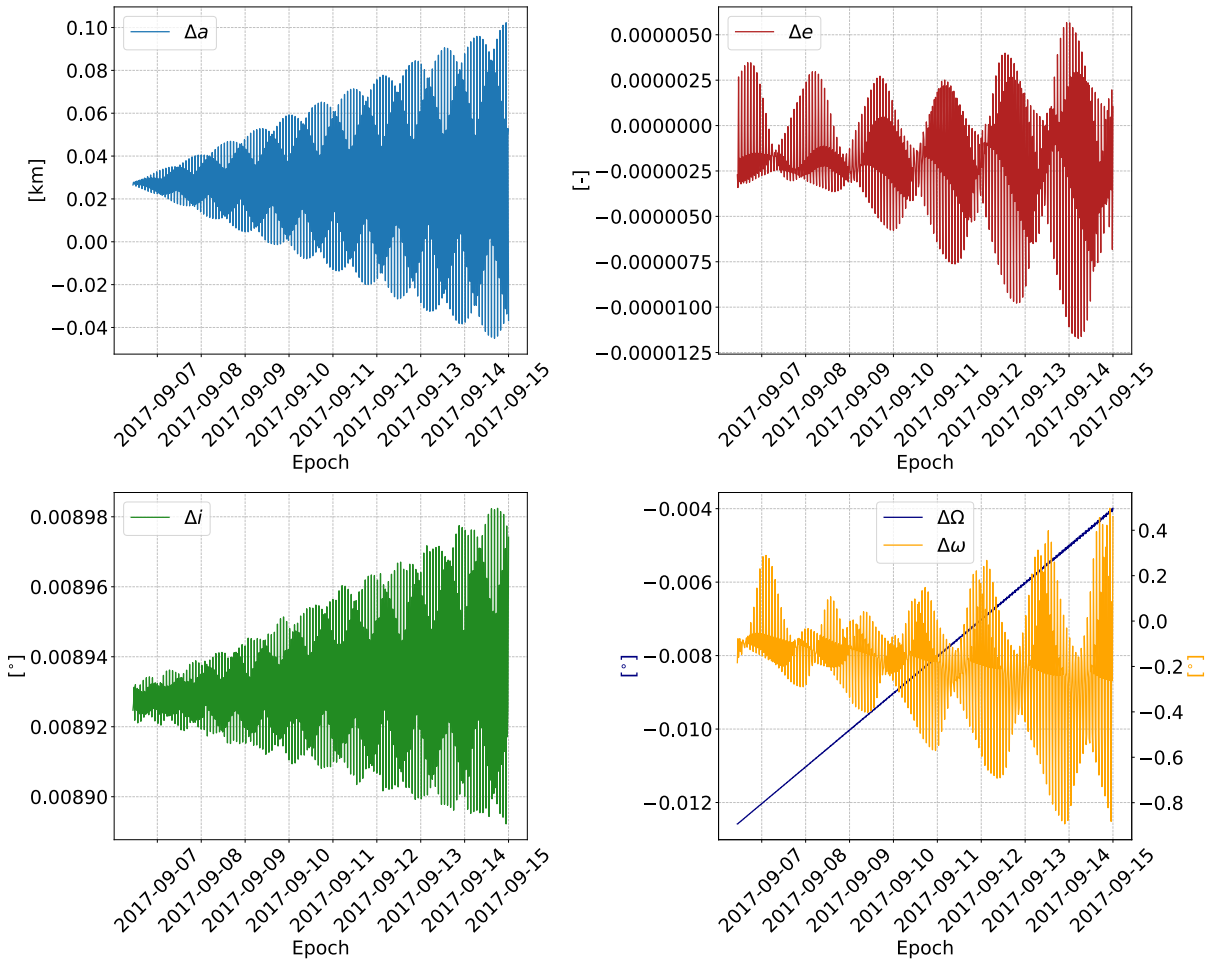

Figure 4.20: Differences in orbital elements of pre and post-manoeuvre orbit (manoeuvre on 06/09/17).

Estimated $\hat{t}_M$	Estimated $\hat{\mathbf{u}}$	Relative $\|\hat{\mathbf{u}}\|$ error
Sept. 6th, 2017, 08:51	$[-0.029, 0.013, 1.956]^T$ m/s	6.20 %

Table 4.10: Characteristics of chosen estimate for manoeuvre on 06/09/2017 with tracks $\{1, 2, 3, 4\}$.

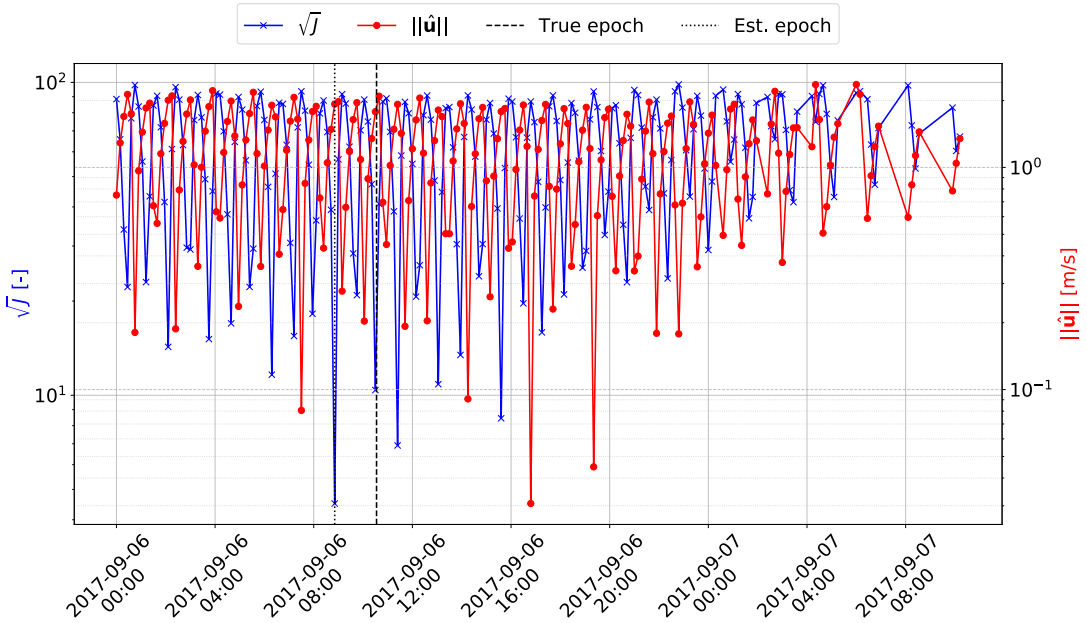

Figure 4.21: Initial estimation of manoeuvre on 06/09/2017 with tracks {5, 6, 7}.

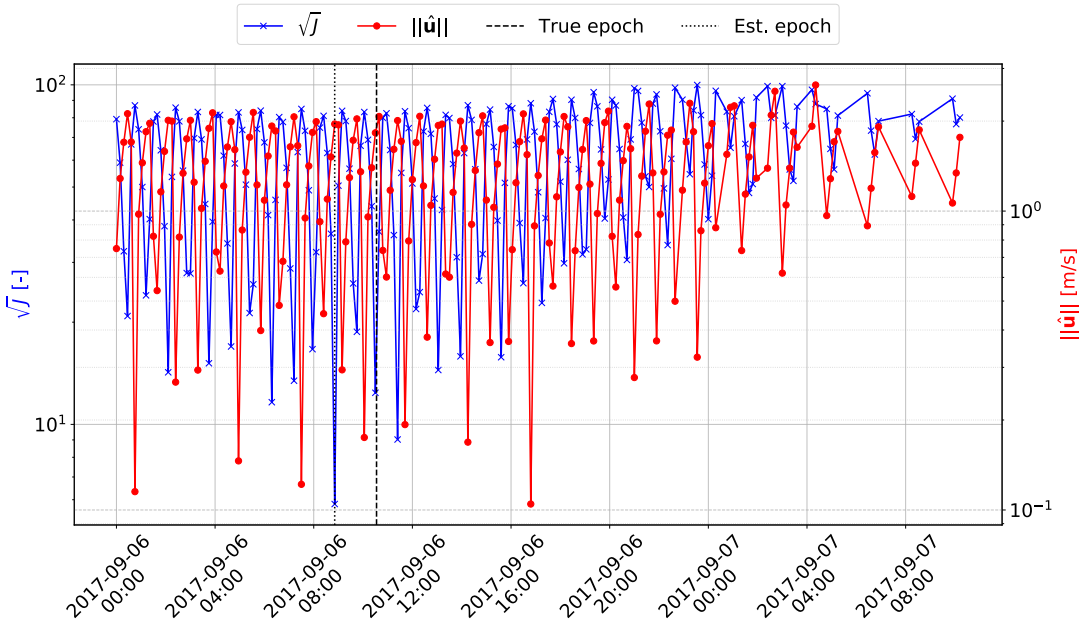

Figure 4.22: Initial estimation of manoeuvre on 06/09/2017 with tracks {5, 6, 7, 8}.

As already mentioned, this result is due to the limited applicability of the manoeuvre estimation algorithm based on an impulsive assumption. Since those long manoeuvres are however properly detected, one possible way to overcome this problem would be to estimate the manoeuvre duration as well as part of the orbit determination process once the a-priori values of manoeuvre time and size have been computed based on impulsive

assumption. This task will be reprised in future developments of this work.

4.4.4. Impact of track separation and time elapsed since manoeuvre on estimation

The parameters which can influence the output of the manoeuvre estimation algorithm are many. It is expected that the manoeuvre magnitude, its direction, the location on the orbit where it is executed, the orbital regime, the time elapsed between the manoeuvre epoch and the tracks, the time separation between tracks, the number of observations and the accuracy of the tracks can have an impact, as well as the accuracy of the dynamical model. The number of these elements is large, and it is hard to perform any parametric analysis to determine how the estimation varies with each of them. For this reason, the typical statement of 3 or 4 tracks required to correctly solve association problems or initialise the orbit of an RSO comes from experience thanks to the analysis of large amounts of data. Nevertheless, the topic of track separation and time elapsed since the manoeuvre is investigated for associations of 2 or 3 tracks, to understand if they can noticeably affect the accuracy of the estimation. The research is conducted only for these types of associations to understand why they are less performing than associations of 4 tracks. At first, one might conclude that, considering the order of magnitude of Sentinel 3-A manoeuvres, having tracks very close to the manoeuvre epoch can be disadvantageous since the manoeuvre has not had a detectable impact on the orbit yet, leading to poor estimation such as in the 1 track case (as in Figure 4.16). This is expected as in the majority of the cases (referring to Figure 4.4) the first track arrives in a couple of hours after the manoeuvre epoch, and the 2^{nd} one can be just separated by 12 hours (approximately 7 orbital periods). On the other hand though, higher errors for larger times passed since the burn epoch can be supposed due a loss in accuracy of the dynamical model. Hence, from this preamble, one would expect to see a recognisable trend that the errors follow as the two variables change, possibly identifying an optimal region where the accuracy of the estimation is at its maximum.

To this aim, the estimations coming from all associations of 2 or 3 tracks are analysed, even if the tracks are not consecutive. For sake of clarity, considering a set of post manoeuvre tracks {1, 2, 3, 4}, the possible associations of 2 tracks are {1, 2}, {1, 3}, {1, 4}, {2, 3}, {2, 4}, {3, 4}; for 3 tracks instead, they are {1, 2, 3}, {1, 2, 4}, {1, 3, 4} and {2, 3, 4}. Figure 4.23 shows the estimation errors of magnitude and epoch with associations of 2 tracks as $t_{i,1}$, the start time of the first post-manoeuvre track and $t_{f,2}$, the end time of the second one, vary with respect to t_M, the true manoeuvre epoch. Similarly, Figures 4.24 and 4.25 show the same errors but for associations of 3 tracks. In this case, $t_{f,3}$ is the end

time of the third considered post-manoeuvre track.

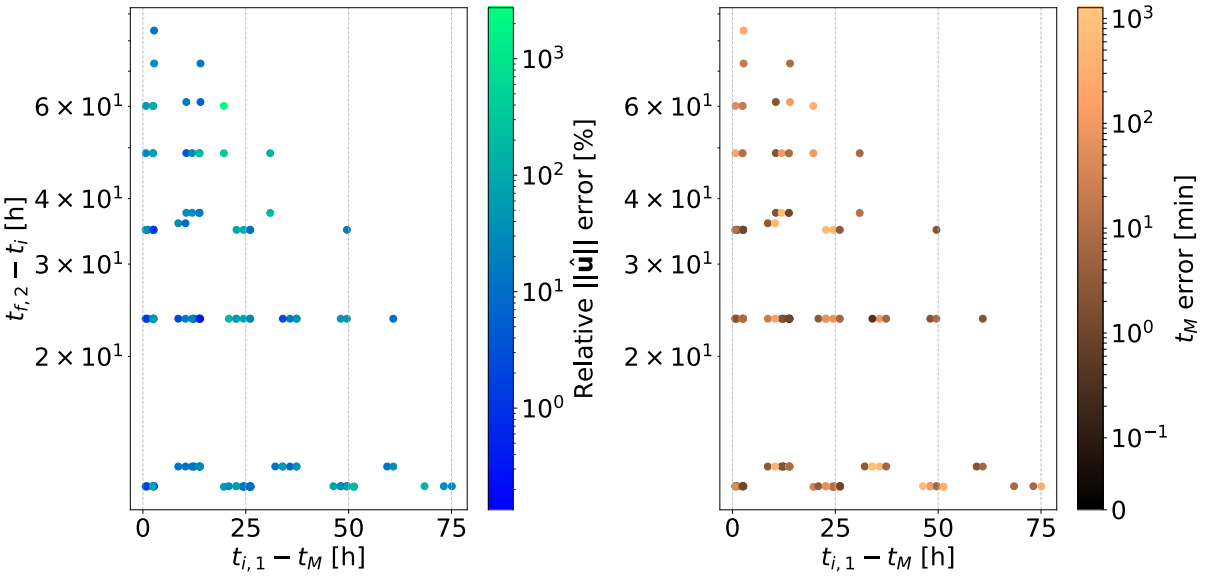

Figure 4.23: Variation of estimation errors (*relative magnitude* and *epoch*) for different associations of *2 tracks*.

As it is possible to notice in the plots, differently from the preliminary statements, there is not any evident trend of the errors as more time has passed since the manoeuvre and as the tracks get more separated. It it possible to state that, at least for the considered orbit and manoeuvres in this simulation scenario, the two variables do not seem have a noticeable impact on the quality of the estimation. Of course, the sensitivity of the algorithm shall be tested more with different cases, varying the other parameters which affect the quality of the estimation.

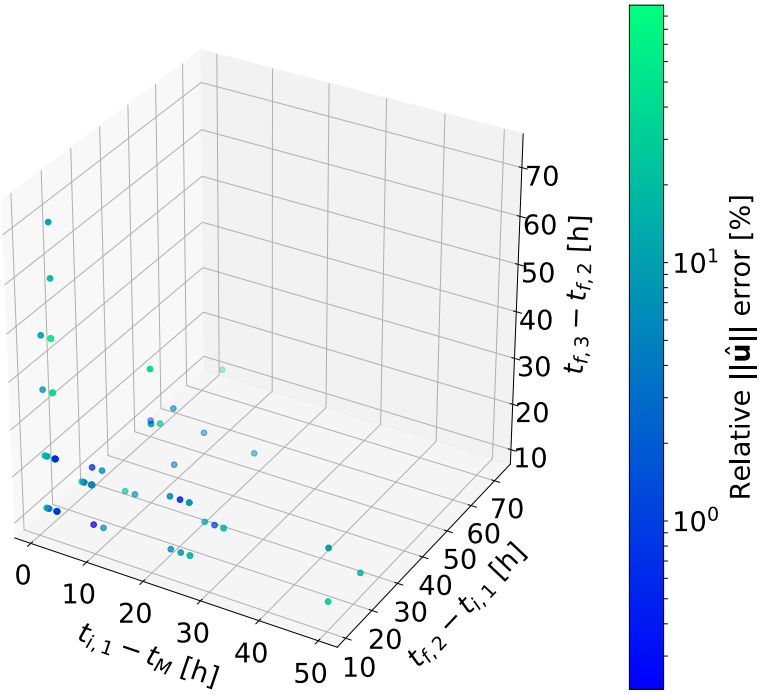

Figure 4.24: Variation of estimation error (*relative magnitude*) for different associations of *3 tracks*.

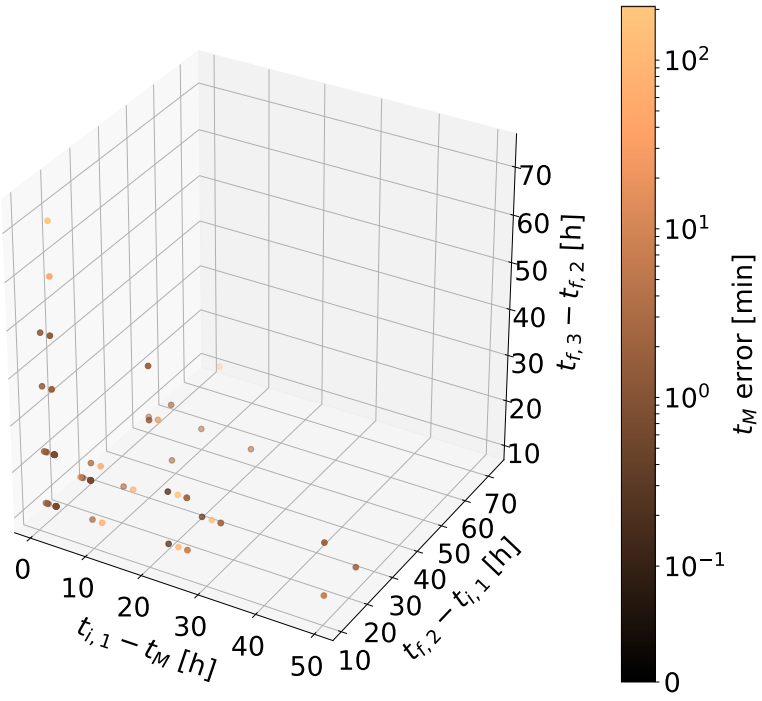

Figure 4.25: Variation of estimation error (*epoch*) for different associations of *3 tracks*.

5 | Conclusions and future work

A novel approach for manoeuvre detection and estimation, conceived to be employed in an operational scenario, has been developed and tested for a single LEO satellite. The final goal of this methodology is to increase the flexibility of the cataloguing chain and increase the robustness of the maintenance chain of an RSO catalogue. The detection strategy is based on metrics that rely on the residuals of observations, while the estimation algorithm, defined as a track-to-orbit correlation problem, is a two-step process which employs parameter estimation at first, to obtain an a-priori guess, and posterior high-fidelity orbit determination to refine the first estimate. The estimation algorithm requires the definition of a selection criterion to choose the most suitable guess among a set of different solutions. The proposed approach proved to be robust at detecting manoeuvres of the satellite and at providing reliable estimates, creating a link between an established pre-manoeuvre orbit and post-manoeuvre tracks.

Results were presented and discussed for both the detection and estimation methodology. The first one was able to detect all the true manoeuvres, while false manoeuvre triggering was only encountered after the estimation of long burns, evidencing the limitation of the manoeuvre estimation algorithm in these situations. It is important to remark that the processed data was simulated, so the detection strategy shall also be tested and eventually redefined when dealing with real observations (considering, as example, sensor tasking). The manoeuvre estimation algorithm was tested with the Keplerian + linear perturbations dynamical model, whose aim is to increase accuracy while keeping the computational cost extremely low, as required when using this approach in a multi-target situation for association purposes. The newly developed model is the major contribution of this work to the evolution of the methodology presented in [35]. The results of the two-step estimation process were presented. It was shown that the estimation algorithm, along with the selection criterion based on WRMS and on the control effort (adapted from the previous GEO analysis), can provide satisfactory results as the number of associated post-manoeuvre tracks increases. In this regard, it was proven that considering 3 or 4 tracks is a sound compromise between estimation quality and computational time; however, to have a safer margin, a manoeuvre is deemed to be confirmed only if estimated with 4

tracks in the simulation chain. Moreover, the impact of the second estimation step, based on the a-priori estimate, is able to increase the accuracy for both manoeuvre vector and epoch, validating the proposed approach.

Future developments will be devoted to the extension of the track-to-orbit manoeuvre detection and estimation to a wider multi-target association framework, in which the goal will be to associate multiple manoeuvrable RSOs with their post-manoeuvre tracks. This task is challenging due the dimension and scalability of the problem, determined by every single combination of UCTs and objects without recently correlated tracks to compare. This can be relieved by the preliminary track-to-track association step and by setting up a consistent methodology to discard most of unfeasible track-to-orbit correlations. In this regard, it is important to remark that the selection strategy to determine the best a-priori estimate, assuming optimal control in terms of manoeuvre magnitude, is tailored to this single-satellite scenario. In the multi-target association framework, the criterion will need to be adapted in order to consider more solutions and create a track-to-orbit association tree considering manoeuvres. The associations will be then evaluated and pruned through the analysis of more post-manoeuvre tracks, to finally associate each set observations to the correct manoeuvrable RSO. A possible strategy to achieve accurate correlations would be to include maximum thresholds on the WRMS of the residuals considering a manoeuvre, to discard very unlikely associations, and keeping only solutions which yield a manoeuvre size within typical sizes. In addition, heuristics can be introduced in the problem by considering the statistical characterisation of data regarding past manoeuvres and typical manoeuvre patterns, as done in [63], [67], [68] and [69]. The application of the manoeuvre detection and estimation strategy with multiple satellites will also be useful to confirm the results obtained in this thesis, as more data will need to be analysed.

The detection strategy can be augmented by different metrics such as the median values of the WRMS, and by defining more secondary thresholds to increase robustness. Regarding the estimation algorithm, improvements can be achieved by increasing the accuracy of the propagation while keeping a relatively low computational effort. This can be done by including $J2$ as a perturbation term or a simple model for aerodynamic drag, as well as employing semi-analytical propagators. Moreover, a methodology that could be applied is the one of Multi Fidelity propagation, which is a concept already presented in manoeuvre detection and estimation literature [86], using several models with different accuracy levels while keeping a modest computational cost. The problem of estimation of long burns could also be tackled, but it would eventually require a substantial reassessment of the methodology. The latter could also be considered only when refining the a-priori estimate with the high-fidelity orbit determination process.

Finally, the author would like to mention that this thesis has been developed as part of an internship in the Space Situational Awareness section of the Flight Dynamics Operations and Systems business unit at GMV. The work will also be presented as a conference paper at the 3rd IAA Conference on Space Situational Awareness (ICSSA) in Madrid, Spain, on April 4th - 6th 2022.

Bibliography

[1] Carolus Schrijver and George Siscoe. *Heliophysics: Evolving Solar Activity and the Climates of Space and Earth*. Cambridge University Press, 2010. DOI: 10.1017/CBO9780511760358.

[2] ESA Space Debris Office. *ESA's annual space environment report*. Tech. rep. GEN-DB-LOG-00288-OPS-SD. Darmstadt, Germany: ESA ESOC, May 2021.

[3] Jonathan C. McDowell. "The edge of space: Revisiting the Karman Line". In: *Acta Astronautica* 151 (2018), pp. 668–677. ISSN: 0094-5765. DOI: https://doi.org/10.1016/j.actaastro.2018.07.003. URL: https://www.sciencedirect.com/science/article/pii/S0094576518308221.

[4] N. Yu Ganushkina et al. "Locations of boundaries of outer and inner radiation belts as observed by Cluster and Double Star". In: *Journal of Geophysical Research: Space Physics* 116.A9 (2011). DOI: https://doi.org/10.1029/2010JA016376. eprint: https://agupubs.onlinelibrary.wiley.com/doi/pdf/10.1029/2010JA016376. URL: https://agupubs.onlinelibrary.wiley.com/doi/abs/10.1029/2010JA016376.

[5] European Space Operation Centre (ESOC). *DISCOSweb*. 2021. URL: https://discosweb.esoc.esa.int/ (visited on 10/21/2021).

[6] H. Klinkrad. *Space Debris: Models and Risk Analysis*. Astronautical Engineering. Springer, 2006. ISBN: 9783540254485. URL: https://books.google.es/books?id=EqD4h59KUXgC.

[7] Oliver Montenbruck and Eberhard Gill. *Satellite Orbits*. Vol. 1. Jan. 2000. ISBN: 978-3-540-67280-7. DOI: 10.1007/978-3-642-58351-3.

[8] Lloyd Wood. "Internetworking and Computing Over Satellite Networks". In: Apr. 2003. Chap. 2, pp. 13–34. ISBN: 1-4020-7424-7. DOI: 10.1007/978-1-4615-0431-3_2.

[9] IADC Steering Group and Working Group 4. *IADC Space Debris Mitigation Guidelines*. Tech. rep. IADC-02-01 rev. 2. Inter-Agency Space Debris Coordination Committee, Mar. 2020.

[10] Harry W. Jones. "The Recent Large Reduction in Space Launch Cost". In: *48th International Conference on Environmental Systems*. 2018.

[11] SpaceWorks. *Nano/Microsatellite Market Forecast 10th Edition (2020)*. Tech. rep. 2020.

[12] W Pang et al. "Boom of the CubeSat: a statistic survey of CubeSats launch in 2003-2015". In: *67th International Astronautical Congress*. Sept. 2016.

[13] Giacomo Curzi, Dario Modenini, and Paolo Tortora. "Large Constellations of Small Satellites: A Survey of Near Future Challenges and Missions". In: *Aerospace* 7.9 (2020). ISSN: 2226-4310. DOI: 10.3390/aerospace7090133. URL: https://www.mdpi.com/2226-4310/7/9/133.

[14] UN Office for Outer Space Affairs. *Online Index of Objects Launched into Outer Space*. https://www.unoosa.org/oosa/osoindex/index.jspx. 2021.

[15] Carsten Wiedemann et al. "Modeling of RORSAT NaK droplets for the MASTER 2005 upgrade". In: *Acta Astronautica* 57.2 (2005). Infinite Possibilities Global Realities, Selected Proceedings of the 55th International Astronautical Federation Congress, Vancouver, Canada, 4-8 October 2004, pp. 478–489. ISSN: 0094-5765. DOI: https://doi.org/10.1016/j.actaastro.2005.03.014. URL: https://www.sciencedirect.com/science/article/pii/S0094576505000834.

[16] NASA Space Debris Program Office. "Westford needles: where are they now?" In: *Orbital Debris Quarterly News* 17 (Oct. 2013), pp. 3–4.

[17] Masahiro Furumoto et al. "Environmental Estimation on Sub-millimeter-size Debris using In-situ Measurement Data". In: *7th European Conference on Space Debris* 7 (Apr. 2017). URL: https://conference.sdo.esoc.esa.int/proceedings/sdc7/paper/409/SDC7-paper409.pdf.

[18] Mike Gruntman. "Passive optical detection of submillimeter and millimeter size space debris in low Earth orbit". In: *Acta Astronautica* 105.1 (2014), pp. 156–170. ISSN: 0094-5765. DOI: https://doi.org/10.1016/j.actaastro.2014.08.022. URL: https://www.sciencedirect.com/science/article/pii/S0094576514003294.

[19] Technische Universität Braunschweig. *MASTER (Meteoroid And Space debris Terrestrial Environment Reference)*. 2021. URL: http://www.space-systems.eu/index.php/de/master (visited on 10/21/2021).

[20] Sven Flegel et al. "Modeling the space debris environment with MASTER-2009 and ORDEM-2010". In: *60th International Astronautical Congress*. Jan. 2010.

[21] André Horstmann, Holger Krag, and Enrico Stoll. "Providing Flux Uncertainties in ESA-MASTER: The Accuracy of the 1cm Population". In: *First International Orbital Debris Conference*. 2019.

[22] Juan Luis Gonzalo, Camilla Colombo, and Pierluigi Di Lizia. "Introducing MISS, a new tool for collision avoidance analysis and design". In: *Journal of Space Safety Engineering* 7.3 (Oct. 2020). ISSN: 2468-8967. DOI: 10.1016/j.jsse.2020.07.010. URL: http://dx.doi.org/10.1016/j.jsse.2020.07.010.

[23] Maria Francesca Palermo et al. "Numerically efficient methods for low-thrust collision avoidance maneuver design". In: *8th European Conference on Space Debris*. Apr. 2021. URL: https://conference.sdo.esoc.esa.int/proceedings/sdc8/paper/282.

[24] Roberto Armellin. "Collision avoidance maneuver optimization with a multiple-impulse convex formulation". In: *Acta Astronautica* 186 (June 2021), pp. 347–362. ISSN: 0094-5765. DOI: 10.1016/j.actaastro.2021.05.046. URL: http://dx.doi.org/10.1016/j.actaastro.2021.05.046.

[25] Donald J. Kessler and Burton G. Cour-Palais. "Collision frequency of artificial satellites: The creation of a debris belt". In: *Journal of Geophysical Research: Space Physics* 83.A6 (1978). DOI: https://doi.org/10.1029/JA083iA06p02637. eprint: https://agupubs.onlinelibrary.wiley.com/doi/pdf/10.1029/JA083iA06p02637. URL: https://agupubs.onlinelibrary.wiley.com/doi/abs/10.1029/JA083iA06p02637.

[26] J.C. Liou and N. L. Johnson. "Risks in Space from Orbiting Debris". In: *Science* 311.5759 (2006), pp. 340–341. DOI: 10.1126/science.1121337. eprint: https://www.science.org/doi/pdf/10.1126/science.1121337. URL: https://www.science.org/doi/abs/10.1126/science.1121337.

[27] B Bastida Virgili and Holger Krag. "Analyzing the criteria for a stable environment". In: *AAS/AIAA Astrodynamics Specialist Conference, Girdwood, AK, USA. AAS11*. Vol. 411. 2011.

[28] Kjetil Wormnes et al. "ESA technologies for space debris remediation". In: *6th European Conference on Space Debris*. Vol. 1. ESA Communications ESTEC Noordwijk, The Netherlands. 2013, pp. 1–8.

[29] Benjamin Bastida Virgili. "DELTA (Debris Environment Long-Term Analysis)". In: *6th International Conference on Astrodynamics Tools and Techniques*. 2016.

[30] Tim Flohrer and Holger Krag. "Space Surveillance and Tracking in ESA's SSA programme". In: *7th European Conference on Space Debris* 7 (Apr. 2017). URL: https://conference.sdo.esoc.esa.int/proceedings/sdc7/paper/242/SDC7-paper242.pdf.

[31] Giacomo Tommei, A. Milani, and Alessandro Rossi. "Orbit determination of space debris: Admissible regions". In: *Celestial Mechanics and Dynamical Astronomy* 97 (Apr. 2007). DOI: 10.1007/s10569-007-9065-x.

[32] 18th Space Control Squadron. *Map of SSN sensors and centres locations*. 2018. URL: https://twitter.com/18SPCS/status/963629809921351680 (visited on 11/04/2021).

[33] European Union SST. *Map of EU SST sensors locations*. 2021. URL: https://www.eusst.eu/about-us/ (visited on 11/04/2021).

[34] Alejandro Pastor et al. "Correlation techniques to build-up and maintain space objects catalogues". In: (Nov. 2019).

[35] A. Pastor et al. "Satellite maneuver detection and estimation with optical survey observations". In: *The Journal of the Astronautical Sciences* (2021). DOI: 10.1007/s40295-022-00311-5.

[36] A. Milani et al. "Orbit determination with very short arcs. I - Admissible regions". In: *Celestial Mechanics and Dynamical Astronomy* 90 (July 2004), pp. 57–85. DOI: 10.1007/s10569-004-6593-5.

[37] Laura Pirovano, Gennaro Principe, and Roberto Armellin. "Data association and uncertainty pruning for tracks determined on short arcs". In: *Celestial Mechanics and Dynamical Astronomy* 132.1 (Jan. 2020), p. 6. ISSN: 1572-9478. DOI: 10.1007/s10569-019-9947-8. URL: https://doi.org/10.1007/s10569-019-9947-8.

[38] The Consultative Committee for Space Data Systems. *Conjunction Data Message (CCSDS 508.0-B-1)*. 2013.

[39] Corinne Contant-Jorgenson, Petr Lála, and Kai-Uwe Schrogl. "The IAA Cosmic Study on space traffic management". In: *Space Policy* 22.4 (2006), pp. 283–288. ISSN: 0265-9646. DOI: https://doi.org/10.1016/j.spacepol.2006.08.004. URL: https://www.sciencedirect.com/science/article/pii/S0265964606000774.

[40] Wikisource. *Moon Treaty — Wikisource*. [Online; accessed 20-October-2021]. 2016. URL: https://en.wikisource.org/w/index.php?title=Moon_Treaty&oldid=6260729.

[41] Wikisource. *Partial Test Ban Treaty — Wikisource*. [Online; accessed 20-October-2021]. 2013. URL: https://en.wikisource.org/w/index.php?title=Partial_Test_Ban_Treaty&oldid=4226359.

[42] COPUOS. *Space Debris Mitigations Guidelines of the Committee on the Peaceful Uses of Outer Space*. Tech. rep. ST/SPACE/49. Wien, Austria: UN Office for Outer Space Affairs, 2010.

[43] COPUOS. *Guidelines for the Long-term Sustainability of Outer Space Activities of the Committee on the Peaceful Uses of Outer Space*. Tech. rep. ST/SPACE/79. Wien, Austria: UN Office for Outer Space Affairs, June 2021.

[44] Radiocommunication Sector. *Environmental protection of the geostationary-satellite orbit*. Tech. rep. ITU-R S.1003-2. Geneva, Switzerland: ITU, 2011.

[45] European Commission. *EUSTM*. 2021. URL: https://eustm.eu/ (visited on 10/20/2021).

[46] European Commission. *Spaceways*. 2021. URL: https://spaceways-h2020.eu/ (visited on 10/20/2021).

[47] 18th Space Control Squadron. *SpaceTrack*. URL: www.space-track.org (visited on 10/20/2021).

[48] T.S. Kelso. *Celestrak*. URL: https://celestrak.com/ (visited on 10/20/2021).

[49] F. R. Hoots and R. L. Roehrich. *Spacetrack Report No. 3: Models for propagation of NORAD element sets*. Tech. rep. Aerospace Defense Center, Peterson Air Force Base, 1980.

[50] David Vallado and Paul Cefola. "Two-line element sets - Practice and use". In: *Proceedings of the International Astronautical Congress, IAC* 7 (Jan. 2012), pp. 5812–5825.

[51] 18th Space Control Squadron. *Spaceflght safety handbook for satellite operators*. Tech. rep. Version 1.5. Vandenberg Air Force Base, USA: Combined Force Space Component Command (CFSCC), Aug. 2020.

[52] JSC Vimpel. *JSC Vimpel - data portal*. 2021. URL: http://spacedata.vimpel.ru/ (visited on 10/21/2021).

[53] Alejandro Pastor et al. "Data processing methods for catalogue build-up and maintenance". In: *1st NEO and Debris Detection Conference* (2019).

[54] Y. Bar-Shalom. "On the track-to-track correlation problem". In: *IEEE Transactions on Automatic Control* 26.2 (1981). DOI: 10.1109/TAC.1981.1102635.

[55] A. Pastor, M. Sanjurjo-Rivo, and D. Escobar. "Track-to-track association methodology for operational surveillance scenarios with radar observations". In: *CEAS Space Journal* (2022).

[56] Jan Siminski et al. "Short-arc tracklet association for geostationary objects". In: *Advances in Space Research* 53 (2014), pp. 1184–1194.

[57] Benedikt Reihs, Alessandro Vananti, and Thomas Schildknecht. "Tracklet-based correlation of combined radar and optical measurements". In: *1st NEO and Debris Detection Conference*. Jan. 2019.

[58] Raúl Domínguez-González et al. "Cataloguing space objects from observations: CORTO cataloguing system". In: *7th European Conference on Space Debris*. Apr. 2017.

[59] Jacob Decoto and Patrick Loerch. "Technique for GEO RSO station keeping characterization and maneuver detection". In: *Proceedings of the Advanced Maui Optical and Space Surveillance Technologies Conference,(AMOS)*. 2015.

[60] Brian Lee Kantsiper. "A systematic approach to station-keeping of constellations of satellites". PhD thesis. Massachusetts Institute of Technology, 1998.

[61] Marcus Holzinger, D. Scheeres, and Kyle Alfriend. "Object Correlation, Maneuver Detection, and Characterization Using Control Distance Metrics". In: *Journal of Guidance, Control, and Dynamics* 35 (July 2012), pp. 1312–1325. DOI: 10.2514/1.53245.

[62] Andris D Jaunzemis, Midhun V Mathew, and Marcus J Holzinger. "Control cost and Mahalanobis distance binary hypothesis testing for spacecraft maneuver detection". In: *Journal of Guidance, Control, and Dynamics* 39.9 (2016), pp. 2058–2072.

[63] Jan Siminski, Hauke Fiedler, and Tim Flohrer. "Correlation of Observations and Orbit Recovery Considering Maneuvers". In: *AAS/AIAA Space Flight Mechanics*. Feb. 2017.

[64] Romain Serra, Carlos Yanez, and Carolin Frueh. "Tracklet-to-orbit association for maneuvering space objects using optimal control theory". In: *Acta Astronautica* 181 (2021), pp. 271–281. ISSN: 0094-5765. DOI: https://doi.org/10.1016/j.actaastro.2021.01.026. URL: https://www.sciencedirect.com/science/article/pii/S0094576521000291.

[65] Atri Dutta and Joseph Raquepas. "Stochastic Optimization Framework for Spacecraft Maneuver Detection". In: *AIAA Scitech 2020 Forum*. 2020, p. 0234.

[66] K Hill. "Maneuver detection and estimation with optical tracklets". In: *Advanced Maui Optical and Space Surveillance Technologies Conference*. 2014, E26.

[67] Jan Siminski, Tim Flohrer, and Thomas Schildknecht. "Assessment of post-maneuver observation correlation using short-arc tracklets". In: *7th European Conference on Space Debris*. 2017.

[68] Guillermo Escribano et al. "Maneuver detection via combined heuristical and statistical methodologies". In: *8th European Conference on Space Debris*. 2021.

[69] Guillermo Escribano et al. "Automatic maneuver detection and tracking of space objects in optical survey scenarios based on stochastic hybrid systems formulation". In: *arXiv preprint arXiv:2109.07801* (2021).

[70] Gregory Mcintyre and Kenneth Hintz. "Comparison of several maneuvering target tracking models". In: *Proceedings of SPIE - The International Society for Optical Engineering* 3374 (July 1998). DOI: 10.1117/12.327127.

[71] Rafael Vazquez et al. "Manoeuvre detection for near-orbiting objects". In: *8th European Conference on Space Debris*. 2021.

[72] James Woodburn, John Carrico, and James R Wright. "Estimation of Instantaneous Maneuvers Using a Fixed Interval Smoother". In: *Advances in the Astronautical Sciences* 116 (2003), pp. 243–260.

[73] Zhao Li, Yidi Wang, and Wei Zheng. "Ranging-Measurements-Based Maneuver Detection Method for Space Target Tracking". In: *Journal of Physics: Conference Series* 1828 (Feb. 2021), p. 012096. DOI: 10.1088/1742-6596/1828/1/012096.

[74] Tom Kelecy and Moriba Jah. "Detection and orbit determination of a satellite executing low thrust maneuvers". In: *Acta Astronautica* 66.5-6 (2010), pp. 798–809.

[75] Richard S Hujsak, James W Woodburn, and John H Seago. "The orbit determination tool kit (ODTK)–version 5". In: *Paper AAS* (2007), pp. 07–125.

[76] Jian Huang, Weidong Hu, and Lefeng Zhang. "Maneuver detection of space object for space surveillance". In: *6th European Conference on Space Debris*. 2013.

[77] Christoph Michael Bergmann et al. "Integrated Manoeuvre Detection and Estimation Using Nonlinear Kalman Filters During Orbit Determination of Satellites". In: *Proceedings of the 8th European Conference on Space Debris*. 2021.

[78] Johannes Herzog, Hauke Fiedler, and Thomas Schildknecht. "Using Conjunctuion Analysis Methods for Manoeuvre Detection". In: *7th European Conference on Space Debris*. 2017.

[79] X. Rong Li and V.P. Jilkov. "Survey of maneuvering target tracking. Part V. Multiple-model methods". In: *IEEE Transactions on Aerospace and Electronic Systems* 41.4 (2005), pp. 1255–1321. DOI: 10.1109/TAES.2005.1561886.

[80] National Research Council. *Continuing Kepler's Quest: Assessing Air Force Space Command's Astrodynamics Standards*. Washington, DC: The National Academies Press, 2012. ISBN: 978-0-309-26142-5. DOI: 10.17226/13456. URL: https://www.nap.edu/catalog/13456/continuing-keplers-quest-assessing-air-force-space-commands-astrodynamics-standards.

[81] Hyun Chul Ko and Daniel J Scheeres. "Orbit Determination and Maneuver Detection Using Event Representation with Thrust-Fourier-Coefficients". In: *Proceedings of the Advanced Maui Optical and Space Surveillance Technologies Conference*. 2015.

[82] Zhai Guang et al. "Non-cooperative maneuvering spacecraft tracking via a variable structure estimator". In: *Aerospace Science and Technology* 79 (2018), pp. 352–363. ISSN: 1270-9638. DOI: https://doi.org/10.1016/j.ast.2018.05.052. URL: https://www.sciencedirect.com/science/article/pii/S1270963818300452.

[83] Liu Ye et al. "Maneuver detection and tracking of a space target based on a joint filter model". In: *Asian Journal of Control* 23.3 (2021), pp. 1441–1453. DOI: https://doi.org/10.1002/asjc.2297. eprint: https://onlinelibrary.wiley.com/doi/pdf/10.1002/asjc.2297. URL: https://onlinelibrary.wiley.com/doi/abs/10.1002/asjc.2297.

[84] Quang M Lam. "Resident space object tracking using an interacting multiple model mixing scheme". In: *Sensors and Systems for Space Applications VII*. Vol. 9085. International Society for Optics and Photonics. 2014, p. 90850V.

[85] Bin Jia et al. "Space object tracking and maneuver detection via interacting multiple model cubature Kalman filters". In: *2015 IEEE Aerospace conference*. IEEE. 2015, pp. 1–8.

[86] Enrico M Zucchelli, Zachary R McLaughlin, and Brandon A Jones. "Tracking Maneuvering Targets with Multi-Fidelity Interacting Multiple Model Filters". In: (2020).

[87] Gary M. Goff, Jonathan T. Black, and Joseph A. Beck. "Tracking maneuvering spacecraft with filter-through approaches using interacting multiple models". In: *Acta Astronautica* 114 (2015), pp. 152–163. ISSN: 0094-5765. DOI: https://doi.org/10.1016/j.actaastro.2015.05.009. URL: https://www.sciencedirect.com/science/article/pii/S0094576515001903.

[88] Gary M Goff et al. "Parameter requirements for noncooperative satellite maneuver reconstruction using adaptive filters". In: *Journal of Guidance, Control, and Dynamics* 38.3 (2015), pp. 361–374.

[89] Daniel P Lubey. "Maneuver Detection and Reconstruction in Data Sparse Systems with an Optimal Control Based Estimator". PhD thesis. University of Colorado at Boulder, 2015.

[90] Jesse A Greaves and Daniel J Scheeres. "Observation and Maneuver Detection for Cislunar Vehicles". In: *The Journal of the Astronautical Sciences* (2021), pp. 1–29.

[91] Nicholas Ravago and Brandon A. Jones. "Space Object Manoeuvre Detection in a Multi-Target Environment Using a Labeled Multi-Bernoulli Filter". In: *Proceedings of the 1st IAA Conference on Space Situational Awareness (ICSSA)*. 2018.

[92] Ba Tuong Vo. "Random finite sets in multi-object filtering". PhD thesis. University of Western Australia, 2008.

[93] Keric Hill, Chris Sabol, and Kyle T Alfriend. "Comparison of covariance based track association approaches using simulated radar data". In: *The Journal of the Astronautical Sciences* 59.1 (2012), pp. 281–300.

[94] ESA Copernicus. *Sentinel Online - Sentinel 3-A Orbit Description*. URL: https://sentinels.copernicus.eu/web/sentinel/missions/sentinel-3/satellite-description/orbit (visited on 01/03/2022).

[95] ESA Copernicus. *Sentinel Online - Sentinel 3-A Satellite Parameters for POD*. URL: https://sentinels.copernicus.eu/web/sentinel/technical-guides/sentinel-3-altimetry/pod/satellite-parameters (visited on 01/03/2022).

[96] PK Seidelmann and J Kovalevsky. "Application of the new concepts and definitions (ICRS, CIP and CEO) in fundamental astronomy". In: *Astronomy & Astrophysics* 392.1 (2002), pp. 341–351.

[97] Zuheir Altamimi, Xavier Collilieux, and Laurent Métivier. "ITRF2008: an improved solution of the international terrestrial reference frame". In: *Journal of Geodesy* 85.8 (2011), pp. 457–473.

A | Appendix A

The following appendix briefly introduces some physical concepts, supported by their mathematical expressions, which are useful for the development of the manoeuvre detection and estimation methodology. Appendix A.1 presents typical reference coordinate systems used for the description of satellite orbits, as well as the transformations between them. Appendix A.2 provides a set of equations which relate the state vector of an orbiting object to the quantities which are usually sensed by SST instruments, in order to build up an analytical model for measurements simulation.

A.1. Coordinate systems

The reference equatorial Earth-centred inertial (ECI) frame which is used throughout the dissertation is the **Geocentric Celestial Reference Frame** (GCRF), that is the realisation of the Geocentric Celestial Refence System (GCRS) defined by the International Astronomical Union (IAU) in 2000. This system is derived from the **International Celestial Reference System** (ICRS, still defined by IAU in the very same year) and from its subsequent realisation, the International Celestial Reference Frame (ICRF), determined by the observation of far-away celestial bodies at radio wavelengths [96]. The ICRS is a space-fixed coordinate system having origin in the barycentre of the Solar System. The GCRS is instead centred in the Earth. The conversion between these two systems, along with the translation of the origin, accounts for relativistic effects generated by Earth's mass and its rotation (known as Sitter precession and Lense-Thirring precession respectively). Position vectors in these systems (and, in general, in any ECI system) can be expressed through their Cartesian coordinates $\mathbf{r}_{GCRF}$, or equivalently via their distance from the origin R, right ascension $\alpha \in [0, 2\pi)$ and declination $\delta \in [-\pi/2, +\pi/2]$. The conversion from range and angular coordinates to Cartesian coordinates can be performed as follows:

$$\mathbf{r}_{GCRF} = R \cdot [\cos\delta\cos\alpha,\ \cos\delta\sin\alpha,\ \sin\delta]^T \tag{A.1}$$

Figure A.1 presents a graphical representation of the GCRS frame (or, more in general, of any ECI). The figure shows the coordinates R, α and δ of a point on the celestial sphere. The first axis of the frame is parallel to the direction of the vernal equinox γ and the third one points towards the Celestial North Pole; the last axis completes the right-handed coordinate system.

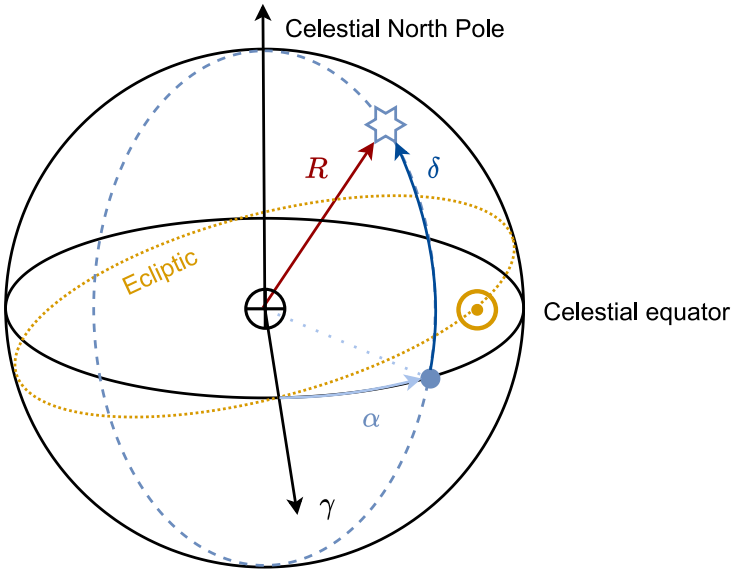

Figure A.1: Representation of GRCS coordinate system.

Along with the GCRS, there is need to define an Earth-fixed coordinate system, which means a coordinate system that remains fixed to the Earth as the latter rotates in space. The selected one is the **International Terrestrial Reference System** (ITRS), defined and constantly updated by International Earth Rotation and Reference Systems Services (IERS) [97]. This system has origin in Earth's centre and takes into account the effects of precession, nutation, rotation and pole motion through some models describing their dynamics. Its realisation, known as International Terrestrial Reference Frame (ITRF) is carried out by using accurate SLR, Lunar Laser Ranging (LLR) and Very Long Baseline Interferometry (VLBI) measurements. The first axis of the ITRS is aligned with the Greenwich meridian, the third one in the direction of the terrestrial North Pole, and the last one completes the right-handed coordinate system. Transformation from ICRF (as well as GCRF) to ITRF is made possible by the Earth Observation Parameters (EOP). These are sets of parameters which describe the relative orientation of the two frames (taking into account the aforementioned irregularities of Earth's rotational dynamics) as a function of time. The EOP are published in daily, monthly or yearly bulletins compiled by IERS. In general, the transformation of a Cartesian vector from GCRF to IRTF can be performed through the following equation [7]:

$$\begin{aligned} \mathbf{r}_{ITRF} &= [\Pi(t)\,\Theta(t)\,N(t)\,P(t)] \cdot \mathbf{r}_{GCRF} \\ &= U(t) \cdot \mathbf{r}_{GCRF} \end{aligned} \tag{A.2}$$

The four matrices which pre-multiply $\mathbf{r}_{GCRS}$ are all rotation matrices, thus are orthogonal. They are respectively: $\Pi(t)$ for polar motion, $\Theta(t)$ for rotation, $N(t)$ for nutation and $P(t)$ for precession.

Consider now an observer, or a ground station, located on Earth's surface. An intuitive system which has origin in this point is the **topocentric-horizon** coordinate system. This frame is Earth-fixed and is aligned with the local horizontal plane, which is the plane tangential to the Earth's surface at that given point. The three reference axes employed in this frame are $\mathbf{e}_E$, pointing East, $\mathbf{e}_N$, pointing North, and $\mathbf{e}_Z$, parallel to the local zenith direction. The first two vectors are parallel respectively to the local meridian and parallel of latitude passing through the observer. The position of the observer can be related to an Earth-fixed Earth-centred frame via its geodetic longitude λ, its geodetic latitude ϕ, which is the angle between the Equator and the normal to the local tangent plane, and its geodetic height h. Longitude is computed with respect to the Greenwich meridian and positive towards East, while latitude is referred to the equatorial plane and positive towards North. Considering as the Earth as an ellipsoid with oblateness f (defined by the relative difference of the equatorial radius $R_\oplus$ and the polar radius R_p, such that $f = (R_\oplus - R_p)/R_\oplus$), the position vector of the station in an Earth-fixed Earth-centred frame $\mathbf{s}_{ef}$ can written as:

$$\mathbf{s}_{ef} = \begin{bmatrix} (N+h)\cos\phi\cos\lambda \\ (N+h)\cos\phi\sin\lambda \\ [(1-f)^2 N + h]\sin\phi \end{bmatrix} \tag{A.3}$$

where:

$$N = \frac{R_\oplus}{\sqrt{1 - f(2-f)\sin^2\phi}} \tag{A.4}$$

More precise computation of the ground station position should require modelling of the local displacements due to tidal perturbations (solid, lunar and polar), as well as plate motion. The transformation from the topocentric horizon frame to an Earth-fixed Earth-centred frame can be defined by the matrix E, composed by the unitary vectors which represent the orientation of the topocentric horizon axes [7].

$$E = \begin{bmatrix} \hat{\mathbf{e}}_E^T \\ \hat{\mathbf{e}}_N^T \\ \hat{\mathbf{e}}_Z^T \end{bmatrix} = \begin{bmatrix} -\sin\lambda & +\cos\lambda & 0 \\ -\sin\phi\cos\lambda & -\sin\phi\sin\lambda & +\cos\phi \\ +\cos\phi\cos\lambda & +\cos\phi\sin\lambda & +\sin\phi \end{bmatrix} \tag{A.5}$$

Figure A.2 provides a graphical representation of the topocentric frame and its orientation with respect to an Earth-fixed frame.

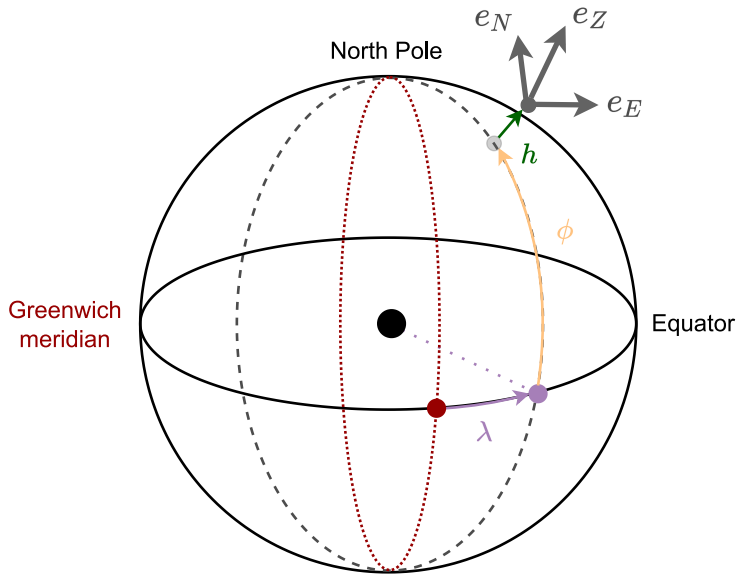

Figure A.2: Representation of the topocentric horizon coordinate system.

The position of a point in space expressed in the topocentric-horizon frame is usually defined by its range ρ, which is the distance from the point to the origin of the frame, and by two angular coordinates, the azimuth $A \in [0, 2\pi)$ and elevation $E \in [-\pi/2, \pi/2]$. The azimuth is the angle between the direction of North and the projection of the point onto the tangential plane, measured positive in the clockwise direction. The elevation is instead the angular distance between the point and the local horizon. The Cartesian position vector can be retrieved from these coordinates as:

$$\mathbf{r}_{th} = \rho \cdot [\cos E \sin A,\ \cos E \cos A,\ \sin E]^T \tag{A.6}$$

Figure A.3 shows the coordinates of a point in the topocentric-horizon coordinate system.

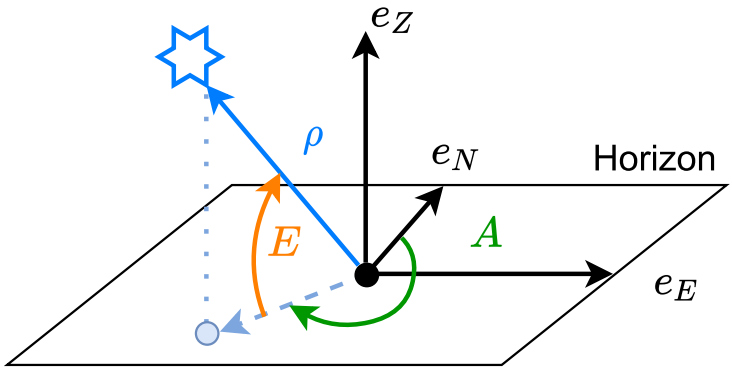

Figure A.3: Coordinates of a point in topocentric horizon coordinate system.

A.2. Analytical model for measurements simulation and prediction

As stated in Chapter 1, typical ground sensors employed in SST activities provide angular measurements as well as range measurements in case of ranging sensors (radars and SLRs), while range-rate measurements are limited to radars only. Telescopes usually supply angular measurements in an inertial frame (right ascension and declination), while radars and SLRs in a local frame (by means of azimuth and elevation). The goal of this section is to define a model, based on the coordinate systems presented in Appendix A.1, to retrieve the nominal coordinates which can be sensed by SST instruments, along with their partial derivatives. The development of this model is required for the manoeuvre estimation algorithm (which needs the computation of residuals) and is employed for the generation of simulated measurements. The equations can be employed for any type of sensor which is able to provide range, range-rate and angular measurements; they can also be applied in cases for which the angular coordinates are provided in a local frame (azimuth and elevation) via transformations of coordinate systems.

Knowing the geodetic coordinates of a ground station, its position in the GCRF frame can be computed as:

$$\mathbf{s}_{sf}(t) = U^T(t) \cdot \mathbf{s}_{ef} = U^T(t) \cdot \begin{bmatrix} (N+h)\cos\phi\cos\lambda \\ (N+h)\cos\phi\sin\lambda \\ [(1-f)^2 N + h]\sin\phi \end{bmatrix} \tag{A.7}$$

The subscript $(\cdot)_{sf}$ refers to a Earth-centred space-fixed coordinate system (GCRF in this case), while $(\cdot)_{ef}$ refers to an Earth-centred Earth-fixed system (ITRF in this case). Consider now the Cartesian state vector representing the position and velocity of a satellite

in the GCRF frame $\mathbf{X}_{sf} = \left[\mathbf{R}_{sf}(t),\, \dot{\mathbf{R}}_{sf}(t)\right]^T$. The relative position of the satellite with respect to the station can be simply derived as $\mathbf{r}_{sf}(t) = \mathbf{R}_{sf}(t) - \mathbf{s}_{sf}(t)$, as well as its velocity $\dot{\mathbf{r}}_{sf}(t) = \dot{\mathbf{R}}_{sf}(t) - \dot{\mathbf{s}}_{sf}(t)$. The two vectors can be gathered in the state $\mathbf{x}_{sf}(t) = [\mathbf{r}_{sf}(t), \dot{\mathbf{r}}_{sf}(t)]^T$. Considering the latter and applying spherical geometry, it is possible to compute the range ρ, range-rate $\dot{\rho}$, right-ascension α_t and declination δ_t. The angular quantities have the $(\cdot)_t$ subscript as they are topocentric quantities: they are related to a reference frame which has origin in the ground station, but axes parallel to the GCRF.

$$\begin{cases} \rho = \sqrt{\mathbf{r}_{sf} \cdot \mathbf{r}_{sf}} \\ \dot{\rho} = \dot{\mathbf{r}}_{sf} \cdot \dfrac{\mathbf{r}_{sf}}{\rho} \\ \delta_t = \arcsin\left(r_y/\rho\right) \\ \alpha_t = \begin{cases} \arccos\left(r_x/(\rho \cdot \cos\delta_t)\right), & \text{if } r_y/\rho > 0 \\ 2\pi - \arccos\left(r_x/(\rho \cdot \cos\delta_t)\right), & \text{if } r_y/\rho \leqslant 0 \end{cases} \end{cases} \tag{A.8}$$

The terms $[r_x,\, r_y,\, r_z]$ the components of the position vector $\mathbf{r}_{sf}$. The computation of α_t can be replaced by the function `atan2`, such that $\alpha_t = \texttt{atan2}\,(r_y, r_x)$, if carried out in scientific computing environments. The partial derivatives of the range with respect to the state vector $\mathbf{x}_{sf}$ can be computed as:

$$\frac{\partial \rho}{\partial \mathbf{X}_{sf}} = \frac{1}{\rho}\begin{bmatrix} r_x & r_y & r_z & 0 & 0 & 0 \end{bmatrix} \tag{A.9}$$

For range rate instead:

$$\frac{\partial \dot{\rho}}{\partial \mathbf{X}_{sf}} = \frac{1}{\rho}\begin{bmatrix} \dot{r}_x - \dot{\rho}\cdot r_x/\rho & \dot{r}_y - \dot{\rho}\cdot r_y/\rho & \dot{r}_z - \dot{\rho}\cdot r_z/\rho & r_x & r_y & r_z \end{bmatrix} \tag{A.10}$$

The derivatives of range with respect to velocity $\dot{\mathbf{R}}_{sf}$ are null since there is no direct dependence. The partial derivatives of right ascension α_t and declination δ_t can be derived from trigonometric relations (based on Equation (A.1)) and have the following form:

$$\frac{\partial \alpha_t}{\partial \mathbf{X}_{sf}} = \frac{1}{r_x^2 + r_y^2}\begin{bmatrix} -r_y & +r_x & 0 & 0 & 0 & 0 \end{bmatrix} \tag{A.11}$$

$$\frac{\partial \delta_t}{\partial \mathbf{X}_{sf}} = \frac{1}{\rho^2 \cdot \sqrt{r_x^2 + r_y^2}}\begin{bmatrix} -r_x & +r_z & r_x^2 + r_y^2 & 0 & 0 & 0 \end{bmatrix} \tag{A.12}$$

Also for angular measurements derivatives with respect to $\dot{\mathbf{R}}_{sf}$ are equal to zero. Finally, the ensemble of equations in Equation (A.8) can be reformulated as a vector function:

$$\mathbf{h}\left(t,\, \mathbf{X}_{sf}(t)\right) \tag{A.13}$$

as well as its derivatives:

$$\frac{\partial \mathbf{h}\left(t,\, \mathbf{X}_{sf}(t)\right)}{\partial \mathbf{X}_{sf}} \tag{A.14}$$

The time dependence, even if it is indirect (as it is included in $\mathbf{X}_{sf}(t)$), is made explicit for sake of clarity, as the model will be employed for different times at which observations are taken. Finally, it is important to remark that this model provides nominal quantities as uncertainties are not included in these calculations; however, the latter will be included as typical Gaussian measurement noise in the parameter estimation and OD processes.

B | Appendix B

Burn epoch	Duration	Manoeuvre vector (RIC frame) $[m/s]$
23/02/2017 09:40:17	1.75 s	$[-0.00003, 0.00402, 0.00124]^T$
15/03/2017 07:42:21	12 min 34.45 s	$[-0.00606, 0.01101, 2.14067]^T$
27/04/2017 10:57:53	12.75 s	$[-0.00010, 0.00812, 0.00012]^T$
23/05/2017 14:34:59	0.38 s	$[0.00009, -0.00130, 0.00014]^T$
12/07/2017 09:44:24	2.37 s	$[-0.00011, 0.00559, 0.00082]^T$
06/09/2017 10:26:03	13 min 27.11 s	$[-0.00774, 0.01418, 2.08535]^T$
27/09/2017 08:07:40	1.87 s	$[-0.00009, 0.00433, 0.00062]^T$
29/11/2017 09:20:01	2.35 s	$[-0.00005, 0.00517, 0.00031]^T$
13/12/2017 08:08:41	11 min 15.73 s	$[-0.00575, 0.01218, 1.85953]^T$
28/02/2018 10:04:59	1.00 s	$[0.00015, -0.00322, -0.00072]^T$
14/03/2018 08:45:30	12 min 59.11 s	$[-0.00536, 0.01583, 2.10507]^T$
24/05/2018 08:11:50	3.25 s	$[-0.00004, 0.00683, -0.00003]^T$
01/08/2018 08:14:59	1.50 s	$[-0.00023, 0.00335, 0.00098]^T$
29/08/2018 07:47:51	13 min 24.87 s	$[-0.00475, 0.01286, 2.17017]^T$
28/11/2018 13:44:59	0.87 s	$[-0.00020, 0.00197, 0.00038]^T$
19/12/2018 09:31:11	12 min 5.75 s	$[-0.00492, 0.01286, 1.89920]^T$
27/02/2019 09:14:59	1.00 s	$[0.00019, -0.00306, 0.00002]^T$
13/03/2019 08:07:43	13 min 48.98 s	$[-0.00497, 0.01510, 2.16371]^T$
13/06/2019 08:22:59	2.62 s	$[-0.00015, 0.00568, 0.00027]^T$
28/08/2019 12:12:11	12 min 18.93 s	$[-0.00384, 0.01205, 1.91230]^T$
27/11/2019 08:04:59	1.50 s	$[-0.00008, 0.00322, -0.00002]^T$
11/12/2019 11:56:51	14 min 8.92 s	$[-0.00418, 0.01129, 2.18477]^T$

Table B.1: Manoeuvre history of Sentinel 3-A in years 2017 to 2019 [95].

List of Figures

1.1 Distribution of RSOs according to their orbital regime in DISCOS (up to mid October 2021). 2
1.2 Number of launches per year according to DISCOS (up to mid October 2021). 4
1.3 Number of fragmentation per year according to DISCOS (up to mid October 2021). 5
1.4 Distribution of RSOs according to their nature/source in DISCOS (up to mid October 2021). 6
1.5 Location of the SSN sensors and facilities. Credits 18$^{\text{th}}$ SPCS [32]. 10
1.6 Map of the EUSST sensors network. Credits EUSST [33]. 11
1.7 Catalogue maintenance accounting for manoeuvres. 20

3.1 Manoeuvre detection scheme. 37
3.2 Graphical representation of the manoeuvre estimation method. 38

4.1 Test for propagation accuracy of the two dynamical models (*radial burns*). 53
4.2 Test for propagation accuracy of the two dynamical models (*in-track burns*). 54
4.3 Test for propagation accuracy of the two dynamical models (*cross-track burns*). 55
4.4 Distribution of the true manoeuvres according of the arrival times of the 1$^{\text{st}}$ and 4$^{\text{th}}$ track. 58
4.5 Graphical representation of the simulation scenario. 60
4.6 Confusion matrix for manoeuvre detection. 62
4.7 Distribution of manoeuvre estimates (left) with estimation algorithm and high-fidelity orbit determination (right) (*1 track*). 65
4.8 Distribution of manoeuvre estimates (left) with estimation algorithm and high-fidelity orbit determination (right) (*2 tracks*). 65
4.9 Distribution of manoeuvre estimates (left) with estimation algorithm and high-fidelity orbit determination (right) (*3 tracks*). 66

4.10 Distribution of manoeuvre estimates (left) with estimation algorithm and high-fidelity orbit determination (right) (*4 tracks*). 66
4.11 Distribution of the estimated manoeuvre components error (*1 track*). . . . 67
4.12 Distribution of the estimated manoeuvre components error (*2 tracks*). . . . 68
4.13 Distribution of the estimated manoeuvre components error (*3 tracks*). . . . 68
4.14 Distribution of the estimated manoeuvre components error (*4 tracks*). . . . 69
4.15 Differences in orbital elements of pre and post-manoeuvre orbit (manoeuvre on 12/07/17). 70
4.16 Initial estimation of manoeuvre on 12/07/2017 with tracks {1}. 71
4.17 Initial estimation of manoeuvre on 12/07/2017 with tracks {1, 2}. 72
4.18 Initial estimation of manoeuvre on 12/07/2017 with tracks {1, 2, 3}. 73
4.19 Initial estimation of manoeuvre on 12/07/2017 with tracks {1, 2, 3, 4}. . . 73
4.20 Differences in orbital elements of pre and post-manoeuvre orbit (manoeuvre on 06/09/17). 75
4.21 Initial estimation of manoeuvre on 06/09/2017 with tracks {5, 6, 7}. 76
4.22 Initial estimation of manoeuvre on 06/09/2017 with tracks {5, 6, 7, 8}. . . 76
4.23 Variation of estimation errors (*relative magnitude* and *epoch*) for different associations of *2 tracks*. 78
4.24 Variation of estimation error (*relative magnitude*) for different associations of *3 tracks*. 79
4.25 Variation of estimation error (*epoch*) for different associations of *3 tracks*. . 79

A.1 Representation of GRCS coordinate system. 96
A.2 Representation of the topocentric horizon coordinate system. 98
A.3 Coordinates of a point in topocentric horizon coordinate system. 99

List of Tables

4.1 Characteristics of satellite for propagation accuracy test. 50
4.2 Propagation times for the LEO object. 50
4.3 Force models of the high-fidelity propagator. 50
4.4 Noise sigmas of the simulated radar. 56
4.5 Report of manoevure detection statistics. 61
4.6 Manoeuvres not detected at the first post-manoeuvre track. 62
4.7 Characteristics of manoeuvre on July 12th, 2017. 69
4.8 Characteristics of chosen estimate for manoeuvre on 12/07/2017 with tracks {1, 2, 3, 4}. 72
4.9 Characteristics of manoeuvre on September 6th, 2017. 74
4.10 Characteristics of chosen estimate for manoeuvre on 06/09/2017 with tracks $\{1, 2, 3, 4\}$. 75

B.1 Manoeuvre history of Sentinel 3-A in years 2017 to 2019 [95]. 103

List of Symbols

Variable	Description	SI unit
A	azimuth	rad
B^*	starred ballistic coefficient	$-$
E	elevation	rad
f	Earth's oblateness	$-$
h	geodetic height	m
J	weighted root mean square error	$-$
$\mathbf{p}$	dynamical parameters vector	$-$
$\mathbf{r}$, $\mathbf{R}$	position vector	km
R_P	Earth's polar radius	km
$R_\oplus$	Earth's equatorial radius	km
$\mathbf{u}$	manoeuvre vector	m/s
$\mathbf{v}$, $\mathbf{V}$	velocity vector	km/s
$\mathbf{x}$, $\mathbf{X}$	state vector	km, km/s
$\mathbf{y}$	full state vector	km, km/s, $-$
W	measurements weighting matrix	$1/mm^2$, $1/(mm/s)^2$, $1/rad^2$
$WRMS$	weighted root mean square error	$-$
$\mathbf{z}$	observation	m, mm/s, rad
α	right ascension	rad
δ	declination	rad
ΔV	velocity impulse	km/s
λ	geodetic longitude	rad
$\boldsymbol{\rho}$	measurements residuals	m, mm/s, rad
ρ	range	m
$\dot{\rho}$	range rate	m/s
σ	standard deviation	m, mm/s, rad
ϕ	geodetic latitude	rad
Φ	state transition matrix	km/s, km/s^2
Ψ	full state transition matrix	km/s, km/s^2, $1/s$

Acknowledgements

I'm dedicating this small space to who contributed to the realisation of this thesis.

At first, I would like to thank prof. Pierluigi Di Lizia, who followed and supported me throughout the development of the thesis, and to whom I'm grateful for proposing me the opportunity to work in a company abroad, allowing me to grow personally and begin a career in this sector.

A word of thanks to Diego Escobar, head of the Space Situational Awareness section at GMV, who guided me in conducting the research and from whom I could learn a lot about these topics. A great thank you to Alejandro Pastor, who introduced me to these very interesting problems about data association and from whom I could take inspiration to develop the thesis. A special thanks to Alejandro Cano, who always provided me precious advice to improve this work and also grow professionally.

Thanks to my parents that, despite the difficulties of last years, never lost heart and always were by my side. Thanks for having supported me in any decision and for always setting me on the right path. Thanks to my brother, sister and the whole family, which always make me remember how blessed I am to have them by my side. Thanks to my friends and classmates with whom I spent unforgettable moments in the last five years, and thanks to Milan, city where I will always feel at home.

Finally, the greatest thank you to those who are no longer: it would have been wonderful to live these moments with you.

Ringraziamenti

Dedico questo piccolo spazio a chi ha contribuito alla realizzazione di questo elaborato.

Vorrei innanzitutto ringraziare il prof. Pierluigi Di Lizia, che mi ha seguito e supportato nella svolgimento di questa tesi, e a cui sono grato per avermi proposto la possibilità di lavorare in un'azienda estera, permettendomi di maturare e di iniziare una carriera in questo settore.

Un ringraziamento va a Diego Escobar, capo della sezione di Space Situational Awareness di GMV, che mi ha guidato nel condurre la ricerca e da cui ho potuto imparare molto di questa disciplina. Ringrazio tantissimo Alejandro Pastor per avermi introdotto nel mondo dei problemi di associazione di dati e per avermi dato spunti interessanti per lo sviluppo della tesi. Un grazie speciale ad Alejandro Cano, da cui ho sempre ricevuto consigli preziosi per migliorare il lavoro e anche per crescere professionalmente.

Un grazie ai miei genitori, che, nonostante le moltissime difficoltà di questi anni, non si sono mai persi d'animo e sono sempre stati al mio fianco. Grazie per avermi supportato in ogni mia decisione e per avermi sempre condotto sulla strada corretta. Grazie a mia sorella, a mio fratello e a tutta la famiglia, che ogni volta mi fanno ricordare quanto sia importante averli con me. Grazie agli amici e compagni di corso con cui ho passato bellissimi momenti in questi ultimi cinque anni, e grazie a Milano, città dove mi sentirò sempre a casa.

Infine, il grazie più sentito a chi non c'è più: sarebbe stato bellissimo vivere questi momenti con voi.